

PROTON SCATTERING IN NOVA TEST BEAM

Teresa Lackey

Submitted to the faculty of the University Graduate School
in partial fulfillment of the requirements
for the degree
Doctor of Philosophy
in the Department of Physics,
Indiana University
July 2022

Accepted by the Graduate Faculty, Indiana University, in partial fulfillment of the requirements
for the degree of Doctor of Philosophy.

Doctoral Committee

Mark Messier, PhD

Herbert Fertig, PhD

Chen-Yu Liu, PhD

Jon Urheim, PhD

Date of Defense: 05/13/2022

Copyright © 2022

Teresa Lackey

There is a special sadness in achievement, in the knowledge that a long-desired goal has been attained at last, and that life must now be shaped towards new ends.

Arthur C. Clarke, *The City and the Stars*

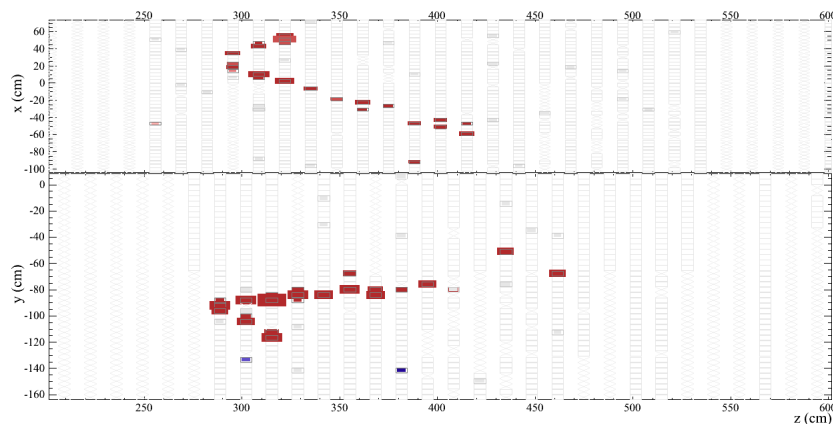
ACKNOWLEDGEMENTS

First, thank you Mark for always going above and beyond. You have been such a caring and compassionate advisor and I've learned so much from you over the years. I hope to continue doing so in the years to come. Thank you to the rest of the IU group; you've all been like a family to me. Thank you for always listening to my venting, answering my questions, and being there with me through all the ups and downs life (and grad school) threw at me over the years.

It takes a village to raise a graduate student and there are too many people who have helped me over the years to list them all here, but I especially want to thank everyone in the Operations and Test Beam groups. I've made countless friends throughout graduate school on NOvA and during my time based at Fermilab. A special thank you to the coven for all the great memories.

To my family, for all the dinner conversations growing up that first piqued my interest in physics, thank you for all your support over the years. Mum, you had almost endless patience with my early questions about the origin of matter in the universe; Dad, your lengthy answers to my questions may not have always answered my actual question, but I always learned something; and Peggy, I'm proud to have been your first (human) student.

Thank you Ben for all the home-cooked meals. I don't know how I would have fed myself in the last months without you. Thank you CJ for being my friend all these years. You somehow always know what I need. And finally, she may not say much I understand, but I can't imagine life without my constant companion through graduate school, Mindy.



The first ν_e event I identified in NOvA's prototype near detector, NDOS, almost a decade ago.

Teresa Lackey

PROTON SCATTERING IN NOVA TEST BEAM

The NuMI Off-axis ν_e Appearance (NOvA) experiment is a two-detector, long baseline, neutrino oscillation experiment, which aims to make a determination of the neutrino mass ordering, the octant of θ_{23} , and measure possible charge-parity (CP) violation. Determining these parameters is a step towards answering some of the fundamental questions about neutrinos. Are neutrinos their own antiparticle? Could neutrinos be responsible for the matter-antimatter asymmetry of the universe? How do neutrinos get their mass? Answering these questions requires precise measurements of the parameters that govern how neutrinos behave, namely the mass squared splittings, mixing angles, and possible CP-violating phase factor in the PMNS matrix. Reaching high precision requires minimizing both statistical and systematic errors. As NOvA continues to accumulate data, the sizes of our statistical errors continue to shrink such that in a couple of years they will be comparable to our systematic errors. NOvA's current systematic errors are dominated by energy and calibration uncertainties. The Test Beam program was initiated to address these uncertainties by assessing the detector response in an environment where more parameters of the incoming particles are known. One of the main goals of the Test Beam program is to garner a better understanding of our systematic errors, particularly in energy measurement and detector response, so that the modeling of these parameters can be improved.

I studied protons in the Test Beam Detector with momenta around 1 GeV/c, the high end of the momentum range relevant to quasielastic neutrino interactions in NOvA. One question this sample can help to answer is if we correctly simulate the fraction of protons that have an inelastic scattering interaction versus ranging out. If protons inelastically scatter at different rates in our simulation and data, the correction applied to the hadronic system when reconstructing neutrino

energy could be inaccurate, since events with inelastic scattering will have less visible energy in the detector. This is particularly important for quasielastic ν_μ events, which have the lowest hadronic energy resolution, and therefore give us our best measurements of Δm_{32}^2 and θ_{23} .

Mark Messier, PhD

Herbert Fertig, PhD

Chen-Yu Liu, PhD

Jon Urheim, PhD

Table of Contents

Acknowledgements	v
Abstract	vi
List of Tables	x
List of Figures	xii
Chapter 1: Neutrinos	1
1.1 Proposal and first detection of neutrinos	1
1.2 Discovery of the muon and tau neutrinos	3
1.3 Neutrino Oscillations	8
1.3.1 Experimental Evidence of Neutrino Oscillations	10
1.4 A review of other neutrino experiments	11
Chapter 2: NOvA	18
2.1 NuMI Beam	19
2.2 NOvA Detectors	21
2.3 Event Reconstruction and Selection	25
2.4 Extrapolation and Results	28
2.5 Systematic Uncertainties	29
Chapter 3: NOvA Test Beam	34
3.1 Beam	35
3.2 Tertiary Beamline Components	36

3.2.1	Time of Flight System	36
3.2.2	Multi-Wire Proportional Chambers and Magnet - momentum reconstruction .	39
3.2.3	Cherenkov Detector	41
3.2.4	Scintillator Paddles	41
3.2.5	Helium pipes	43
3.3	NOvA Test Beam Detector	43
3.3.1	Triggers	44
3.3.2	Detector Geometry	45
3.3.3	Detector Calibration	50
3.4	Test Beam Installation, Commissioning, and Data-Taking Summary	52
Chapter 4: Accounting for Detector Electronics Shutoff		65
4.1	Front End Board Shutoffs	65
4.2	Overall Infrastructure Description	67
4.2.1	Tuning the time window and cut on number of hits	68
Chapter 5: Data Selection		75
Chapter 6: Simulation		84
6.1	Cosmic simulation	84
6.2	Threshold and Baseline Distributions	86
6.3	Brightness Levels	86
6.4	Light Level View Factors	88
6.5	Simulating Beamline Events	89
Chapter 7: Nuclear Interaction Length		94

7.1	Proton interactions	94
7.2	Data Selection and Simulation	96
7.3	Fitting in bins of p_T	99
7.4	Cross checks	102
7.5	Interpretation of Results	106
Chapter 8: Summary		109
References		110
Curriculum Vitae		

List of Tables

3.1	Efficiencies for beamline trigger conditions. For the majority of period 2, we ran with the 4 of 4 scintillator paddle trigger.	59
3.2	Running conditions for period 2.	60
3.3	Running conditions for period 3. FEB versions: v4.10.2E (nominal FD), v4.11.35 ($\times 16$ w/ shutoff bit), and v4.11.33 ($\times 16$ buffer).	64
4.1	Cuts applied to 1312 selected events with shutoff bit information available. Rows show events that passed or failed based on the cuts being tuned for the EventFEBStatus module. Columns show events that did or did not have FEB shutoffs based on the status bit information from the DAQ. Off diagonal elements show the false positives and false negatives.	70
4.2	Cuts applied to 1312 selected events with shutoff bit information available, focussed on a time window of 10 ms. Rows show events that passed or failed based on the cuts being tuned for the EventFEBStatus module. Columns show events that did or did not have FEB shutoffs based on the status bit information from the DAQ. Off diagonal elements show the false positives and false negatives.	74
5.1	First round of cuts applied to events to select ~ 1 GeV/ c protons.	76
5.2	Number of triggers that pass beamline selection cuts. Time of flight (TOF) and wire chamber (WC) reconstruction requirements only check for the existence of reconstruction, not the value of the parameter. Proton selection requires $52 \text{ ns} < \text{time of flight} < 70 \text{ ns}$ and no signal in the Cherenkov detector, along with an existing wire chamber track.	77
5.3	Cuts to ensure quality of wire chamber (WC) track.	78
5.4	Cuts applied to hits in the NOvA detector prior to clustering.	82
5.5	Cuts applied at the track and event level in the NOvA detector.	83
5.6	Number of protons that came from each trigger type.	83
6.1	Cuts applied to hits prior to clustering.	92
6.2	Cuts applied at the track and event level.	92

7.1 GEANT process codes and average reconstructed transverse momentum, $\langle \text{reco } p_T \rangle$, for immediate daughter particles of simulated protons. Example event displays of protons with no daughters, inelastic scattering, and elastic scattering are in Figures 7.3-7.5. 97

7.2 Fit results for cross checks. p-values expressed as fractions. 105

7.3 Summary of absolute statistical and systematic errors for $f = 0.771$ 106

List of Figures

1.1	From [4], Savannah River Neutrino Detector. Target tanks A and B were filled with 200 L water with 40 kg CdCl ₂ dissolved to capture neutrons. Tanks 1, 2, and 3 contain 1400 L liquid scintillator and have 55 photo multiplier tubes on each end.	2
1.2	From [13], overview of experimental setup at the Brookhaven Alternating Gradient Synchrotron (AGS). The angle from the direction of protons in the beam to the detector is 7.5°. The detector sits behind a 13.5 m iron shield wall.	4
1.3	From [15], candidate ν_τ event from DONUT. Darkened line exiting the primary vertex is a τ which decays to $e^- + \nu_\tau + \nu_e$ at the location of the kink in the track. Perpendicular lines provide the scale - vertical line is 0.1 mm, horizontal line is 1.0 mm.	5
1.4	From [17], average value of $e^+e^- \rightarrow$ hadrons cross section as a function of center of mass energy from LEP experiments ALEPH, DELPHI, L3, and OPAL. Error bars increased by a factor of ten for visibility. The data match the theoretical three neutrino curve.	6
1.5	From [19], distributions of the cosine of the angle between electron trajectory and the direction of the sun in neutrino events in the Kamiokande-II detector, split up by electron energy. Electrons that point straight back to the sun have $\cos \theta_{\text{Sun}} = 1$	7
1.6	From [25], the ratio of fully contained events in data to Monte Carlo events assuming no oscillations versus L/E_ν . A ratio of 1 would imply data matches the no-oscillation assumption. Dashed lines show expected shape assuming $\nu_\mu \leftrightarrow \nu_\tau$ oscillations with $\Delta m^2 = 2.2 \times 10^{-3} \text{ eV}^2$ and $\sin^2 2\theta = 1$	10
1.7	From [39], cartoon showing the average baselines for Double Chooz, RENO, and Daya Bay. The two Daya Bay baselines shown are for distances to the Daya Bay Nuclear Power Plant and the Ling Ao Nuclear Power Plant reactor cores. The closest detector for each experiment is about 300-400 m from the reactors. The furthest detectors for each experiment range from about 1000 m to 1700 m away from the reactors.	13
1.8	From [41], visible energy spectrum of contained K2K events in the Super-K detector. Data points are in black, the solid blue line is the expectation from simulation without neutrino oscillations, and the dashed red line is the expectation from simulation at the best fit point of $\Delta m^2 = 2.8 \times 10^{-3} \text{ eV}^2$ and $\sin^2 2\theta = 1$	14
1.9	90% confidence level contours for normal mass ordering in Δm_{32}^2 vs. $\sin^2 \theta_{23}$ phase space from [27, 44–47].	16

2.1	Map of NOvA experiment layout. The NuMI beam and NOvA Near Detector are located at Fermilab while the Far Detector is located 810 km away in northern Minnesota. The location of the MINOS Far Detector in Soudan, MN at a baseline of 735 km is also shown.	18
2.2	From [50], NuMI beam components not drawn to scale.	19
2.3	Neutrino energy spectra that would be seen by the NOvA Far Detector for various off-axis angles. The NOvA detectors are located 14.6 mrad off-axis.	20
2.4	Neutrino flux at the Near Detector for neutrino mode (left) and antineutrino mode (right). Between 1 and 5 GeV the ν_μ ($\bar{\nu}_\mu$) beam is 93% (92%) pure.	21
2.5	Weekly protons-on-target (POT) recorded by the NOvA Far Detector from February 2014 to March 2020. Data taken in (anti)neutrino mode is displayed in orange (blue). The long gaps each year are due to Fermilab's summer beam shutdown. Total exposure: 13.6×10^{20} in ν mode and 12.5×10^{20} in $\bar{\nu}$ mode.	22
2.6	Left: Schematic of NOvA detector planes with alternating horizontal and vertical planes of cells. Right: Schematic of single NOvA cell. Each cell has a cross-section of $4 \times 6 \text{ cm}^2$ and a wavelength shifting fiber looped through the length of the cell.	22
2.7	From [52]. Left: absorption and re-emission spectra for the primary scintillant, pseudocumene, and wavelength shifters, PPO and bis-MSB, present in the NOvA liquid scintillator. Right: the absorption and re-emission spectrum for the dye used in the wavelength shifting fiber.	23
2.8	ν_μ charged current data event in the Far Detector. Bottom image has the reconstructed vertex drawn as a yellow cross, the muon hits outlined in pink, and the proton hits outlined in blue. For each image, the top half is a top-down view of the detector and the bottom half is a side view of the detector, with beam entering from the left for each. A spline fit uses the range of the muon to determine its energy, while a second spline fit based on the visible energy in the hadronic system determines the remaining energy in the event.	26
2.9	ν_e charged current data event in the Far Detector. Bottom image has the reconstructed vertex drawn as a yellow cross, the electron hits outlined in lime green, and two tracks in the hadronic system outlined in pink and blue. For each image, the top half is a top-down view of the detector and the bottom half is a side view of the detector, with beam entering from the left for each. A CNN classifies hits in the event as electromagnetic or hadronic in origin and a quadratic fit yields the energy of the neutrino.	27
2.10	Diagram of the steps of the extrapolation procedure for predicting the ν_μ energy spectrum at the Far Detector. We start with the reconstructed energy spectrum of neutrinos in the Near Detector at the top left and after converting to true energy, accounting for differences between the two detectors, including neutrino oscillations, and converting back to reconstructed energy we end with the expected spectrum in the Far Detector at the top right.	29

2.11	ν_μ (top) and ν_e (bottom) energy spectra at the Far Detector for neutrino (left) and antineutrino (right) data compared with extrapolated simulation best fit results. The peak in the ν_e spectra is in the same location as the dip in the ν_μ spectra, where the $\nu_\mu \rightarrow \nu_e$ oscillation probability is maximal.	30
2.12	Confidence level contours in Δm_{32}^2 vs. $\sin^2 \theta_{23}$ (left) and $\sin^2 \theta_{23}$ vs. δ_{CP} (right) phase spaces for normal (top) and inverted (bottom) mass ordering. The best fit point is shown as a black cross on the normal ordering contours.	31
2.13	90% confidence level contour for normal mass ordering in Δm_{32}^2 vs. $\sin^2 \theta_{23}$ phase space overlaid with results from other experiments [27, 45–47].	31
2.14	Systematic and statistical uncertainties for Δm_{32}^2 , $\sin^2 \theta_{23}$, and δ_{CP} . Detector calibration is the dominant source of systematic uncertainty for each parameter.	32
2.15	Data (black) to Monte Carlo (red) comparison of dE/dx for protons in the Near Detector as a function of the distance to the end of the proton track. The ratio between data and Monte Carlo has an average of 0.9579.	33
3.1	Fish-eye photo of NOvA Test Beam experiment.	34
3.2	From [62], diagram of the accelerator complex at Fermilab. For Test Beam experiments, beam begins at the pre-accelerator on the upper right of the diagram and continues through the Linac, Booster, Main Injector, and Recycler, and is then extracted to the Switchyard line on the right hand side of the diagram. NOvA Test Beam is located on the Meson line of Switchyard.	35
3.3	Spill structure found by counting up hits on a single pixel in the NOvA detector and integrating over multiple spills. Data collected with low intensity beam (1×10^8 ppp) to reduce electronics shutoffs. The unevenness of the spill is due to the chaotic nature of the resonant extraction. Some buckets will be empty while others will be overfilled. 37	37
3.4	Diagram of beamline components. Scintillator paddles and helium pipes not shown. The distance from the target to the NOvA detector is 14.62 m.	37
3.5	Time of flight for 1 GeV/ c particles in period 2. The time of flight detectors are separated by 13.16 m. They provide good separation between protons, kaons, and the peak of faster particles, but do not provide separation between electrons, muons, and pions.	38
3.6	From [64], effective magnetic field as a function of magnet current. Points are the values obtained from using the full field maps and the red curve is the parameterization. Field maps for 300, 1200, and 2100 A were measured, the others were interpolated from the measured maps.	40

3.7	Time of flight versus momentum for 1 GeV/ c protons (top) and all 1 GeV/ c particles (bottom). The plots on the right have a 1% downward shift in momentum applied. The time of flight for a speed of light particle passing through the beamline is 43.9 ns.	42
3.8	Pressure threshold for Cherenkov radiation in CO ₂ . NOvA Test Beam used CO ₂ at 1 atm. At this pressure electrons with momentum down to 20 MeV/ c will emit Cherenkov radiation while muons, pions, kaons and protons will not.	43
3.9	Picture of the NOvA Test Beam detector in the MC7b enclosure at the Fermilab Test Beam Facility. The silver tube to the right (upstream) of the detector is the Cherenkov detector.	44
3.10	Vertical plane with locations of survey points. Plane 6 was missing point a .	45
3.11	Horizontal plane with locations of survey points.	46
3.12	z (depth in beam direction) location of each plane. The front face of the detector is at $z = 0$. Plane centers are an average of 6.68 cm apart. The variation along this line is due to variation in where the measurements were taken, not in plane depth.	47
3.13	x (horizontal) location of each plane. Vertical planes show the expected stagger. This is done so that if a particle passes through the plastic between cells in one plane, it will enter the cell in the next vertical plane. The stagger between planes is about 1 cm, with a shift of 1.5 cm between blocks. Horizontal planes also shift about 1.5 cm between blocks.	48
3.14	y (vertical) location of each plane. The horizontal planes are staggered in their vertical position, but not as precisely as the horizontal stagger. There is no obvious shift between blocks in the vertical position.	48
3.15	Roll (around beam direction) of each plane. Unfortunately, the direction of the roll means the east side of the detector is slightly lower than the west side. The east side is where the readout and fill ports for the scintillator are. As a result, the top cell in each horizontal module is underfilled, with an air bubble on the west side.	49
3.16	Difference between start location of track in NOvA detector and wire chamber (WC) track projected forwards to the front face of the NOvA detector after tuning the placement of the detector.	50
3.17	Difference between direction of track in NOvA detector and direction of wire chamber (WC) track after tuning the rotation (pitch and yaw) of the detector. Plot made using tracks with a z direction > 0.99 to remove any protons that may have inelastically scattered, thus changing their direction. Due to the granularity of the NOvA detector, some directions are favored over others based on the geometry of the cells. The rotation of the detector was chosen so that the peak in these distributions is at 0.	50

3.18 MeV/cm vs. distance from the end of the muon track for stopping muons in Test Beam data. Muons deposit just under 2 MeV/cm in the detector in the minimally ionizing portion of their track.	51
3.19 Photoelectrons/cm as a function of distance along the cell for cosmic ray muon hits in the Test Beam Detector in two different cells. Data points are in black and the attenuation fits are the blue lines. The dashed lines show where the edges of the detector are.	52
3.20 DCM timing offsets for Test Beam Detector (left) and Far Detector (right). The Far Detector has 28 timing chains, with 6 DCMs each. Offsets between DCMs at the Far Detector are comparable to the offset between DCMs 1 and 2 on the Test Beam Detector. DCM 3 has faster electronics, so the offset cannot be directly compared. . .	52
3.21 Timing resolution vs. pulse height of Test Beam Detector (left) and Far Detector (right). The timing resolution of the two detectors is similar.	53
3.22 Event display of triggered event in period 2. Large blank spaces and gaps are a result of shutoff electronics. The hits that do show up are from high energy muons that passed through the detector during the 150 μ s readout window. The tertiary beam spot is around $x=0, y=-7$	54
3.23 Event display of triggered event in period 1 zoomed in on the 10 μ s around the particle that caused the trigger. Even though there are no clear signs of electronics shutoff, there are a number of particles passing through the detector alongside the particle of interest. The second block was not active for period 1.	55
3.24 Hits on the front face of the NOvA detector, looking upstream towards the beamline. The tertiary beam spot is approximately centered on the detector, while the beam plume is most prominent in the upper west quadrant. The beam spot is most visible in the lower east quadrant because the electronics in this region do not shut off as much as in the other three quadrants.	56
3.25 Hits on a pixel during the 4.2 s spill found by counting up hits on a single pixel in the NOvA detector and integrating over multiple spills. Data collected with a beam intensity of 5×10^9 ppp. You can see the initial ramp-up of the beam and then a drop from the electronics shutting off. Throughout the spill the electronics are turned back on at a rate of 10 Hz and then shut off again once their buffers fill up.	57
3.26 Top (left) and side (right) views of where tracks in the upper west region of the detector point back to. The front face of the NOvA detector is at the far right side of the plot and the location of the secondary target is indicated with a red x.	58
3.27 Time of tracks in detector. The particle that caused the trigger should enter the detector around 51-52 μ s. Peaks either side of this are from adjacent buckets of beam, spaced 11.2 μ s apart.	61

3.28	X (left) and Y (right) start location of in-time tracks in the detector. In-time tracks have a mean time between 45 and 55 μ s.	62
3.29	Number of particles passing basic selection cuts in periods 2 (left) and 3 (right). . . .	62
4.1	Event display of selected event, zoomed in on the 10 μ s around the particle that caused the trigger. At least half of the v4 FEBs in the first block and all of the v4 FEBs in the second block are missing, indicating they were likely shut off during the event. The line of cells lit up in the middle of each block is from the v5 FEBs.	66
4.2	Shutoff status for selected protons plotted against time for period 2. Spikes in shutoffs correspond to days when we ran at higher intensities for various intensity studies and other beam tuning.	70
4.3	Number of hits in a given time window before (left) and after (right) the event time of interest. Time window ranges from 5 ms (top) to 50 ms (bottom). The large peak at zero are FEBs that are shutoff, while the population of FEBs with non-zero hits in the time window are presumed to be active. I chose a time window of 10 ms (Figure 4.3c and Figure 4.3d).	71
4.4	Number of hits in a given time window before (left) and after (right) the event time of interest. Time window ranges from 5 ms (top) to 50 ms (bottom). The red line shows FEBs that reported a shutoff during the 110 ms prior to the event, while the blue line shows FEBs that were not shutoff during this time. I chose a time window of 10 ms (Figure 4.4c and Figure 4.4d).	72
4.5	Number of hits in a given time window before (left) and after (right) the event time of interest vs. FEB #. Time window ranges from 5 ms (top) to 50 ms (bottom). FEBs 16-31 (west-vertical modules) in both blocks shut off the most frequently, while FEBs 0-15 (east-vertical modules) shut off the least frequently. The beam plume is most intense for the west-vertical modules, then top-horizontal, bottom-horizontal, and finally, east-vertical. DCM 3 contains the ND v5 FEBs which, due to a higher readout rate, shut off less frequently than the FD v4 FEBs using the original firmware (v4.10.2E). The selected time window needs to be long enough to ensure the quietest FEBs have a hit in them so they are not incorrectly marked as shutoff, while keeping it short enough that you do not miss a shutoff due to an FEB being re-enabled at the edge of the window.	73
5.1	Time of flight vs. momentum for beamline particles from 1000 A runs. Lines overlaid are theoretical curves assuming a path length of 13.2 m between the time of flight detectors. Particles with a time of flight between 52 and 70 ns were identified as protons.	76

5.2	Left: Momentum calculated from wire chamber (WC) track plotted against the distance in the horizontal (XZ) plane between where the track enters the magnet and the central axis of the magnet. Right: Fractional difference in momentum calculated using range in the detector and using the WC track. The west side of the magnet is the positive side. The magnetic field will bend particles towards the west. Events outside of the red lines are rejected.	77
5.3	NOvA detector (X,Y) coordinates of wire chamber (WC) track where it intersects with the front face of the detector (Z=0). Events outside the red box are rejected.	78
5.4	Time in ns of hits within each event, zoomed in on the window around the particle the beamline triggered on. The earlier peak is from TOF based triggers and the later peak is from scintillator paddle based triggers.	80
5.5	Time in ns of hits within each event for TOF (left) and scintillator paddle (right) based triggers. Hits outside of the red lines are dropped prior to the clustering stage.	80
5.6	Cell and plane location for each hit in the detector for simulated (left) and data (right) protons. Hits outside of the red lines are dropped prior to the clustering stage. The plane to plane offsets are due to the beam spot being centered in vertical (even) planes and just low of center in horizontal (odd) planes.	81
5.7	Mean time of hits on the track. As with the time of individual hits, this cut is split by trigger conditions to account for the slightly different timing of TOF vs scintillator paddle based triggers. Tracks outside of the red lines are rejected.	81
5.8	Maximum plane the track reaches. Longer tracks are caused by plume particles and are rejected.	82
5.9	The sum of hits in all clusters in the event. Noisier events are more likely to have plume contamination and are rejected.	82
5.10	Distributions of the final selected sample of protons. Length of the proton track in the NOvA detector is on the left and calorimetric energy of the track is on the right.	83
6.1	Data-driven activity trigger rate for one week in the Test Beam Detector. Beam was off for the beginning of the week, where the rate is flatter around 14.4 Hz.	84
6.2	From [72], μ^+/μ^- ratio as a function of muon momentum measured by BESS. Muons that stop in the Test Beam Detector have momentum $< 1 \text{ GeV}/c$	86
6.3	Threshold distributions for v4 (left) and v5 (right) FEBs on the Test Beam Detector from pedestal scans taken during period 3.	87
6.4	Baseline distributions for v4 (left) and v5 (right) FEBs on the Test Beam Detector from pedestal scans taken during period 3.	87

6.5	Relative brightness of each cell in the Test Beam Detector. There is a distinct increase of brightness between the first 32 planes and the next 21, where the scintillator from Ash River was used. The brightness decreases slightly in the last 10 planes. The very bright region in plane 55 is from a single noisy FEB.	88
6.8	pe/cm of muon hits in vertical (left) and horizontal (right) cells split up by bins of distance to the end of the muon track. Data points are in black, the red line is simulation before (top) and after (bottom) fitting for $F_{x,y}$	90
6.9	pe/cm for all muon hits in data (black), simulation before tuning (orange) with $F_x = 0.5078$ and $F_y = 0.4927$, and simulation after tuning (green) with $F_x = 0.4791$ and $F_y = 0.4473$	90
6.10	Diagram of beamline material between the fourth wire chamber and the NOvA detector. The grey block on the right is the NOvA detector. Sizes of beamline detector are inflated in the XY plane to ensure simulated particles will pass through them even if they are misaligned in the geometry.	91
6.11	Mean time of hits on the track for simulation. Tracks outside of the red lines are rejected.	92
6.12	Maximum plane the track reaches. Longer tracks are caused by plume particles and are rejected. Simulation is area normalized to data. Tracks in data are about a plane shorter on average than tracks in simulation. The cause for this is unknown.	93
6.13	The sum of hits in all clusters in the event. Noisier events are more likely to have plume contamination and are rejected. Simulation is area normalized to data.	93
7.1	From [77], nucleon-nucleus cross sections (y-axis, in barns) as a function of mass number A (x-axis). The middle panel is for 1 GeV particles, with the open triangles for the inelastic cross section.	95
7.2	From [58], inelastic and production cross sections of protons on a carbon target. For the energies in NOvA Test Beam, GEANT uses the Barashenkov (solid line) interpolations. The NOvA detectors are 67% carbon by mass.	96
7.3	Simulated proton that ranged out without creating any daughter particles.	97
7.4	Simulated proton with a daughter particle created by the <i>protonInelastic</i> GEANT process code, indicative of an inelastic scatter.	98
7.5	Simulated proton with a daughter particle created by the <i>hadElastic</i> GEANT process code, indicative of an elastic scatter. Events with elastic scattering have a similar topology to ones that range out with no scattering.	98

7.6	Opening angle between initial direction and direction in detector (left) and track length of proton in detector (right). While these variables show some differences between the inelastic scattering and range out populations, they do not have enough separation for a reliable fit.	99
7.7	Transverse momentum for simulated events that contain an inelastic scatter, elastic scatter, or no scattering.	100
7.8	Transverse momentum for data and simulation prior to the fit.	101
7.9	Transverse momentum for data and simulation with the fit result. Simulated population for inelastic scatter (range out) was tuned up (down) by the amount indicated by the fit. The red fit line is $1.0(0.77 \times MC_{\text{range}} + (1.23) \times MC_{\text{scatter}})$	101
7.10	Residuals of fit.	102
7.11	Secondary beam intensity for spills with selected protons. The red line is at 1.55×10^9 ppp. Events to the left (right) of this line are in the lower (higher) intensity sample.103	103
7.12	Misreconstructed track due to extra hit from beam plume. There were 3 higher intensity events that looked like this.	104
7.13	Track with the wrong direction in the x-view. The extra hits around $z=110$ are likely due to a neutron kicked out from an interaction at the end of the proton track. One hit in the x-view was missed due to the spatial cuts in the clustering algorithm. This was the only high intensity event with this problem.	104
7.14	An example of an event from a high intensity spill with good reconstruction. The majority of high intensity events fell into this category. The other hits in the event are likely from a muon in the beam plume.	105
7.15	New nuclear interaction length, λ'_i , that would increase the number of protons that inelastically scatter to match the fit results. Plot made using simulated protons without any inelastic scattering.	107

Chapter 1

Neutrinos

Neutrinos are one of the most abundant particles in the universe, and over the past ~ 90 years since the proposal of their existence, we have learned much about their properties. In this chapter I will review the history of neutrino physics, describe some of the past and current neutrino experiments, and give an overview of the current status of the field.

1.1 Proposal and first detection of neutrinos

Observations of electron energies in beta decay experiments found that rather than the expected discrete energy, as seen with alpha and gamma decay, the electrons had a continuous energy spectrum [1]. This appeared to violate energy conservation, so in 1930 Pauli proposed there was a neutral, light particle, close to the mass of an electron, that carried the remainder of the energy in each interaction [2]. At the time, Pauli believed he had proposed a particle that could never be detected. In 1934 Fermi used Pauli's proposed particle to formalize the theory of beta decay wherein nuclear decay results in the decayed isobar, an electron, and a neutral, spin $\frac{1}{2}$, light particle: the neutrino [3].

Fortunately, Pauli's fear that the neutrino was undetectable proved to be wrong. Cowan and Reines carried out two experiments studying inverse beta decay at nuclear reactors to search for evidence of the neutrino. The first was at the Hanford Reactor in Washington in 1953 [5], and the second was at the Savannah River Plant in South Carolina in 1956 [4, 6]. Both experiments had the same premise: they studied the inverse beta decay reaction $\bar{\nu}_e + p \rightarrow n + e^+$, looking for evidence of a prompt positron signal in coincidence with a delayed signal from neutron capture in cadmium. The initial experiment at Hanford had a very large background rate, likely due to cosmic rays, but Cowan and Reines noted a difference in the event rate for reactor-on versus reactor-off running that provided tentative evidence for the existence of the neutrino. The experiment at the Savannah River Plant employed more shielding to reduce background rates from both cosmic rays and the reactor. The detector, shown in Figure 1.1, consisted of two target tanks – polyethylene boxes filled with

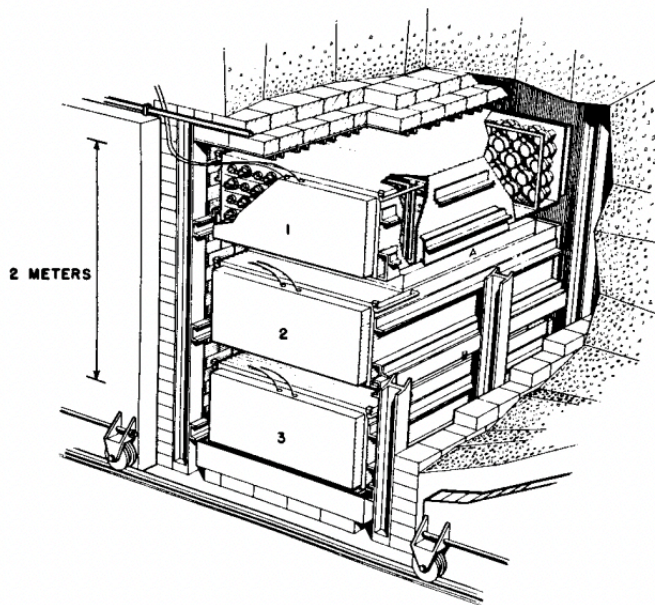


Figure 1.1: From [4], Savannah River Neutrino Detector. Target tanks A and B were filled with 200 L water with 40 kg CdCl_2 dissolved to capture neutrons. Tanks 1, 2, and 3 contain 1400 L liquid scintillator and have 55 photo multiplier tubes on each end.

water and cadmium chloride – sandwiched between three scintillator counters read out by 110 5 in photo multiplier tubes. The observed signal was within 5% of the predicted cross section (although that cross section had a $\pm 25\%$ uncertainty), thus confirming the existence of the neutrino. This work earned Frederick Reines the Nobel Prize in Physics in 1995.

Neutrinos led to many advancements in detection technology and in the theory of weak interactions. In 1956 Lee and Yang proposed the possibility of parity violation in weak interactions and suggested a couple experiments that could prove the violation [7]. The first of these was to study Λ^0 production and the subsequent decay, $\pi^- + p \rightarrow \Lambda^0 + \theta^0$, $\Lambda^0 \rightarrow p + \pi^-$. The momenta of the incoming and outgoing pions along with the momentum of the Λ^0 can be used to construct a pseudoscalar whose sign changes as the handedness of the particles change. If parity is conserved, we should observe equal proportions of positive and negative values for the pseudoscalar. An asymmetry in the values would point to parity violation. To observe an asymmetry in the pseudoscalar, the Λ^0 must be polarized. The same method could be applied to the decay of any strange particle as long as it decays to 3 or more particles, or decays to 2 particles, at least one of which must have nonzero spin. Lee and Yang's second suggested experiment was studying pion decay at rest, $\pi \rightarrow \mu + \nu$, $\mu \rightarrow e + \nu + \nu$. If parity is violated, the distribution of the angle between the muon and the electron

will not be symmetric for θ and $\pi - \theta$. Wu discussed these potential experiments with Lee and Yang and decided to pursue a study of the angular distribution of electrons in beta decay [8, 9]. Wu, with the aid of Amble and his low temperature lab at the National Bureau of Standards, polarized a Co^{60} source up to 65% using a process called adiabatic demagnetization [10, 11]. This process requires cooling the nuclei to liquid helium temperature. The polarization of Co^{60} was measured by observing the anisotropy of gamma rays emitted from the nuclei. An anthracene crystal 2 cm above the Co^{60} source detected β particles. Measuring the angular distribution of the electrons relative to the initial orientation of the nuclei, Wu and Amble found that the electrons were emitted in the direction opposite the nuclear spin and calculated the asymmetry parameter for the electron angular distribution close to -1, implying near-maximum interference between parity conserving and parity non-conserving terms in the Hamiltonian. This demonstrated that parity is violated in weak interactions, and that electrons are left-handed. This work earned Chen Ning Yang and Tsung-Dao Lee the Nobel Prize in Physics in 1957.

In 1957 Goldhaber, Grodzins, and Sunyar carried out an experiment to determine the helicity, or handedness, of neutrinos [12]. They observed circular polarization of gamma rays emitted from orbital electron capture on Eu^{152} , through the chain reaction $e^- + \text{Eu}^{152} \rightarrow \nu_e + \text{Sm}^{152*} \rightarrow \nu_e + \text{Sm}^{152} + \gamma$. Because of conservation of angular momentum, the polarization of the gammas emitted in the direction of the samarium momentum, opposite the direction of the neutrinos, is equal to the helicity of the neutrino. They placed an Eu^{152} source in an electromagnet with an alternating field. The emitted gamma rays are resonantly scattered on Sm_2O_3 and detected by a scintillation counter with a photomultiplier tube. They found that the gamma rays were circularly polarized with negative helicity, meaning the neutrinos had 100% negative helicity and thus are left-handed.

1.2 Discovery of the muon and tau neutrinos

Nuclear reactors, including the sun, produce electron-type neutrinos. In a 1960 discussion about potential high energy neutrino experiments [14], Lee and Yang proposed the need to determine if the neutrinos in π decay, μ capture, and β decay reactions are all the same particle. In 1962, Lederman, Schwartz, and Steinberger detected muon neutrinos in an experiment at Brookhaven National Laboratory [13]. This was the first accelerator neutrino experiment. 15 GeV protons strike

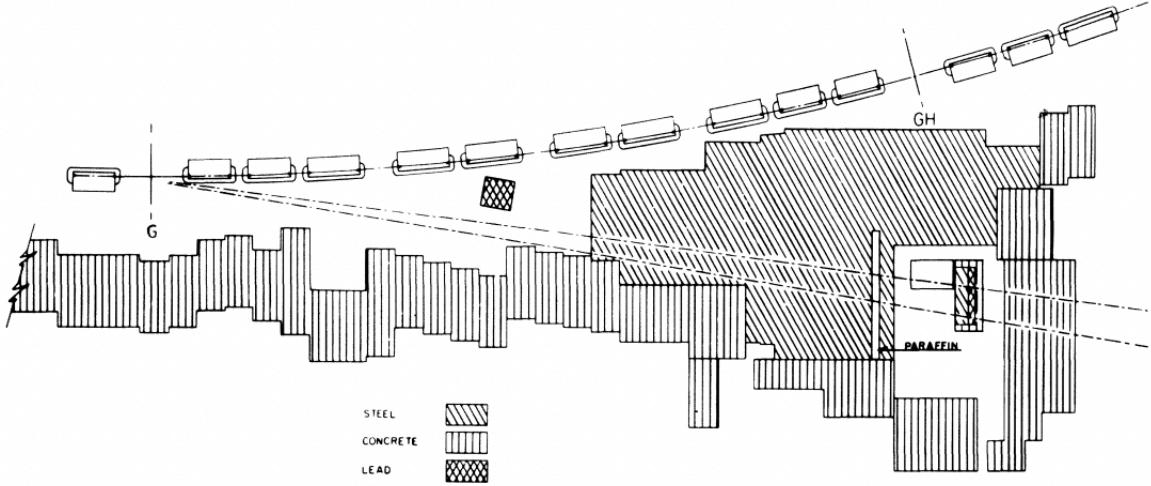


Figure 1.2: From [13], overview of experimental setup at the Brookhaven Alternating Gradient Synchrotron (AGS). The angle from the direction of protons in the beam to the detector is 7.5° . The detector sits behind a 13.5 m iron shield wall.

a beryllium target, producing pions that then decay to muon neutrinos through $\pi^\pm \rightarrow \mu^\pm + \nu_\mu^{(-)}$. The idea behind the experiment was that if there is only one type of neutrino, both muons and electrons should be seen, but if there are multiple types then only muons would be observed in this experiment. A 10 ton aluminum spark chamber detector sat behind a 13.5 m iron shield wall which blocked muons up to 17 GeV. With a total exposure of 3.48×10^{17} protons, they observed 113 events with 56 accepted as neutrino events. There was no evidence of electrons in the data and they concluded that $\nu_\mu \neq \nu_e$. This work earned Leon Lederman, Melvin Schwartz, and Jack Steinberger the Nobel Prize in Physics in 1988.

The third type of lepton, τ , was discovered in 1975 by Perl et al. at the Stanford Linear Accelerator Center. [16]. Since we already knew of the existence of the electron and muon neutrinos, it was natural to assume that ν_τ also exists. The Direct Observation of the NU Tau (DONUT) collaboration set out to observe ν_τ events in an accelerator experiment at Fermilab [15]. A beam of 800 GeV protons interacted with a 1 m tungsten beam dump, producing a variety of particles. The ν_τ 's primarily came from $D_s \rightarrow \tau^- + \bar{\nu}_\tau$ and the resulting τ^- decay. The mean ν_τ energy for interactions was 111 GeV. The DONUT detector setup, following shielding and a scintillator counter veto wall, consisted of emulsion targets interleaved with scintillating fiber planes followed by a charged particle spectrometer for electron and muon identification. The emulsion targets allowed for iden-

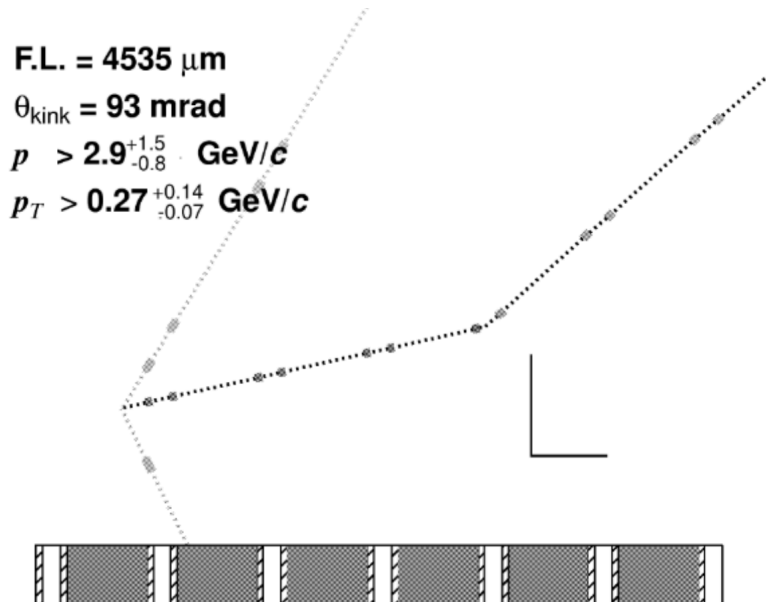


Figure 1.3: From [15], candidate ν_τ event from DONUT. Darkened line exiting the primary vertex is a τ which decays to $e^- + \nu_\tau + \nu_e$ at the location of the kink in the track. Perpendicular lines provide the scale - vertical line is 0.1 mm, horizontal line is 1.0 mm.

tification of τ decay events like the one in Figure 1.3. With a total exposure of 3.54×10^{17} protons, they observed 4 τ decay events and 1 charm decay event, compared to the expected 4.2 τ decay and 0.9 charm decay. The charm decay event passed all of the selection cuts except for one; it had an electron track coming from the interaction vertex.

Why stop looking after this? Could there possibly be a fourth lepton and a corresponding fourth neutrino? Fortunately, the width of the Z boson has a dependence on the number of active neutrinos so we can answer this question without hunting for more particles. If there are more neutrinos, the total Z width increases, thus decreasing the cross section. A combination of Large Electron Positron Collider (LEP) experiments have measured the $e^+e^- \rightarrow \text{hadrons}$ cross section as a function of center of mass energy. The combined results are in Figure 1.4. The data fits the 3ν theoretical line, so we can conclude there are only 3 active flavors of neutrino which have masses lighter than the Z boson.

The experiments discussed thus far have used neutrino sources local to the earth - either by creating a beam of neutrinos using a particle accelerator or employing a radioactive source like a nuclear reactor. The sun is also a source of neutrinos. It produces electron neutrinos through a variety of fusion processes from the proton-proton chain to the carbon-nitrogen-oxygen cycle. Beginning in the late 1960s, a variety of detectors were built to observe solar neutrinos. Water

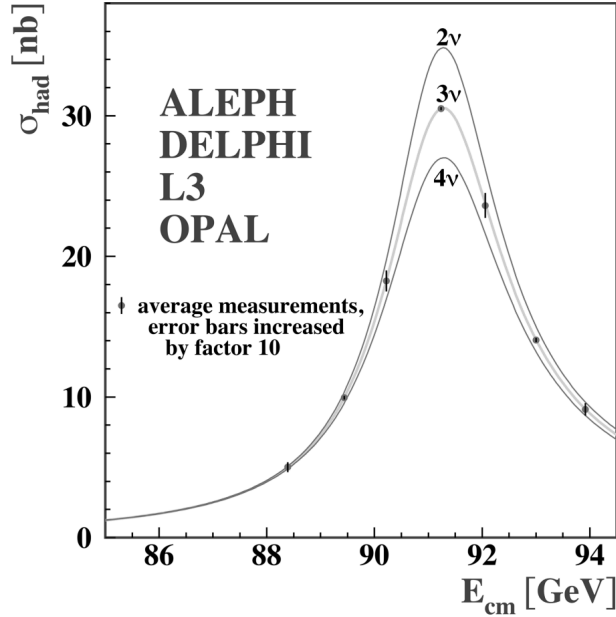


Figure 1.4: From [17], average value of $e^+e^- \rightarrow \text{hadrons}$ cross section as a function of center of mass energy from LEP experiments ALEPH, DELPHI, L3, and OPAL. Error bars increased by a factor of ten for visibility. The data match the theoretical three neutrino curve.

Cherenkov and chlorine-based detectors are sensitive to neutrinos coming from ${}^8\text{B}$ decay, while gallium detectors are sensitive to the lower energy neutrinos from the proton-proton chain.

In the late 1960s, the Homestake Solar Neutrino Detector [18] was built in the Homestake Mine in South Dakota to observe ${}^8\text{B}$ decay neutrinos from the sun via the inverse beta decay reaction, $\nu_e + {}^{37}\text{Cl} \rightarrow {}^{37}\text{Ar} + e^-$. The detector was a tank placed 1478 m underground and filled with 615 metric tons of C_2Cl_4 . 5% of the tank volume was filled with helium gas. The helium was used to remove argon from the tank, carrying it to a cryogenically cooled absorber that trapped the argon while allowing the helium to pass back through to the detector. The amount of ${}^{37}\text{Ar}$ extracted was determined by observing their decay in a proportional counter. The number of ${}^{37}\text{Ar}$ atoms observed, combined with detection and extraction efficiencies is equal to the number of neutrino interactions that occurred in the tank. Over the course of 24 years, 108 solar neutrinos were observed. The resultant solar neutrino rate was about $\frac{1}{3}$ of the expected rate based on solar model predictions. Multiple cross-checks were performed to confirm the efficiency of argon extraction and measure expected background rates to try to explain the low rate and although no errors were found, this result remained unconfirmed for many years. This work did eventually earn Raymond Davis the

Nobel Prize in Physics in 2002.

While it was originally built to search for proton decay, the upgraded Kamioka Nucleon Decay Experiment (Kamiokande-II) [19], located in the Kamioka Mine in Japan, was also sensitive to solar neutrinos originating from ^8B decay. The water Cherenkov Kamiokande-II detector contained 2140 tons of water and had 948 20 in photomultiplier tubes for collecting light. Kamiokande-II could record the energy of contained events, along with the direction of the incoming neutrino. They saw an obvious signal coming from the direction of the sun (Figure 1.5), but observed 46% of the solar flux prediction. These results are consistent with those of the Homestake Mine experiment. This work earned Masatoshi Koshiba the Nobel Prize in Physics in 2002.

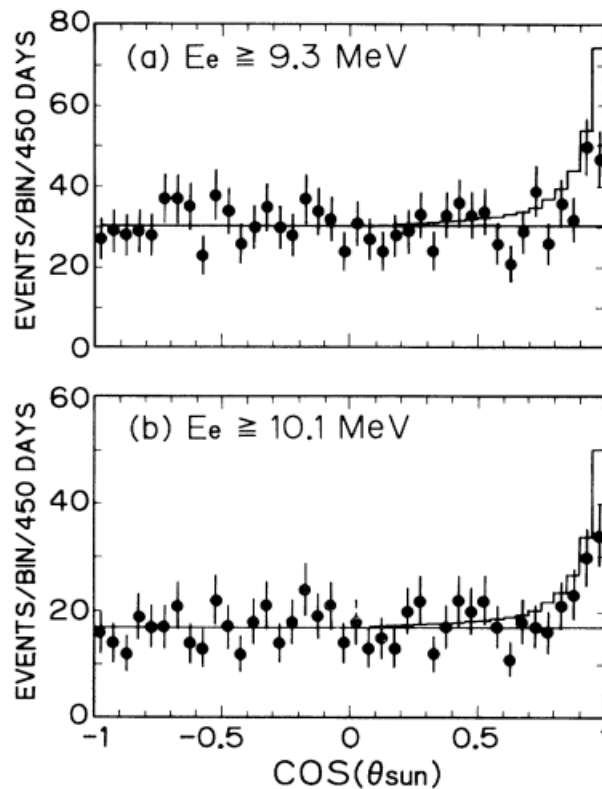


Figure 1.5: From [19], distributions of the cosine of the angle between electron trajectory and the direction of the sun in neutrino events in the Kamiokande-II detector, split up by electron energy. Electrons that point straight back to the sun have $\text{cos } \theta_{\text{sun}} = 1$.

The predicted neutrino flux from the proton-proton chain is largely related to the luminosity of the sun, and therefore less dependent on the specifics of the solar model used than the flux from ^8B decay. In the 1990s, the Russian-American Gallium Experiment (SAGE) [20], located in the Baksan

Neutrino Observatory in Russia, and the Gallium Experiment (Gallex) [21], located in the Laboratori Nazionali del Gran Sasso in Italy, both recorded the flux of solar neutrinos from the proton-proton chain. They employed the neutrino capture reaction ${}^{71}\text{Ga} + \nu_e \rightarrow {}^{71}\text{Ge} + e^-$ using GaCl_2 as a target. The germanium was extracted via an oxidation reaction, turned into gaseous GeH_4 , and placed in a proportional counter to determine how much total germanium was extracted. SAGE saw about 50% of the predicted solar flux, and Gallex saw about 60%. The Gallium Neutrino Observatory (GNO) [22], a continuation of Gallex, saw a similar result. Since the proton-proton neutrino flux was missing a similar amount as the ${}^8\text{B}$ decay neutrino flux this could not be attributed to an incorrect model of the ${}^8\text{B}$ decay within the solar model. These results, combined with the lower fluxes seen by the Homestake Mine and Kamiokande experiments pointed to evidence of unknown physics.

1.3 Neutrino Oscillations

The question still remained: Were all of these experiments flawed such that they recorded fewer neutrinos than expected, was there a problem with the solar flux models, or was there some physics explanation for the discrepancy? The concept of neutrino oscillations, or mixing, was formalized by Pontecorvo, Gribov [23], Maki, Nakagawa, and Sakata [24]. Although we detect neutrinos in their flavor eigenstates, ν_e , ν_μ , and ν_τ , they travel through space in their mass eigenstates, ν_1 , ν_2 , and ν_3 , which are linear combinations of the flavor eigenstates. This means that while solar neutrinos all start out as ν_e , while traveling to the earth they can oscillate to a different flavor, leading to a deficit in the number of ν_e detected. To transform from one basis to the other, we use a unitary rotation matrix commonly referred to as the PMNS matrix after Pontecorvo, Maki, Nakagawa, and Sakata.

$$\begin{pmatrix} \nu_e \\ \nu_\mu \\ \nu_\tau \end{pmatrix} = U_{\text{PMNS}} \begin{pmatrix} \nu_1 \\ \nu_2 \\ \nu_3 \end{pmatrix} \quad (1.1)$$

The matrix contains three rotation angles, θ_{12} , θ_{13} , and θ_{23} , commonly referred to as the mixing angles, and a potentially non-zero charge-parity (CP) violating phase, δ_{CP} . In its factored form, the

PMNS matrix is

$$U_{\text{PMNS}} = \begin{pmatrix} 1 & 0 & 0 \\ 0 & \cos \theta_{23} & \sin \theta_{23} \\ 0 & -\sin \theta_{23} & \cos \theta_{23} \end{pmatrix} \begin{pmatrix} \cos \theta_{13} & 0 & \sin \theta_{13} e^{-i\delta_{\text{CP}}} \\ 0 & 1 & 0 \\ -\sin \theta_{13} e^{i\delta_{\text{CP}}} & 0 & \cos \theta_{13} \end{pmatrix} \begin{pmatrix} \cos \theta_{12} & \sin \theta_{12} & 0 \\ -\sin \theta_{12} & \cos \theta_{12} & 0 \\ 0 & 0 & 1 \end{pmatrix}. \quad (1.2)$$

The time evolution for a neutrino flavor state, ν_α , can then be expressed as

$$|\nu_\alpha(t)\rangle = \sum_{j=1,2,3} U_{\alpha j}^* e^{-iE_j t} |\nu_j\rangle, \quad (1.3)$$

where ν_j is each neutrino mass eigenstate, $U_{\alpha j}^*$ is the corresponding element of the PMNS matrix, and E_j is the neutrino energy. The probability of oscillation from flavor state ν_α to ν_β in vacuum, with $\hbar = c = 1$, is

$$P\left(\nu_\alpha^{(-)} \rightarrow \nu_\beta^{(-)}\right) = \delta_{\alpha\beta} - 4 \sum_{i>j} \Re(U_{\alpha i}^* U_{\beta i} U_{\alpha j} U_{\beta j}^*) \sin^2\left(\Delta m_{ij}^2 \frac{L}{4E}\right) \pm 2 \sum_{i>j} \Im(U_{\alpha i}^* U_{\beta i} U_{\alpha j} U_{\beta j}^*) \sin\left(\Delta m_{ij}^2 \frac{L}{4E}\right), \quad (1.4)$$

where the mass splitting $\Delta m_{ij}^2 \equiv m_i^2 - m_j^2$ with $m_{i,j}$ representing the mass eigenstates, L is the distance the neutrino travels, and E is the neutrino energy. Since the probability of neutrino oscillation depends on the mass splittings, the existence of oscillations would imply neutrinos have nonzero mass. Additionally, because of the sign difference for neutrinos versus antineutrinos, the probability of $\nu_\alpha \rightarrow \nu_\beta$ will differ from $\bar{\nu}_\alpha \rightarrow \bar{\nu}_\beta$ if U_{PMNS} has an imaginary part due to a nonzero CP violating phase δ_{CP} .

The neutrinos we detect do not just travel through the vacuum of space. We need to be able to account for forward scattering in the higher densities of the sun and the earth, and to a lesser extent the density of the atmosphere. All neutrino flavors are subject to neutral current reactions with electrons in matter. Since this is common to all flavors, it adds a phase to the neutrino oscillation probability that can be ignored. $\nu_e^{(-)}$ can also undergo charged current interactions with the electrons. This requires adding a matter potential into the Hamiltonian for (anti)neutrinos, $V = \pm\sqrt{2}G_F N_e$, where G_F is the Fermi constant and N_e is the electron number density. The matter potential leads to new effective masses and mixing angles for the neutrinos, since ν_e contributes

to each mass eigenstate. This affects the oscillation probabilities and can lead to an enhancement of oscillations compared to the probability without accounting for matter. The effect is opposite for neutrino versus antineutrino oscillations since in both cases the (anti)neutrinos pass through matter, rather than antimatter.

1.3.1 Experimental Evidence of Neutrino Oscillations

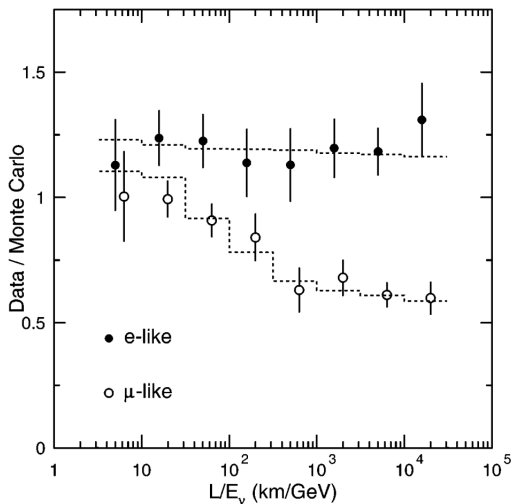


Figure 1.6: From [25], the ratio of fully contained events in data to Monte Carlo events assuming no oscillations versus L/E_ν . A ratio of 1 would imply data matches the no-oscillation assumption. Dashed lines show expected shape assuming $\nu_\mu \leftrightarrow \nu_\tau$ oscillations with $\Delta m^2 = 2.2 \times 10^{-3} \text{ eV}^2$ and $\sin^2 2\theta = 1$.

The upgrade to Kamiokande-II, Super-Kamiokande (Super-K), is a 50 kt water Cherenkov detector viewed by 11,146 50 cm photomultiplier tubes (PMTs) with an additional 1885 8 in veto PMTs around the outside. Super-K detected both solar and atmospheric neutrinos [25, 26]. It was able to measure the energy of contained events and, since the energy spectrum of neutrinos depends on the oscillation probability, it could therefore provide measurements of some parameters in the PMNS matrix. Decays of cosmic rays in the atmosphere produce both muon and electron neutrinos with an expected ratio of $\nu_\mu/\nu_e \approx 2$. A significant deviation from 2 could be evidence of neutrino oscillations. The observed ν_μ/ν_e ratio and zenith angle distribution was consistent with $\nu_\mu \rightarrow \nu_\tau$ oscillations, with $\sin^2 2\theta_{13} > 0.82$ and $5 \times 10^{-4} \text{ eV}^2 < \Delta m_{31}^2 < 6 \times 10^{-3} \text{ eV}^2$. Figure 1.6 shows the ratio of the ν_e and ν_μ -like interactions in the detector to Monte Carlo assuming no oscillations. A study of recorded solar neutrinos from ${}^8\text{B}$ decay similarly confirmed evidence of neutrino oscillations. The latest results

from Super-K prefer normal mass ordering with $\sin^2 \theta_{23} = 0.588_{-0.064}^{+0.031}$, $\Delta m_{32}^2 = 2.50_{-0.20}^{+0.13} \times 10^{-3} \text{ eV}^2$, and $\delta_{\text{CP}} = 1.33_{-0.51}^{+0.45} \pi$ [27]. This work earned Takaaki Kajita the Nobel Prize in Physics in 2015.

The Sudbury Neutrino Observatory (SNO) [28] similarly detects solar neutrinos from ^8B decay. SNO was a heavy water Cherenkov detector containing 1000 metric tons of D_2O in a 12 m diameter sphere, surround by a pure H_2O shield and viewed by 9,456 20 cm PMTs. SNO compared the solar neutrino flux of charged current (ϕ^{CC} , $\nu_e + d \rightarrow p + p + e^-$) and elastic scattering (ϕ^{ES} , $\nu_\ell + e^- \rightarrow \nu_\ell + e^-$) events. Comparing ϕ^{CC} to ϕ^{ES} can provide evidence of neutrino oscillations independent of solar flux models; if $\phi^{\text{CC}} < \phi^{\text{ES}}$, solar neutrinos must change from ν_e to other flavors. SNO's measurement of ϕ^{ES} was consistent with Super-K's result, and the measurement of ϕ^{CC} was significantly smaller, indicating there must be a non-electron contribution to the solar neutrino flux. This work earned Arthur McDonald the Nobel Prize in Physics in 2015.

1.4 A review of other neutrino experiments

Since the discovery of neutrino oscillations by Super-K and SNO, many experiments have made measurements of the neutrino mixing parameters. Neutrino experiments can probe different neutrino mixing parameters depending on the neutrino source used and the distance the neutrinos travel. The experiments can be broken into four main categories: solar, atmospheric, reactor, and accelerator neutrino experiments, although there is some overlap between these categories.

Many of the solar neutrino experiments were already described. The remaining one, Borexino, was designed to measure solar neutrinos from ^7Be decay [29, 30], although it has also measured the flux from ^8B [31], the proton-proton chain [32], and the carbon-nitrogen-oxygen (CNO) cycle [33]. Located in the Laboratori Nazionali del Gran Sasso in Italy, Borexino is a spherical liquid scintillator detector viewed by PMTs with a fiducial volume weighing 100 tons, shielded by ultra-pure water to reduce backgrounds from gamma rays and neutrons in the rock surrounding the detector. Borexino was the first experiment to detect neutrinos coming from the CNO cycle in the sun.

IceCube/DeepCore [34] is an atmospheric neutrino experiment. IceCube is an ice Cherenkov detector with strings of PMTs in columns in the ice near the south pole spanning an area of 1 km^2 . The central DeepCore region is more densely populated with PMTs and about 50% of them have a higher quantum efficiency, enabling detection of lower energy particles. DeepCore is most sensitive

to measuring ν_μ disappearance, which provides information about Δm_{32}^2 and $\sin^2 \theta_{23}$. Super-K also falls into the atmospheric sector.

The reactor experiments are Kamioka Liquid scintillator AntiNeutrino Detector (KamLAND) [35], Double Chooz [36], Daya Bay [37], and Reactor Experiment for Neutrino Oscillations (RENO) [38]. They all detect $\bar{\nu}_e$ from various nuclear reactors via inverse beta decay reactions inside the detectors, looking for prompt positron signals in coincidence with a delayed gamma from neutron capture, the same signal the original Cowan and Reines experiments searched for. KamLAND has the longest baseline, with a single detector located in the Kamioka mine an average of 180 km from various reactors across Japan. The detector is 1 kT of liquid scintillator inside a volume of non-scintillating mineral oil which is, in turn, inside a 3.2 kT water Cherenkov detector. PMTs read out both the inner liquid scintillator detector and the outer cosmic muon veto Cherenkov detector. The longer baseline enables KamLAND to provide precise measurements of $\tan^2 \theta_{12} = 0.436_{-0.025}^{+0.029}$ and $\Delta m_{21}^2 = 7.53_{-0.18}^{+0.18} \times 10^{-5} \text{ eV}^2$, along with a measurement of $\sin^2 \theta_{13} = 0.023_{-0.002}^{+0.002}$.

Double Chooz, Daya Bay, and RENO have similar detectors and baselines. At much shorter baselines than KamLAND, on the order of hundreds of meters rather than kilometers, they provide precise measurements of $\sin^2 2\theta_{13}$. The relative baselines between reactor cores and the various detectors are in Figure 1.7. They consist of concentric cylindrical tanks providing a layered detector, somewhat like an onion. The inner layer contains gadolinium-doped liquid scintillator which serves as the target volume for neutrino interactions. Surrounding that is another layer of liquid scintillator, and then non-scintillating mineral oil to act as a buffer or shield from external backgrounds. PMTs are located on the inner wall of the buffer tank. The outermost layer is a veto tank filled with either pure water (Daya Bay, RENO) or liquid scintillator (Double Chooz) with additional PMTs to act as a veto for cosmic ray muon events.

Daya Bay, located at the Daya Bay Nuclear Power Plant in China, consisted of eight $\bar{\nu}_e$ detectors, one pair about 365 m from two of the reactor cores, another pair about 505 m from the remaining six reactor cores, and four detectors in a far hall an average of 1663 m from all reactors. Values for $\sin^2 2\theta_{13}$ and $\Delta m_{ee}^2 \equiv \cos^2 \theta_{12} \Delta m_{31}^2 + \sin^2 \theta_{12} \Delta m_{32}^2$ are extracted using the $\bar{\nu}_e$ survival probability. Looking at the disappearance probability with 3-flavor oscillations gives a value for Δm_{32}^2 with precision similar to accelerator experiments. Daya Bay provided the first precise measurement of θ_{13} , obtaining a value of $\sin^2 2\theta_{13} = 0.092 \pm 0.016 \text{ (stat.)} \pm 0.005 \text{ (syst.)}$ [40], which was the first

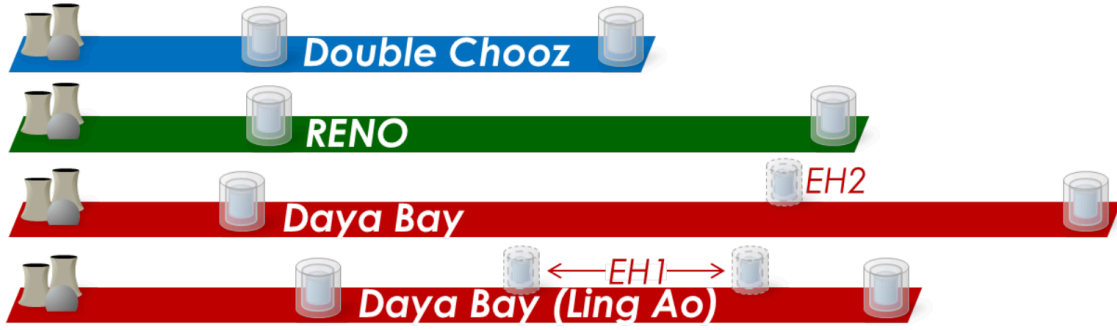


Figure 1.7: From [39], cartoon showing the average baselines for Double Chooz, RENO, and Daya Bay. The two Daya Bay baselines shown are for distances to the Daya Bay Nuclear Power Plant and the Ling Ao Nuclear Power Plant reactor cores. The closest detector for each experiment is about 300-400 m from the reactors. The furthest detectors for each experiment range from about 1000 m to 1700 m away from the reactors.

evidence that θ_{13} was nonzero, as was previously thought could be the case. Daya Bay's latest results were $\sin^2 2\theta_{13} = 0.0856 \pm 0.0029$, $\Delta m_{ee}^2 = 2.522_{-0.070}^{+0.068} \times 10^{-3} \text{ eV}^2$, and $\Delta m_{32}^2 = 2.471_{-0.070}^{+0.068} \times 10^{-3} \text{ eV}^2$ [37].

Double Chooz was located at the Chooz Nuclear Power Plant in Chooz, France. It consisted of two identical detectors located 400 and 1050 m from the reactors. Using external constraints from Daya Bay and RENO for Δm_{ee}^2 and fitting for the rate and shape difference in $\bar{\nu}_e$ events in the near and far detector, Double Chooz reports $\sin^2 2\theta_{13} = 0.105 \pm 0.014$. RENO also has two detectors, located 294 and 1383 m from the center of the reactors at the Hanbit Nuclear Power Plant in Korea. RENO reports a rate-only result for $\sin^2 2\theta_{13}$ of 0.086 ± 0.008 (stat.) ± 0.014 (syst.) with an external constraint for Δm_{ee}^2 along with a rate and spectral result of $\sin^2 2\theta_{13} = 0.0896 \pm 0.0048$ (stat.) ± 0.0047 (syst.) and $\Delta m_{ee}^2 = (2.68 \pm 0.12$ (stat.) ± 0.07 (syst.)) $\times 10^{-3} \text{ eV}^2$.

The final family of experiments is accelerator experiments. For each of these, a beam of primarily muon (anti)neutrinos is produced at an accelerator facility. Neutrinos are detected close to their origin in a near detector and in a far detector following a long baseline over which the neutrinos can oscillate to a different flavor. The experiments vary primarily in detector construction, although specific analysis techniques also differ.

KEK to Kamoika (K2K) [41] was the first long baseline neutrino experiment. It used the KEK proton synchrotron to generate muon neutrinos with an average energy of 1.3 GeV aimed towards the Super-K detector in Kamioka, 250 km away. There were a couple beam monitoring detectors,

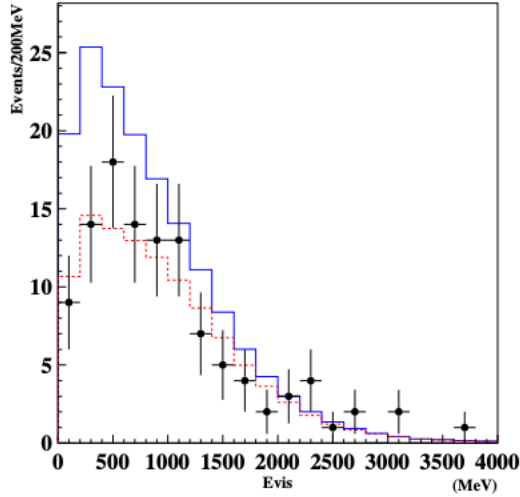


Figure 1.8: From [41], visible energy spectrum of contained K2K events in the Super-K detector. Data points are in black, the solid blue line is the expectation from simulation without neutrino oscillations, and the dashed red line is the expectation from simulation at the best fit point of $\Delta m^2 = 2.8 \times 10^{-3} \text{ eV}^2$ and $\sin^2 2\theta = 1$.

PIMON, placed in the beamline occasionally to measure pion kinematics in the beam, and MUMON, permanently located in the beamline to monitor the beam position. K2K had numerous near detectors. The first was a 1 kT water Cherenkov detector analogous to the far detector, Super-K. Following that was a scintillating fiber detector that provided discrimination between interaction types, then a lead glass calorimeter to tag electromagnetic showers, and finally a muon range detector to measure the energy and other kinematics of muons in ν_μ charged current interactions. The energy spectrum of ν_μ events in K2K is in Figure 1.8. K2K's best fit was $\Delta m^2 = 2.8 \times 10^{-3} \text{ eV}^2$ and $\sin^2 2\theta = 1$.

The Main Injector Neutrino Oscillation Search (MINOS) [42, 43] detectors had alternating planes of steel and plastic scintillator with wavelength fibers that were read out by PMTs. The steel was toroidally magnetized, enabling differentiation between ν_μ and $\bar{\nu}_\mu$. The 0.98 kT near detector was located at Fermilab 1.04 km from the beam target and the 5.4 kT far detector was located in the Soudan Mine in Soudan, MN 735 km from the target. Using the Neutrinos at the Main Injector (NuMI) beam with a peak neutrino energy of about 3 GeV, MINOS had an L/E of about 250 km/GeV. MINOS has done separate analyses of ν_μ disappearance and ν_e appearance. The ν_μ disappearance measurement best fit point is $\sin^2 2\theta_{23} = 0.950_{-0.036}^{+0.035}$ and $\Delta m_{32}^2 = 2.41_{-0.10}^{+0.09} \times 10^{-3} \text{ eV}^2$. For the ν_e appearance measurement, MINOS fixed the values for $\sin^2 2\theta_{23}$, Δm_{32}^2 , and Δm_{21}^2 using external constraints and the values obtained from the ν_μ disappearance measurement and then extracted

values for $2 \sin^2 2\theta_{13} \sin^2 \theta_{23}$ assuming $\delta_{\text{CP}} = 0$ and all combinations of normal/inverted mass ordering and $\theta_{23} < \frac{\pi}{4}$ or $\theta_{23} > \frac{\pi}{4}$. The best fit points for this analysis are $2 \sin^2 2\theta_{13} \sin^2 \theta_{23} = 0.051_{-0.030}^{+0.038}$ for normal mass ordering and $2 \sin^2 2\theta_{13} \sin^2 \theta_{23} = 0.093_{-0.049}^{+0.054}$ for inverted ordering. Additionally, using an external restraint from reactor experiments on $\sin^2 \theta_{13}$, MINOS demonstrated how experiments can combine the ν_{μ} disappearance and ν_e appearance measurements to put constraints on δ_{CP} , the octant of θ_{23} (ie. is $\theta_{23} < \frac{\pi}{4}$ or $\theta_{23} > \frac{\pi}{4}$), and the mass ordering.

The NuMI Off-Axis ν_e Appearance (NOvA) [44] detectors were constructed with low-Z materials to aid in the separation of ν_e charged current events from neutral current events. NOvA also utilizes the NuMI beam at Fermilab, but the detectors were placed off the central axis of the beam so the neutrinos seen in the detectors were more narrowly peaked around 2 GeV, the energy for which neutrino oscillations would be maximized for NOvA's baseline of 810 km. The narrow peak at lower energy also helps to reduce higher energy backgrounds from neutral current events. The NOvA detectors consist of cells of polyvinyl chloride filled with liquid scintillator and wavelength shifting fibers read out by avalanche photodiodes. The planes alternate horizontal and vertical orientation perpendicular to the beam direction which enables three dimensional reconstruction of events. The 293 T Near Detector is located at Fermilab, 1 km from the beam target and the 14 kT Far Detector is located near Ash River, MN, 810 km from the target. See section 2.2 for more details about the NOvA detectors. Using external constraints for Δm_{21}^2 , $\sin^2 \theta_{12}$, and $\sin^2 \theta_{13}$, NOvA reports values for Δm_{32}^2 , $\sin^2 \theta_{23}$, and δ_{CP} with a best fit point at $\Delta m_{32}^2 = (2.41 \pm 0.07) \times 10^{-3} \text{ eV}^2$, $\sin^2 \theta_{23} = 0.57_{-0.04}^{+0.03}$, $\delta_{\text{CP}} = 0.82_{-0.87\pi}^{+0.27\pi}$, and a preference for normal mass ordering and $\theta_{23} > \frac{\pi}{4}$. More details about the latest NOvA analysis and results are in chapter 2.

Tokai to Kamioka (T2K) [45] has a similar setup as NOvA, with off-axis detectors for a narrow beam peaked at about 0.6 GeV. T2K's far detector is the Super-K water Cherenkov detector in the Kamioka Mine described earlier. The beam, generated at the Japan Proton Accelerator Research Complex (J-PARC) in Tokai, Japan, is directed 2.5° away from Super-K. T2K has two near detectors; the first, Interactive Neutrino GRID (INGRID), sits on the beam axis and serves as a beam monitor, while the second, ND280, is located the same amount off-axis as the far detector. ND280 is 280 m from the beam target and Super-K is 295 km from the target. T2K uses external constraints for the same parameters as NOvA does and similarly reports values for Δm_{32}^2 , $\sin^2 \theta_{23}$, and δ_{CP} with a best fit point at $\Delta m_{32}^2 = (2.45 \pm 0.07) \times 10^{-3} \text{ eV}^2$, $\sin^2 \theta_{23} = 0.53_{-0.04}^{+0.03}$, and $\delta_{\text{CP}} = -0.60_{-0.18\pi}^{+0.22\pi}$ with a

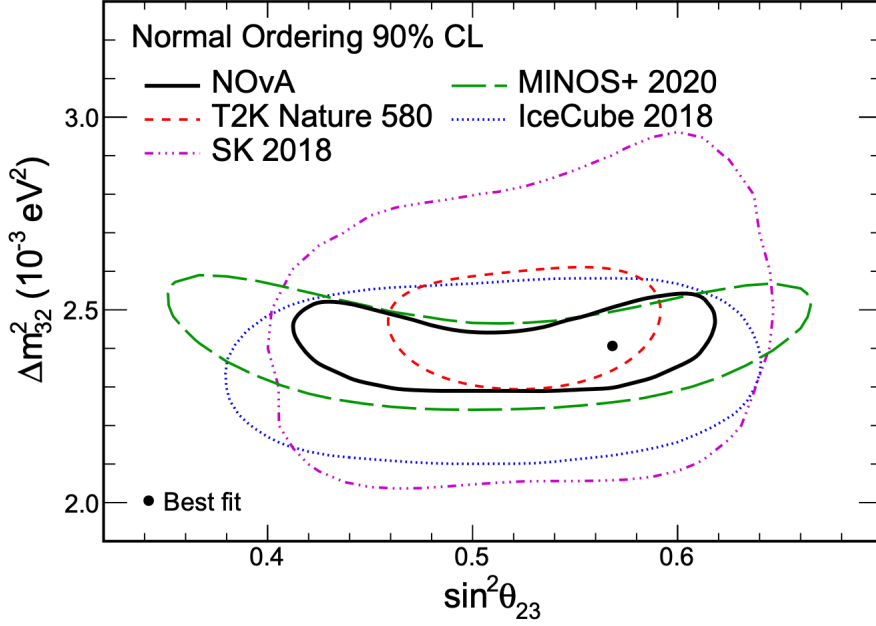


Figure 1.9: 90% confidence level contours for normal mass ordering in Δm_{32}^2 vs. $\sin^2 \theta_{23}$ phase space from [27, 44–47].

preference for normal mass ordering, $\theta_{23} > \frac{\pi}{4}$, and near-maximal CP violation ($\delta_{\text{CP}} \neq 0, \pi$).

Bringing the data from all of these experiments together provides us with our current knowledge of the neutrino mixing parameters. The NuFIT group performs global fits of the available data and provides the neutrino community with the latest values for the PMNS matrix [48]. θ_{12} is measured by solar neutrino and long-baseline reactor neutrino experiments (like KamLAND). θ_{13} has almost exclusively been measured by reactor neutrino experiments, though long-baseline accelerator neutrino experiments can also measure it via ν_e appearance. The final mixing angle, θ_{23} , is measured via ν_μ disappearance in long-baseline accelerator and atmospheric neutrino experiments. The solar mass squared splitting, Δm_{21}^2 , has been measured most precisely by KamLAND, though it can also be determined using solar neutrinos. Reactor and accelerator experiments provide values for Δm_{32}^2 and Δm_{31}^2 ($\Delta m_{32}^2 = \Delta m_{31}^2 - \Delta m_{21}^2$). Current measurements of δ_{CP} come from (ν_e^-) appearance measurements.

The latest global fit values for each of the mixing parameters can be found in Table 3 of [48]. All three mixing angles are non-zero, with $\theta_{13} < \theta_{12} < \theta_{23}$. It is still possible that θ_{23} is exactly $\frac{\pi}{4}$, meaning there is “maximal mixing”, ie. the ν_μ and ν_τ contributions to ν_3 are equal, though data

currently favors $\theta_{23} > \frac{\pi}{4}$. We know $m_2 > m_1$ and $\Delta m_{21}^2 \ll \Delta m_{23}^2$. The sign of Δm_{23}^2 is still unknown - a positive (negative) sign would confirm normal (inverted) mass ordering - though existing data prefers normal mass ordering. The final unknown parameter is δ_{CP} . If non-zero, it will confirm the existence of CP violation in the lepton sector. Beyond these unknown parameters, we also still do not know the absolute values for neutrino masses.

Chapter 2

NOvA

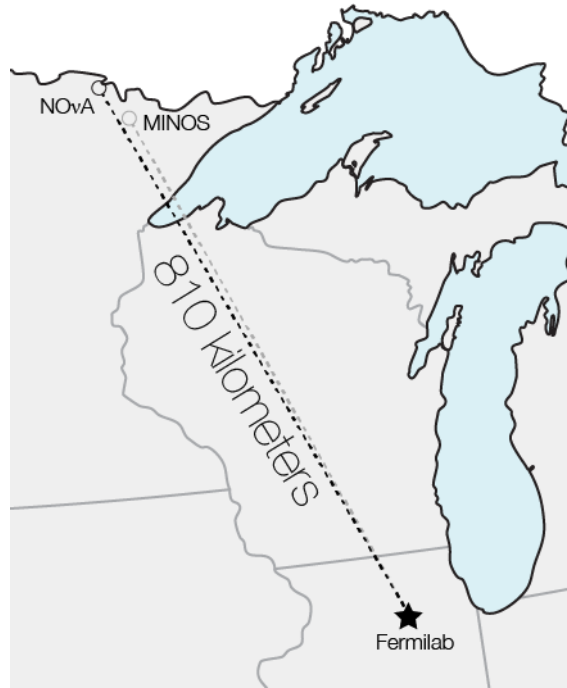


Figure 2.1: Map of NOvA experiment layout. The NuMI beam and NOvA Near Detector are located at Fermilab while the Far Detector is located 810 km away in northern Minnesota. The location of the MINOS Far Detector in Soudan, MN at a baseline of 735 km is also shown.

The NuMI Off-axis ν_e Appearance experiment (NOvA) is a two detector, long baseline, neutrino oscillation experiment designed to study $\bar{\nu}_\mu \rightarrow \bar{\nu}_e, \bar{\nu}_\mu$ oscillations. It utilizes the NuMI beam at Fermilab, which is a high intensity beam composed of primarily muon (anti)neutrinos. NOvA uses data from a Near Detector onsite at Fermilab at a baseline of 1 km to predict the spectrum of events visible at the Far Detector near Ash River, MN at a baseline of 810 km. To determine the neutrino mixing parameters, we measure the energy spectra of ν_μ and ν_e events in our Far Detector (after oscillations) and compare to the expected spectra for various values of the mixing parameters. This full process is explained more in section 2.4, but simplified forms of Equation 1.4 are below to enable a discussion about which parameters NOvA has sensitivity to. When extracting the parameters, we use the full forms of the oscillation probabilities. Simplifying for the two neutrino case relevant to

NOvA we get, for ν_μ disappearance:

$$P\left(\nu_\mu^{(-)} \rightarrow \nu_\mu^{(-)}\right) \approx 1 - \sin^2 2\theta_{23} \sin^2 \left(\frac{\Delta m_{32}^2 L}{4E} \right). \quad (2.1)$$

For ν_e appearance all three mixing angles and mass squared splittings are relevant [49]:

$$P\left(\nu_\mu^{(-)} \rightarrow \nu_e^{(-)}\right) \approx P_{\text{atm}} + P_{\text{sol}} + 2\sqrt{P_{\text{atm}}P_{\text{sol}}} \cos \left(\frac{\Delta m_{32}^2 L}{4E} \pm \delta_{\text{CP}} \right),$$

$$\text{with } P_{\text{atm}} = \sin^2 \theta_{23} \sin^2 2\theta_{13} \sin^2 \left(\frac{\Delta m_{31}^2 L}{4E} \right), \quad (2.2)$$

$$P_{\text{sol}} = \cos^2 \theta_{23} \cos^2 \theta_{13} \sin^2 2\theta_{12} \sin^2 \left(\frac{\Delta m_{21}^2 L}{4E} \right).$$

Constraints from solar and reactor experiments provide us with higher precision than we could obtain for θ_{13} and θ_{12} , so we fix these parameters using external constraints and use them as inputs to NOvA's measurements. Both disappearance and appearance measurements have sensitivity to Δm_{32}^2 and θ_{23} . The ν_μ disappearance measurement has higher statistics and so it is more precise, but since it depends on $\sin^2 2\theta_{23}$ this measurement only tells us how close θ_{23} is to $\frac{\pi}{4}$, not whether it is less than or greater than $\frac{\pi}{4}$. To determine the octant of θ_{23} , i.e. whether $\theta_{23} < \frac{\pi}{4}$ or $\theta_{23} > \frac{\pi}{4}$, we turn to the ν_e appearance measurement, which depends on $\sin^2 \theta_{23}$, without the extra factor of 2. The ν_e appearance measurement also has sensitivity to the sign of Δm_{32}^2 , which tells us what the mass ordering is, and to δ_{CP} , which tells us if neutrinos exhibit CP violation.

2.1 NuMI Beam

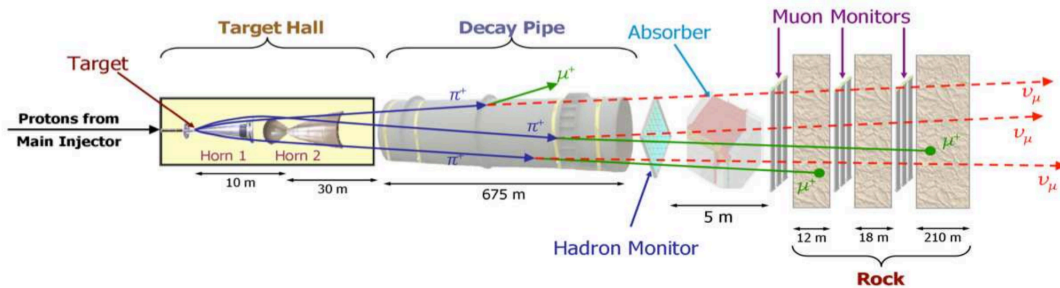


Figure 2.2: From [50], NuMI beam components not drawn to scale.

The Neutrinos at the Main Injector (NuMI) beam uses 120 GeV protons extracted from Fermilab’s Main Injector to produce charged mesons that decay to primarily muon (anti)neutrinos. For more details about how the protons are generated and accelerated, see section 3.1. For NOvA, NuMI runs in the medium energy configuration discussed in [50]. A schematic of the NuMI beamline is in Figure 2.2. Following extraction, the protons are directed slightly downwards towards a graphite target, 350 m from the extraction point. Protons interacting in the target generate charged mesons. Following the target, a pair of parabolic magnetic focusing horns act as lenses to focus charged particles of the desired sign for (anti)neutrino mode. Focused mesons travel through a 2 m diameter, 675 m long decay pipe filled with helium to minimize interactions prior to decay. The primary source of neutrinos in the NuMI beamline are pion decays ($\pi^+ \rightarrow \mu^+ \nu_\mu$ 99.99%) and kaon decays ($K^+ \rightarrow \mu^+ \nu_\mu$ 63.56%). Kaon decays also generate ν_e with a branching ratio of about 5%, leading to an inherent ν_e background in the beam. Most remaining charged particles are stopped by an aluminum, steel, and concrete absorber downstream of the decay pipe. There is an additional 240 m dolomite muon shield to range out any remaining muons in the beam prior to reaching the Near Detector. The NOvA detectors were placed 14.6 mrad away from the central axis of the beam, or

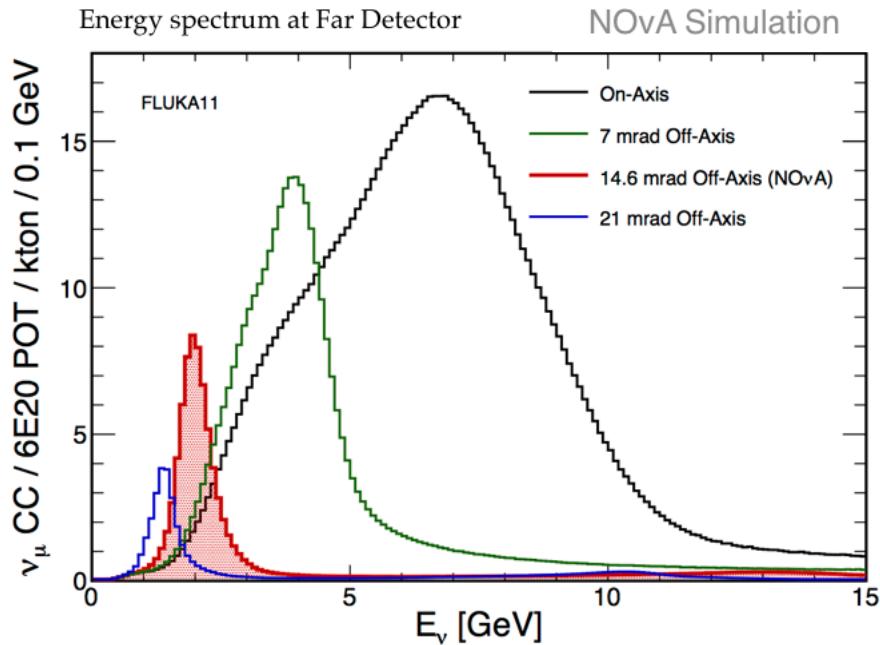


Figure 2.3: Neutrino energy spectra that would be seen by the NOvA Far Detector for various off-axis angles. The NOvA detectors are located 14.6 mrad off-axis.

14.6 mrad “off-axis”. The neutrino energy spectra for different off-axis locations are in Figure 2.3.

On the beam axis, the neutrino energy spectrum is broad and peaks around 7 GeV. As the detector location moves further off-axis, the peak shifts to a lower energy and narrows. For NOvA’s baseline of 810 km, the first oscillation maximum occurs around 2 GeV. At an off-axis angle of 14.6 mrad, NOvA sees a larger amount of 2 GeV neutrinos than if it were on-axis. The off-axis location has the added benefit of decreasing backgrounds from higher energy neutral current (NC) events which can mimic ν_e events in the detectors. The resultant neutrino flux seen in the NOvA Near Detector is in Figure 2.4. Since we cannot directly measure the neutrino flux, we use the number of protons-on-target (POT) to report beam intensity. The total number of neutrino interactions we expect is directly correlated with the total POT we record. Figure 2.5 displays the accumulated POT for which our Far Detector was recording data used in the most recent NOvA oscillation analysis.

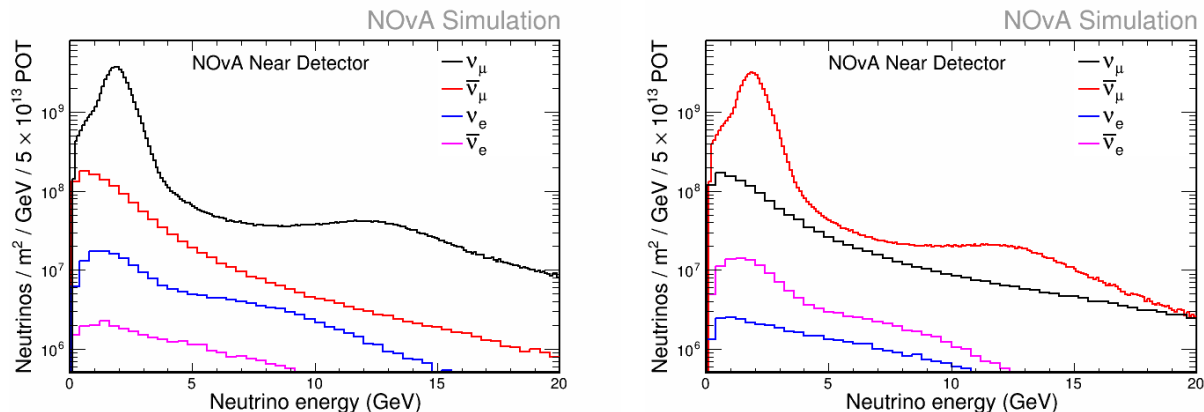


Figure 2.4: Neutrino flux at the Near Detector for neutrino mode (left) and antineutrino mode (right). Between 1 and 5 GeV the ν_μ ($\bar{\nu}_\mu$) beam is 93% (92%) pure.

2.2 NOvA Detectors

The Near Detector, located at Fermilab, 1 km from the NuMI target, is 100 m underground. It is 3.9 m × 3.9 m × 15.9 m, with the longest dimension going along the length of the detector, roughly parallel to the beam. The Far Detector is located 810 km from the target, near Ash River, Minnesota. The Far Detector is not underground, but has a modest overburden of 3.6 meters water equivalent. It is much larger than the Near Detector, measuring 15 m × 15 m × 60 m. Both detectors have the same basic design: they are composed of planes of extruded polyvinyl chloride (PVC) cells measuring 4 cm × 6 cm × the height or width of the detector. The cells are grouped in planes that alternate horizontal and vertical orientations, perpendicular to the length of the detector. To resolve ν_e events

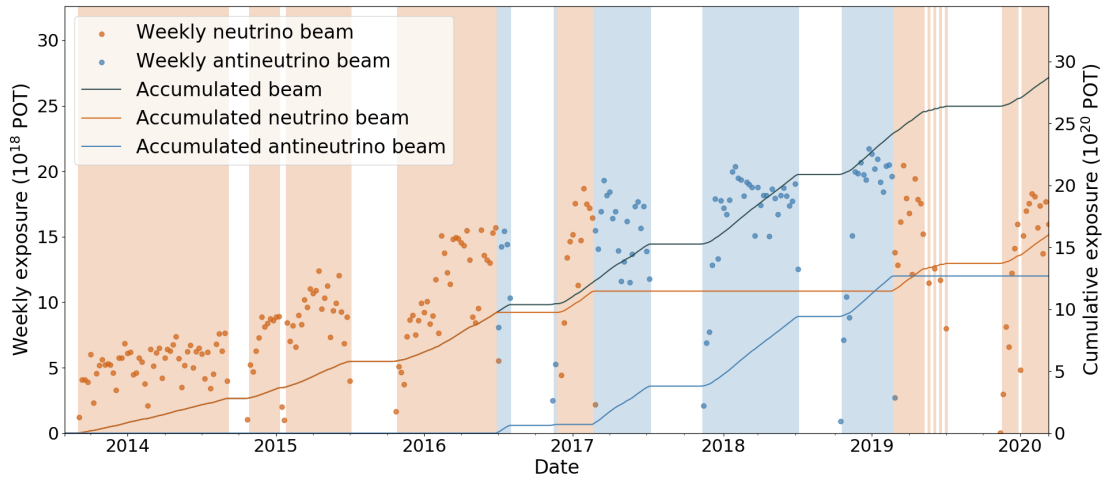


Figure 2.5: Weekly protons-on-target (POT) recorded by the NOvA Far Detector from February 2014 to March 2020. Data taken in (anti)neutrino mode is displayed in orange (blue). The long gaps each year are due to Fermilab’s summer beam shutdown. Total exposure: 13.6×10^{20} in ν mode and 12.5×10^{20} in $\bar{\nu}$ mode.

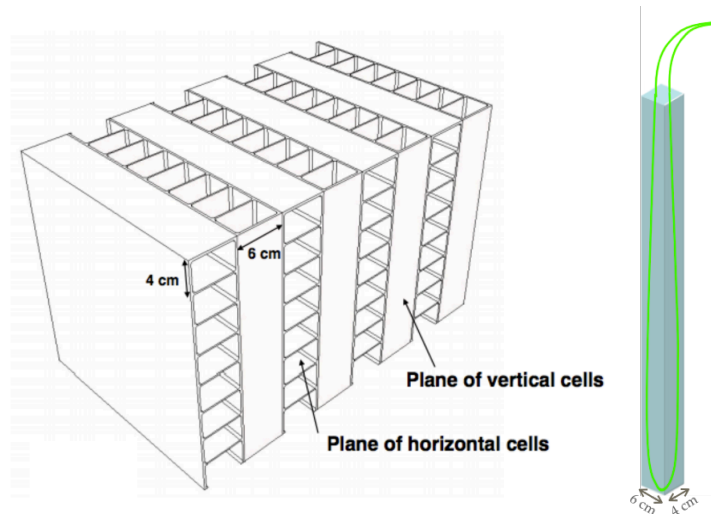


Figure 2.6: Left: Schematic of NOvA detector planes with alternating horizontal and vertical planes of cells. Right: Schematic of single NOvA cell. Each cell has a cross-section of $4 \times 6 \text{ cm}^2$ and a wavelength shifting fiber looped through the length of the cell.

in the detectors, NOvA was constructed with low-Z materials. With a radiation length of 37.5 cm, electrons will pass through an average of 5 cells before pair producing. The PVC is loaded with TiO_2 to increase reflectivity within each cell [51]. Each cell is filled with liquid scintillator and an optical wavelength shifting fiber which carries light to the readout electronics. The final 3 m of the Near Detector consists of ten 10 cm thick planes of steel interleaved with pairs of PVC planes to range out muons. The Test Beam Detector is described more in section 3.3, but is mentioned in comparisons between detectors in this section.

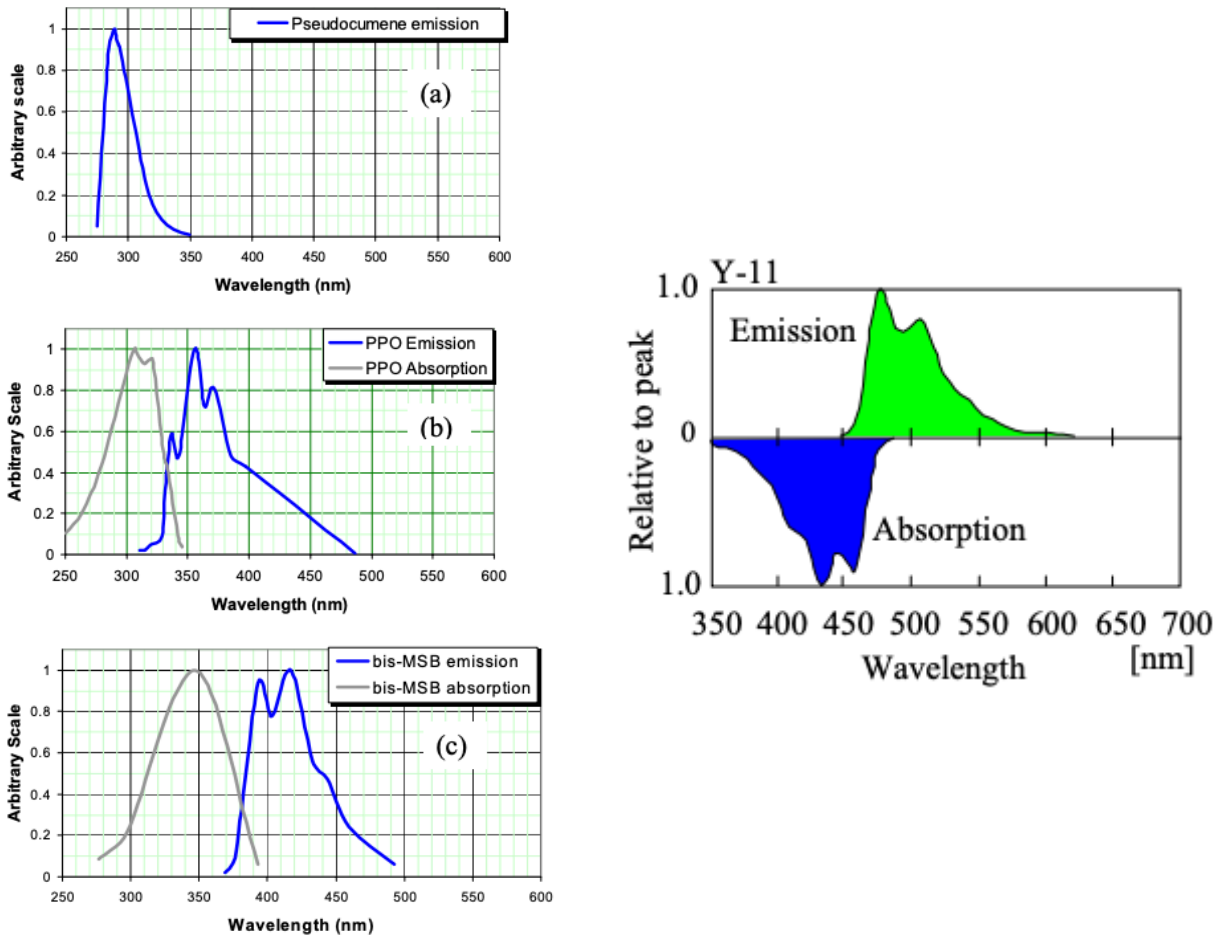


Figure 2.7: From [52]. Left: absorption and re-emission spectra for the primary scintillant, pseudocumene, and wavelength shifters, PPO and bis-MSB, present in the NOvA liquid scintillator. Right: the absorption and re-emission spectrum for the dye used in the wavelength shifting fiber.

The scintillator is mostly mineral oil, doped with a scintillant (pseudocumene) and wavelength shifters (PPO and bis-MSB) [53]. A charged particle passing through the scintillator will produce near ultraviolet light which is then shifted to 380-450 nm. Each cell has a wavelength shifting (WLS)

fiber looped in it (see Figure 2.6) which absorbs light in the violet to blue range and emits it in the blue to green 450-600 nm range. Both ends of the WLS fiber are read out by a single pixel in an avalanche photodiode (APD). The absorption and emission spectra for the various wavelength shifters used are in Figure 2.7.

Light from the APD is digitized by a custom front end board (FEB). The Far Detector is outfitted with v4 FEBs, using the v4.10.2E firmware, and the Near Detector is outfitted with v5 FEBs, using the V5.21.0E firmware. The v5 FEBs have faster timing, due to a higher order multiplexing, which helps deal with pileup in the Near Detector beam events. The FEBs continuously read out signal from the detector cells, with individual readings spaced 500 (125) ns apart for the v4 (v5) FEBs. Thresholds are set for each cell in the detectors using a Digital Scanning Oscilloscope, or pedestal, scan. For each pixel on an APD/FEB pair, we take 4096 readings of (ADC, TDC) pairs. From the resulting spectrum, we can extract the baseline and variation from that baseline. The actual value of the baseline does not matter for setting the threshold, but we use it as input for our simulation. To set the threshold, we find the standard deviation, σ_{DCS} , of a dual correlated sample, defined as $\text{ADC}[i] - \text{ADC}[i-3]$, where $\text{ADC}[i]$ is the current reading of charge on the pixel and $\text{ADC}[i-3]$ is the reading of charge 3 samples earlier. The threshold for each cell is then set at $4(5) \times \sigma_{\text{DCS}}$ for the Far (Near, Test Beam) Detector. As the FEB digitizes signal from the APD, if $\text{ADC}[i] - \text{ADC}[i-3] > \text{threshold}$, then the (ADC, TDC) information for four readings 0-3, where 2 is the reading that exceeded threshold, are sent to a Data Concentrator Module (DCM). Each DCM receives data from up to 64 FEBs. The DCM packages together information from the FEBs into 50 μs microslices. The microslices are then combined into 5 ms long millislices that are then sent to a machine in the buffer farm. All the buffer nodes run an event builder that collates the information from all the DCMs on the detector – 168, 14, and 3 for the Far, Near, and Test Beam detectors, respectively. Once the data is on a buffer node, we either decide to save it to disk based on a few types of triggers, or we allow it to fall off the end of a circular buffer without saving the information. For the Far, (Near and TestBeam) Detectors, the buffer is about 20 (30) minutes long.

The NuMI beam is sent in 10 μs pulses, spaced about 1.2-1.5 s apart. If data occurs coincident with the beam, we save a window around the time we expect beam to enter our detectors. Signal from the Accelerator Division (AD) at Fermilab is sent through cables directly connected to a timing unit onsite. This Timing Distribution Unit (TDU) forwards the beam spill timing information to the

trigger system on each detector’s Data Acquisition (DAQ) system. Upon receiving this information, the DAQ uses configuration information to determine the offset and length of the trigger to write out. Both the Near and Far Detectors record 550 μs of data each time they receive a NuMI trigger. We have a pulsed trigger that records 550 μs of data at a rate of 10 (1) Hz for the Far (Near and Test Beam) Detector. We also have the ability to run basic reconstruction on the data prior to writing it to disk and use data-driven triggers (DDTs) to determine if we should save the data. We create clusters of hits and form tracks and if they meet certain criteria, we save the data to disk. For the Near and Far Detectors we also have external triggers that allow us to subscribe to alerts from the SuperNova Early Warning System (SNEWS) [54] and LIGO/Virgo alerts through NASA’s Gamma-ray Coordinates Network (GCN) [55]. In each case, we write out 45 s of data starting 5 s before the event time passed to the DAQ.

2.3 Event Reconstruction and Selection

Energy depositions in detector cells during each readout window, or event, are recorded as (time, charge) ‘hits’. Hits are clustered together based on time and space. For each cluster of hits, reconstruction algorithms determine the most likely location of an interaction vertex and further divide the hits into groups pointing away from the vertex in ‘prongs’. We start with over one billion events coincident with the NuMI beam at each detector and apply a variety of beam and detector quality and selection cuts to narrow these down to $\mathcal{O}(2 \times 10^6)$ (anti)neutrino interaction candidates in the Near Detector and $\mathcal{O}(400)$ (anti)neutrino interaction candidates in the Far Detector.

Beam quality cuts zoom in further on the 10 μs pulse of the NuMI beam and check the quality of the beam for each event using variables such beam width and position, horn current, and POT per beam spill. Detector quality cuts ensure all parts of the detector were reporting and in time with each other. Containment criteria require The vertex to be far enough away from all edges of the detector so energy from the outgoing particles is contained within the detector.

A Boosted Decision Tree (BDT) rejects cosmogenic events. A Convolutional Neural Network (CNN) classifies events as ν_e charged current, ν_μ charged current, neutral current, or cosmogenic background. Energy of the selected neutrino interactions is found differently for the two flavors. For ν_μ interactions, the muon is identified using a BDT and its energy is calculated based on its range.

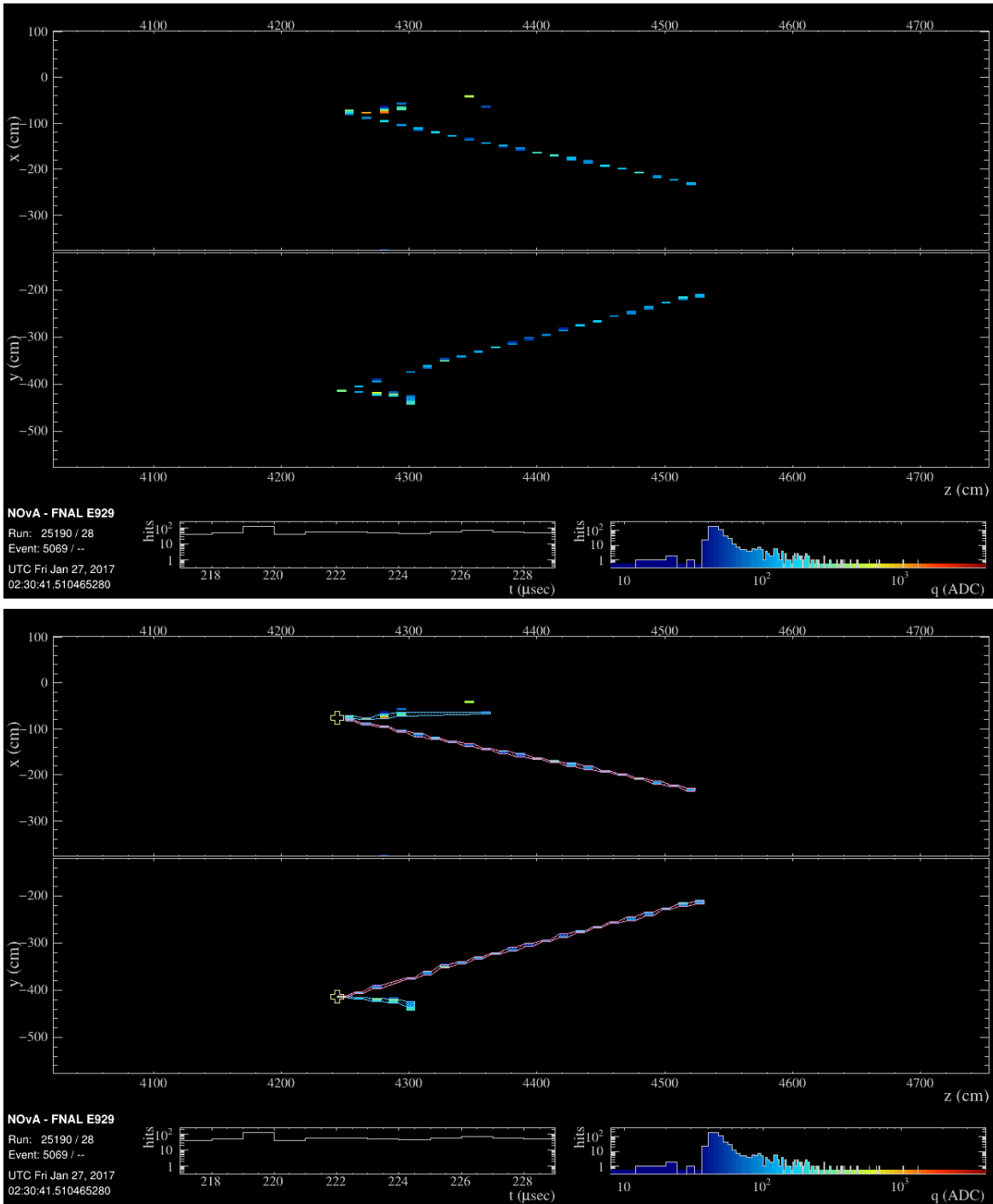


Figure 2.8: ν_μ charged current data event in the Far Detector. Bottom image has the reconstructed vertex drawn as a yellow cross, the muon hits outlined in pink, and the proton hits outlined in blue. For each image, the top half is a top-down view of the detector and the bottom half is a side view of the detector, with beam entering from the left for each. A spline fit uses the range of the muon to determine its energy, while a second spline fit based on the visible energy in the hadronic system determines the remaining energy in the event.

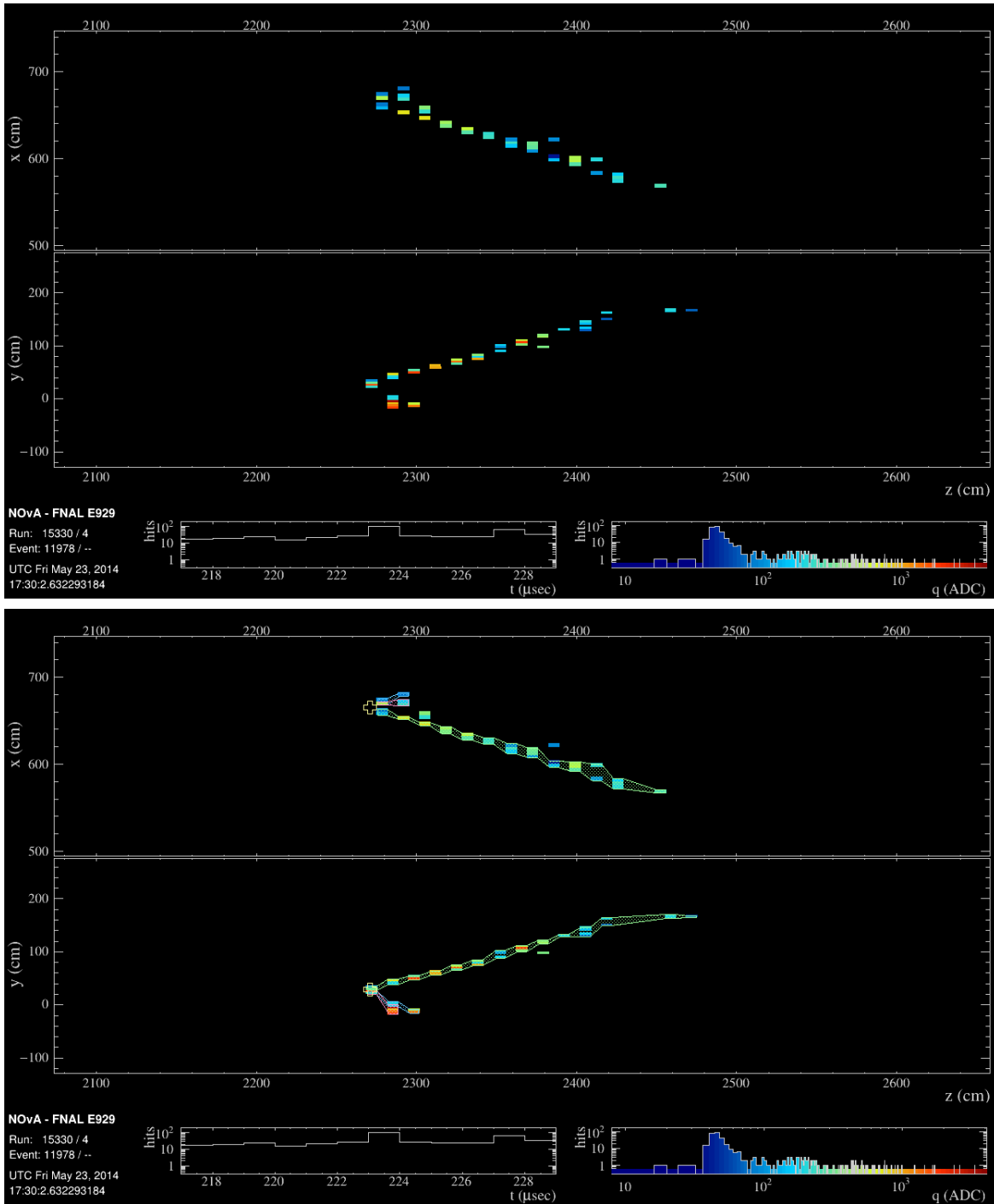


Figure 2.9: ν_e charged current data event in the Far Detector. Bottom image has the reconstructed vertex drawn as a yellow cross, the electron hits outlined in lime green, and two tracks in the hadronic system outlined in pink and blue. For each image, the top half is a top-down view of the detector and the bottom half is a side view of the detector, with beam entering from the left for each. A CNN classifies hits in the event as electromagnetic or hadronic in origin and a quadratic fit yields the energy of the neutrino.

We estimate E_ν by adding the muon energy and the calorimetric energy of the remaining hits in the cluster, attributed to the hadronic system. We split the ν_μ results into quartiles of hadronic energy resolution, with the resolution for E_{ν_μ} ranging from about 7% for the lowest resolution quartile to about 11% for the highest resolution quartile. For ν_e interactions, a CNN classifier identifies electromagnetic-like activity in the cluster and classifies hits as electromagnetic or hadronic. E_ν is determined using a quadratic fit for the electromagnetic and hadronic energies. The ν_e energy resolution is about 10%. ν_μ and ν_e energy resolution is dominated by the reconstruction of the hadronic system.

Simulation of neutrino interactions begins with generating particles in the NuMI beamline. FLUKA [56, 57] models proton interactions within the NuMI target and a Geant4 [58] simulation of the beamline transports particles through the beamline materials. The Package to Predict the FluX (PPFX) [59] corrects the flux at the NOvA Near Detector using external data from various hadron production cross section measurements and models. The GENIE event generator [60], tuned using Near Detector and external data to match current knowledge of interactions, take the neutrino flux as input to determine what neutrino interactions will occur within the detector. Cosmic ray interactions begin with the CRY event generator [61]. Once particles are generated, they are propagated through the detector material using Geant4 [58]. Custom NOvA simulation transports light created in interactions within the scintillator in each cell to the wavelength shifting fiber and down the fiber to the APD and then models the response of the detector electronics to create the equivalent of the (charge, time) hits recorded in the data.

2.4 Extrapolation and Results

Because the Near and Far Detectors have nearly identical construction, we can use the neutrino interactions recorded in the Near Detector to make a prediction of the spectra of neutrinos we see at the Far Detector. Starting with the reconstructed ν_μ energy spectrum in the Near Detector, we reweight the simulated sample in each bin of E_ν to match the data. We then extract the corresponding true E_ν spectrum from the simulation and transform this true spectrum to the spectrum we would expect at the Far Detector, accounting for expected differences between detectors based on their relative size, the precise angle of the beam at their locations, and dispersion of the beam.

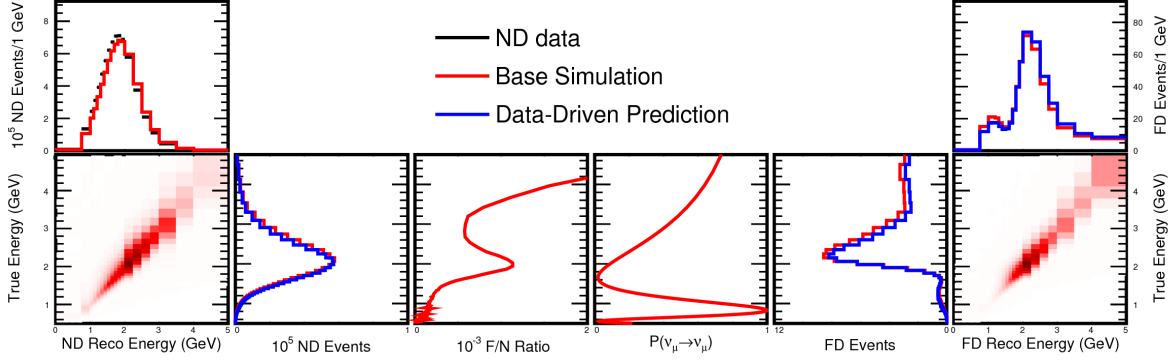


Figure 2.10: Diagram of the steps of the extrapolation procedure for predicting the ν_μ energy spectrum at the Far Detector. We start with the reconstructed energy spectrum of neutrinos in the Near Detector at the top left and after converting to true energy, accounting for differences between the two detectors, including neutrino oscillations, and converting back to reconstructed energy we end with the expected spectrum in the Far Detector at the top right.

We then account for oscillation probabilities to obtain the true E_ν spectra for ν_μ and ν_e . These true E_ν spectra are finally transformed back to reconstructed E_ν spectra so we can compare with what we are able to measure. This extrapolation procedure, diagrammed in Figure 2.10, is performed for both neutrinos and antineutrinos in bins of hadronic energy fraction (E_{had}/E_ν) and transverse momentum to remove potential bias from energy resolution and acceptance differences between the detectors. The extrapolation is performed multiple times keeping Δm_{21}^2 and $\sin^2 \theta_{12}$ fixed using external constraints, allowing $\sin^2 \theta_{13}$ to float around its external constraint, and varying Δm_{32}^2 , $\sin^2 \theta_{23}$, and δ_{CP} to find a best fit between the extrapolated simulation and measured data.

Measured neutrino energy spectra at the Far Detector are in Figure 2.11. They are overlaid on the best fit result from the extrapolation procedure with $\Delta m_{32}^2 = +2.41 \pm 0.07 \times 10^{-3} \text{ eV}^2$, $\sin^2 \theta_{23} = 0.57_{-0.04}^{+0.03}$, and $\delta_{\text{CP}} = 0.82_{-0.87}^{+0.27} \pi$. The best fit slightly favors normal mass ordering and the upper octant for θ_{23} , with significances of 1.0σ and 1.2σ , respectively. Confidence level contours for the oscillation parameters we fit for are in Figure 2.12. A comparison in the Δm_{32}^2 vs. $\sin^2 \theta_{23}$ phase space with other experiments is in Figure 2.13.

2.5 Systematic Uncertainties

With any comparison to simulation we have to account for potential mismodeling within the simulation affecting our final results. There are uncertainties associated with items like the beam flux,

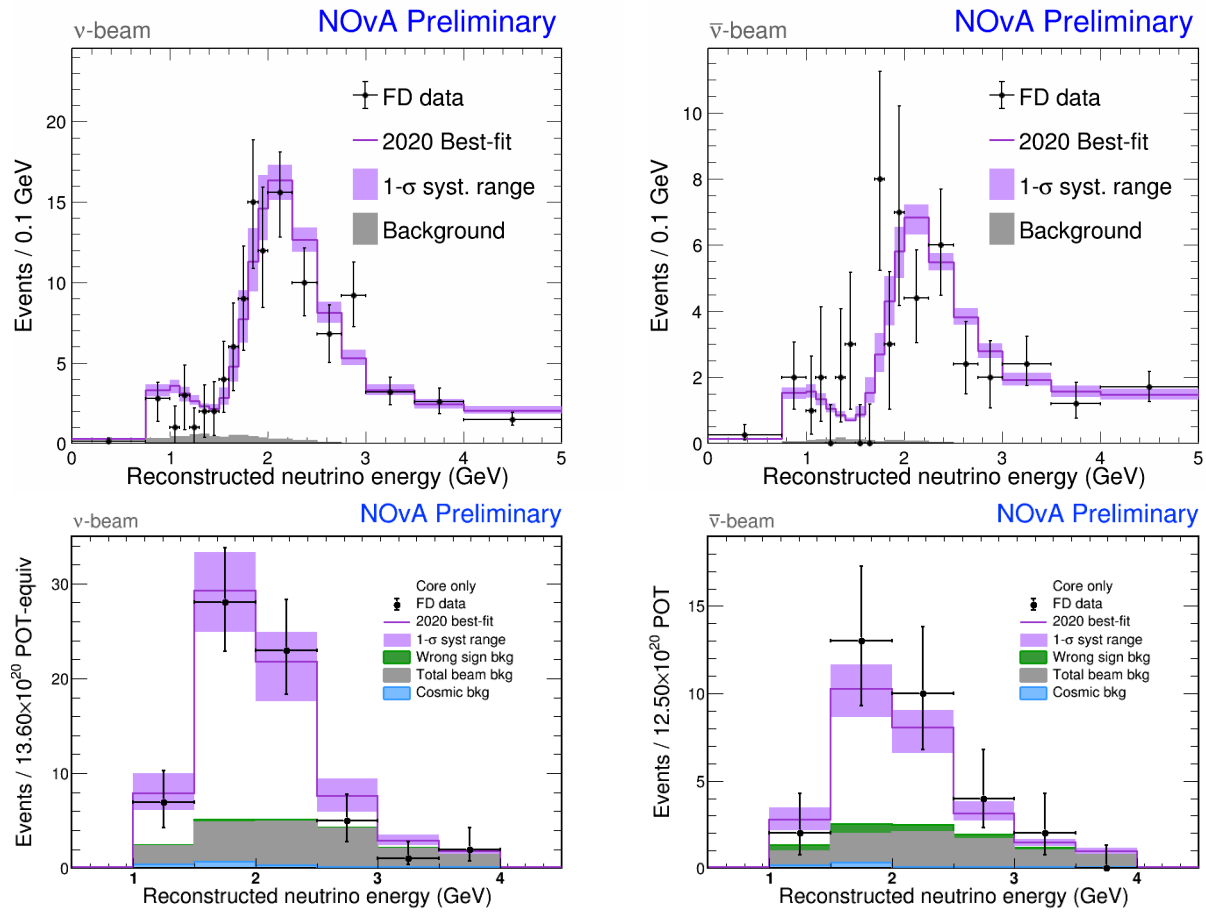


Figure 2.11: ν_μ (top) and ν_e (bottom) energy spectra at the Far Detector for neutrino (left) and antineutrino (right) data compared with extrapolated simulation best fit results. The peak in the ν_e spectra is in the same location as the dip in the ν_μ spectra, where the $\nu_\mu \rightarrow \nu_e$ oscillation probability is maximal.

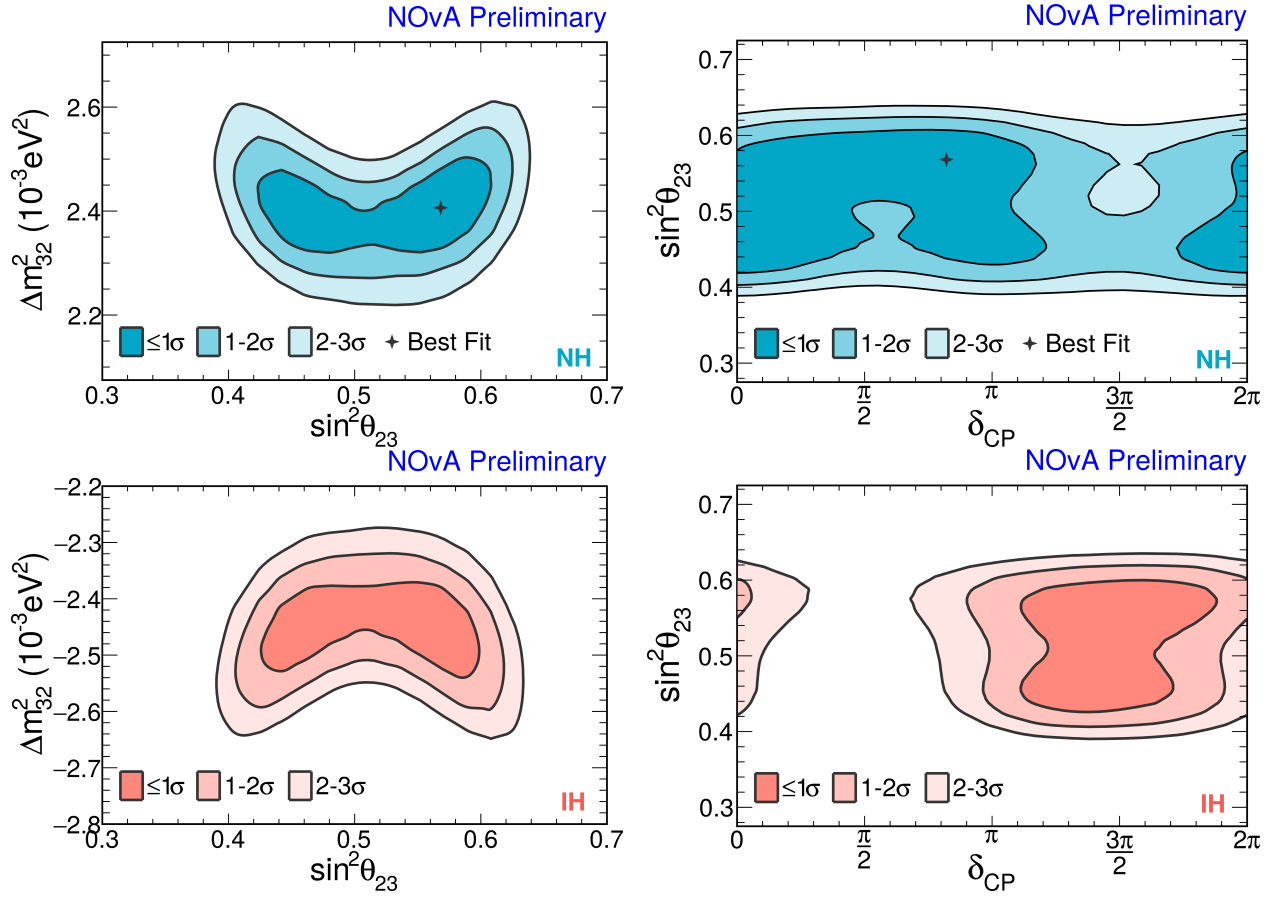


Figure 2.12: Confidence level contours in Δm_{32}^2 vs. $\sin^2 \theta_{23}$ (left) and $\sin^2 \theta_{23}$ vs. δ_{CP} (right) phase spaces for normal (top) and inverted (bottom) mass ordering. The best fit point is shown as a black cross on the normal ordering contours.

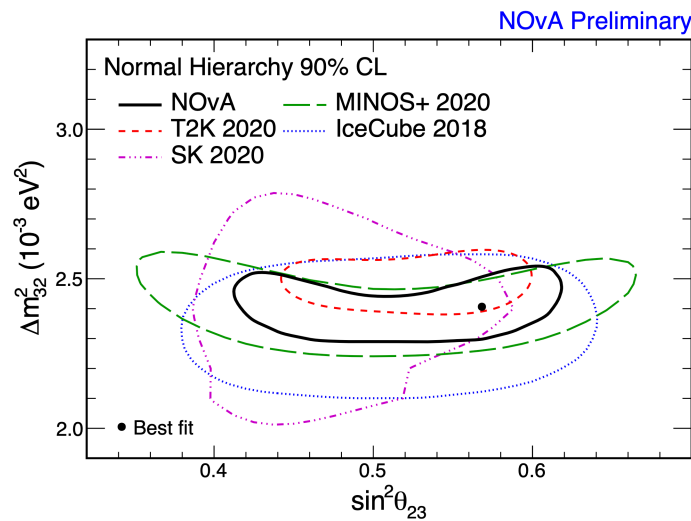


Figure 2.13: 90% confidence level contour for normal mass ordering in Δm_{32}^2 vs. $\sin^2 \theta_{23}$ phase space overlaid with results from other experiments [27, 45–47].

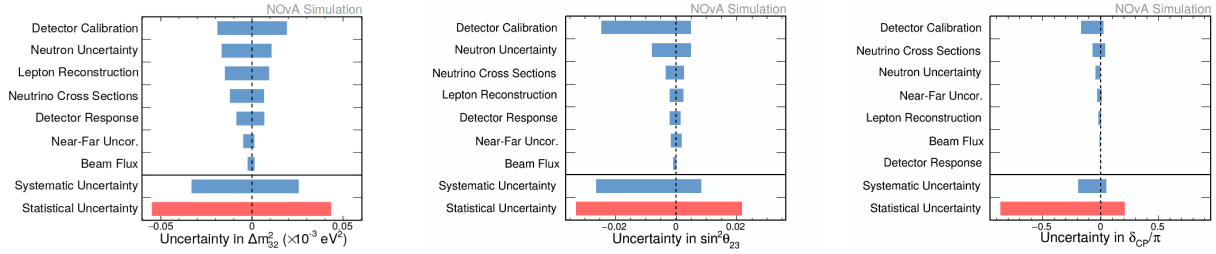


Figure 2.14: Systematic and statistical uncertainties for Δm_{32}^2 , $\sin^2 \theta_{23}$, and δ_{CP} . Detector calibration is the dominant source of systematic uncertainty for each parameter.

neutrino interactions, detector geometry and response, calibration, reconstruction, and extrapolation. Uncertainties such as detector response and calibration require recreating the simulation from the beginning with shifts applied to various parameters that could be mismodeled. Beam flux and neutrino interaction uncertainties are easier to account for as they can be found by reweighting the final prediction rather than going back to the beginning. The dominant systematic uncertainties for each oscillation parameter we calculate are in Figure 2.14. The largest uncertainty for each is detector calibration. Data to simulation comparisons of protons in the Near Detector exhibit a 5% difference in energy response, see Figure 2.15. Calibration uncertainty also arises from imperfect modeling of the energy response at the end of cells compared to in the center of the cells. Detector response uncertainties arise from aging of the scintillator lowering the average number of total hits in events over time, and the modeling of the response to light in the detector. As NOvA continues to accumulate data, the statistical errors on our measurements will continue to shrink such that they will be comparable to our systematic errors. The NOvA Test Beam program was initiated to address some of these uncertainties by assessing the detector response in an environment where more parameters of the incoming particles are known. More details about the Test Beam program are in chapter 3.

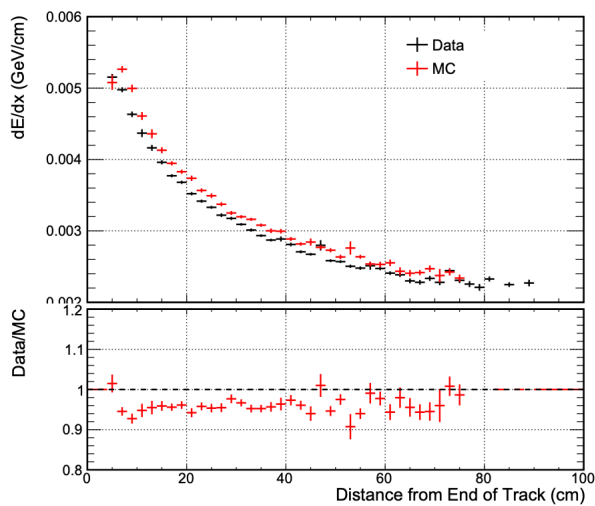


Figure 2.15: Data (black) to Monte Carlo (red) comparison of dE/dx for protons in the Near Detector as a function of the distance to the end of the proton track. The ratio between data and Monte Carlo has an average of 0.9579.

Chapter 3

NOvA Test Beam



Figure 3.1: Fish-eye photo of NOvA Test Beam experiment.

To address some of NOvA’s dominant systematic uncertainties, we placed a scaled down NOvA detector, about $\frac{1}{5}$ the size of the Near Detector, in a charged particle beamline. The beamline was outfitted with scintillator paddle time-of-flight detectors for particle identification, an analyzer magnet and wire chambers for momentum reconstruction, and a Cherenkov detector for electron discrimination. The beamline detectors provide particle identification and a momentum measurement prior to the particle entering the NOvA detector. We can compare that information with what we observe in the NOvA detector to test our calibration and reconstruction procedures and learn more about our detectors’ response to energy. Each of these components is described in more detail below.

To date, NOvA Test Beam has operated for 4 separate running periods. Period 1, our commissioning period with only half the NOvA detector active, ran from May to July 2019. Period 2, with the full detector, ran from December 2019 to March 2020, and period 3 ran from January 2021 to June 2021. In period 2 we collected about 5400 particles with a variety of trigger and beam conditions. Additional beam tuning was done during the beginning of period 3. That, along with the longer running time, resulted in an additional 27000 particles collected in period 3 at three different momentum settings. The fourth and final period began in November 2021.

3.1 Beam

The beam at Fermilab [62] starts out with a 35 keV H^- ion source, with 100 μ s long pulses at a rate of 15 Hz. The beam is chopped using an Einzel Lens to select a portion of each pulse to send into a Radio Frequency Quadrupole (RFQ) for acceleration. The RFQ focuses the beam using an electric field and accelerates the ions to 750 keV. Additional focusing is done by a pair of magnetic quadrupole doublets and an RF buncher cavity prior to beam entering the linear accelerator (Linac). The Linac accelerates the ions to 400 MeV through drift tubes and RF stations. Following the Linac, the beam is directed into the Booster ring through another beam chopper that selects pulses the length of the Booster circumference (474.2 m, 1.6 μ s) and through a stripping foil to remove the electrons, resulting in a beam of protons. Through a system of RF cavities, the protons are accelerated to 8 GeV. From the Booster, protons are sent down the MI-8 line to the Recycler. In the Recycler, the bunches of the beam are merged together to form six double-intensity batches, through a process called slip-stacking, which are then extracted to the Main Injector, where the protons are accelerated to 120 GeV using electromagnets.

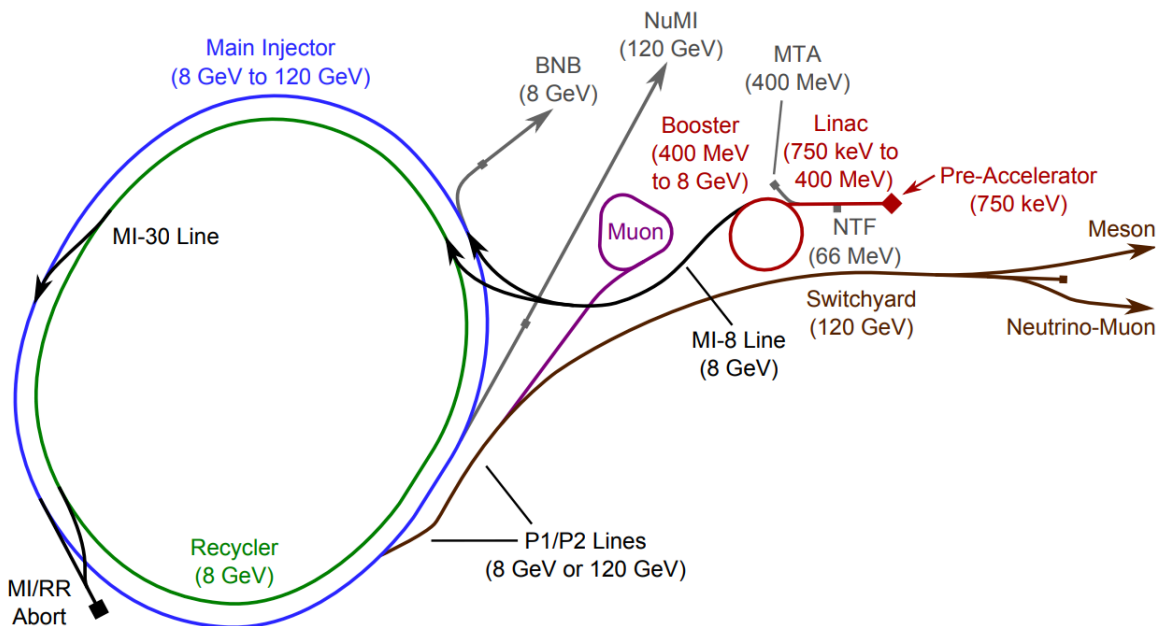


Figure 3.2: From [62], diagram of the accelerator complex at Fermilab. For Test Beam experiments, beam begins at the pre-accelerator on the upper right of the diagram and continues through the Linac, Booster, Main Injector, and Recycler, and is then extracted to the Switchyard line on the right hand side of the diagram. NOvA Test Beam is located on the Meson line of Switchyard.

These protons can be sent down the Neutrinos at the Main Injector (NuMI) beamline towards the NOvA Near Detector, but for Test Beam experiments, a resonant extraction resulting in a long, low-intensity pulse sends the beam to Switchyard. The extraction spreads out the 11 μs pulse we receive in the NuMI beamline to the same amount of intensity in a 4.2 s pulse. Upon reaching Switchyard, the beam is split by electrostatic splitting septa to send beam to the Switchyard beam absorber or down the M(eson)Test or MCenter beamlines. NOvA Test Beam is located in the MC7b enclosure, and uses the MCenter beamline. The beam spill consists of 1.6 μs length pulses of beam, or “buckets”, spaced 11.2 μs apart, with a total spill length of 4.2 s. The buckets are not all equally filled since the resonant extraction is somewhat chaotic. The intensity of the spill ramps up for the first half second, it is at its highest for the next second, and then slowly ramps down for the remainder of the spill. An example of the spill structure made by integrating hits in the detector over multiple low intensity spills is in Figure 3.3. At higher beam intensity, the majority of the extra intensity is added to the beginning of the spill.

Once in the MCenter beamline, the protons impinge on a copper target. The resulting beam is tuned to select 64 GeV particles, of which about 90% are protons, 10% pions [63]. We performed some secondary beam momentum scans, and ran with a momentum of 64 GeV/ c for the majority of data-taking. We also ran with various secondary collimator openings to try to maximize recorded beam triggers while minimizing the effect of high particle rates shutting off the detector electronics (see section 3.4 and chapter 4 for more details), though the majority of our period 2 data was taken at a single setting, with an average opening of 12.69 mm.

Upon entering the MC7b enclosure, the beam hits another copper target, which marks the beginning of the tertiary beamline. The tertiary beamline consists of a dipole magnet to select particles of momenta 0.2-2.0 GeV/ c and a suite of detectors for identifying particles by type and momenta prior to them entering the NOvA detector, placed 14.62 m downstream of the target.

3.2 Tertiary Beamline Components

3.2.1 Time of Flight System

We had a total of 3 time-of-flight (TOF) detectors, two scintillator paddles read out by photomultiplier tubes (PMTs) and a third read out by silicon photomultipliers (SiPMs). The SiPM TOF was not

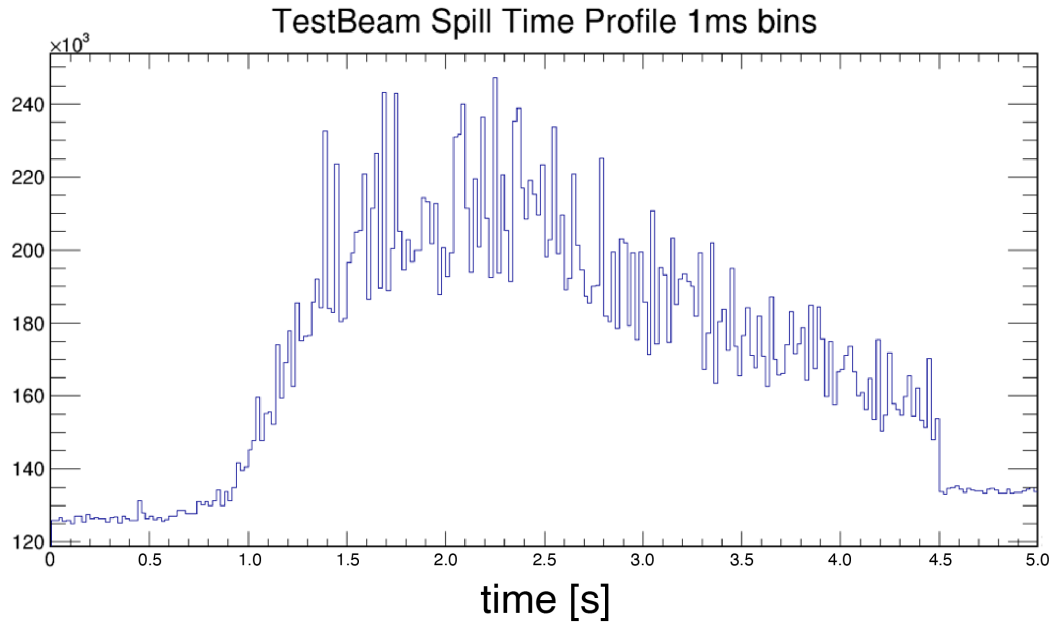


Figure 3.3: Spill structure found by counting up hits on a single pixel in the NOvA detector and integrating over multiple spills. Data collected with low intensity beam (1×10^8 ppp) to reduce electronics shutoffs. The unevenness of the spill is due to the chaotic nature of the resonant extraction. Some buckets will be empty while others will be overfilled.

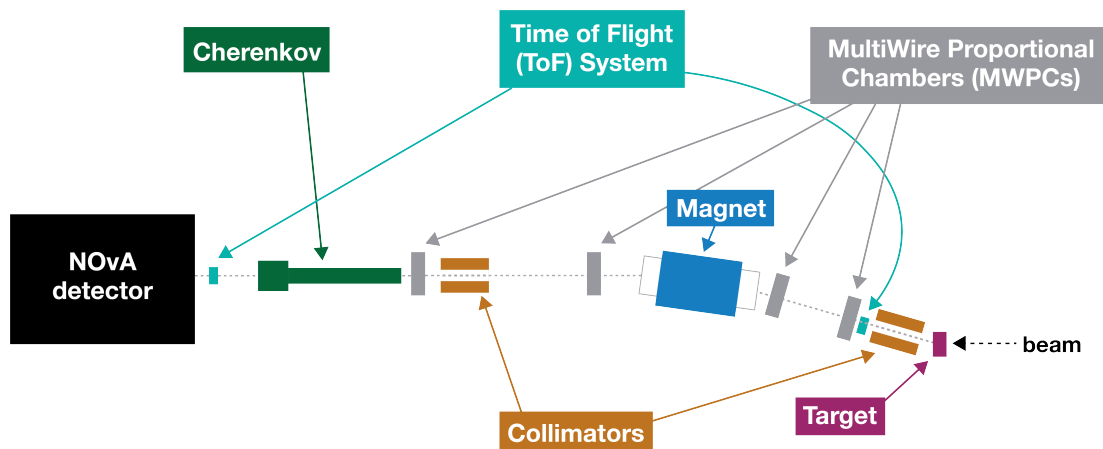


Figure 3.4: Diagram of beamline components. Scintillator paddles and helium pipes not shown. The distance from the target to the NOvA detector is 14.62 m.

NOvA Preliminary

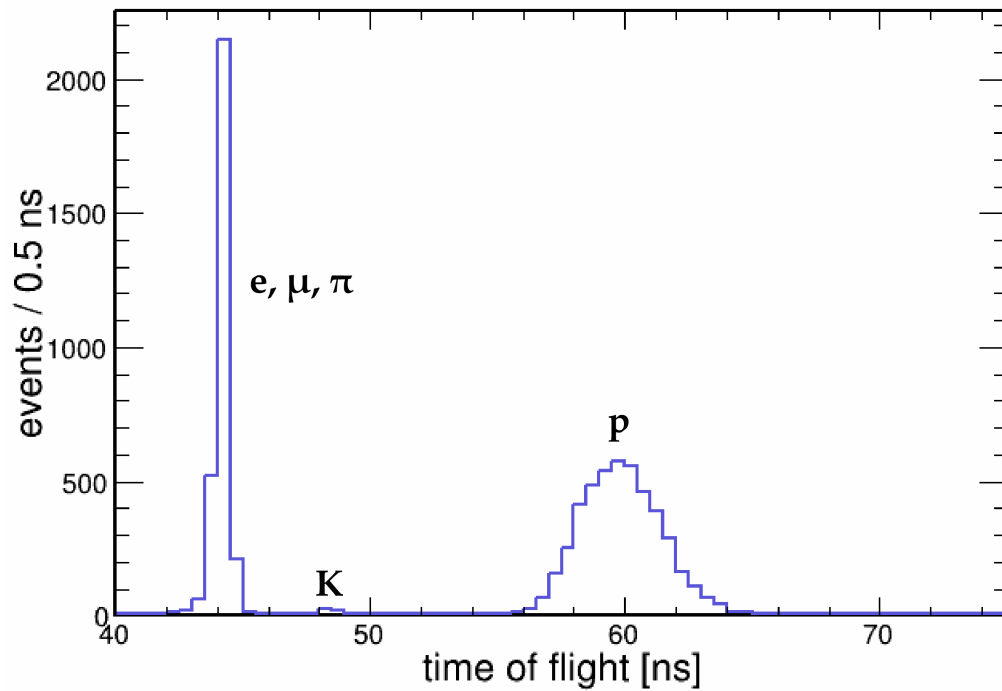


Figure 3.5: Time of flight for 1 GeV/ c particles in period 2. The time of flight detectors are separated by 13.16 m. They provide good separation between protons, kaons, and the peak of faster particles, but do not provide separation between electrons, muons, and pions.

read out during period 2, and therefore is not used in this analysis. The PMT TOFs are $5.91 \times 5.91 \text{ in}^2$. The upstream one, placed immediately after the target collimator, is 0.79 in thick, and the downstream one, placed after the Cherenkov detector, is 0.24 in thick. The path length through the beamline from the upstream TOF to the downstream one, assuming two straight lines, is 13.16 m. Although the TOF detectors provide ns timing resolution, at 1 GeV/ c there is no separation between electrons, muon, and pions. Kaons are separated from the faster particles by $> 3\sigma$ and protons are an additional 6σ higher. Time of flight values for 1 GeV/ c particles recorded in period 2 are in Figure 3.5. For period 3, the PMT TOF detectors were redeployed, with the thinner one placed after the target collimator and the thicker one placed 1 m downstream of wire chamber 4, prior to the Cherenkov detector, to increase the acceptance of particles.

3.2.2 Multi-Wire Proportional Chambers and Magnet - momentum reconstruction

To determine the momentum of each particle passing through the beamline we use a system of four Multi-Wire Proportional Chambers (MWPCs or WCs) with a bending dipole magnet in between wire chamber 2 and 3. Each MWPC has a horizontal and vertical plane, consisting of 128 gold plated tungsten wires spaced 1 mm apart. The chambers are filled with a gas mixture that is 85% argon and 15% isobutane. The wire chambers operated between 2420 and 2490 V in period 2. Every time the beamline triggers, the wire chambers read out 1207 ns of hits on the wires as (wire number, TDC) pairs.

A dipole magnet sits between MWPC 2 and 3 at an 8° angle to the z-axis, along the beamline. Using hit positions in the WCs and a parameterization of the magnetic field, we can calculate a particle's momentum. We derived the parameterization using field maps of the magnet for magnet currents of 300, 1200, and 2100 A. Field maps for 5 other magnet currents between 300 and 2100 A were created by interpolating from the existing maps using a quadratic of the form $B = a + bI + cI^2$, where B is the magnetic field at each point, I is the magnet current, and a , b , and c were found by fitting the existing maps. Using the length of the magnet as the effective length of the field, L_{eff} , and integrating along the z-axis of the magnet provides the effective field, B_{eff} , for each magnet current.

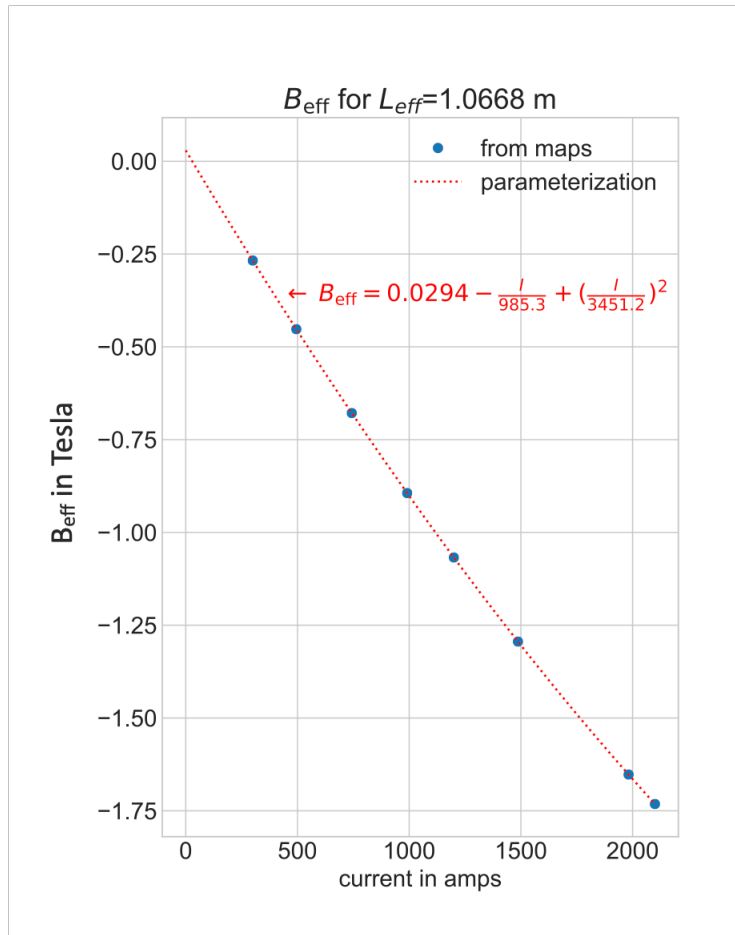


Figure 3.6: From [64], effective magnetic field as a function of magnet current. Points are the values obtained from using the full field maps and the red curve is the parameterization. Field maps for 300, 1200, and 2100 A were measured, the others were interpolated from the measured maps.

The resulting parameterization, also shown in Figure 3.6, is

$$B_{\text{eff}} = 0.0294 - \frac{I}{985.3} + \left(\frac{I}{3451.2} \right)^2. \quad (3.1)$$

Hit clusters are formed on each plane of each WC using a DBSCAN algorithm[65]. Clusters with more than 10 hits are rejected as noise. The earliest hit in each cluster is used for the position measurement in that plane of the WC. Creation of a track requires hits on all 8 planes. Tracks are fit to the hit clusters assuming the straightest line possible in the YZ plane, since the magnet will not bend the particle in that plane. The angles the tracks form with the magnet are then used along with the effective magnetic field to determine the particle's momentum with

$$p = \frac{0.99 \times B_{\text{eff}} L_{\text{eff}}}{3.33564 (\sin(\theta_{\text{DS}} + \theta_{\text{mag}}) - \sin(\theta_{\text{US}} + \theta_{\text{mag}})) \cos(\arctan(\frac{dy}{dz}))} \quad (3.2)$$

where p is the momentum of the particle, B_{eff} is the effective magnetic field, L_{eff} is the effective length of the magnetic field = 106.68 cm, $\theta_{\{\text{US,DS}\}}$ are the angles the upstream and downstream tracks form with the magnet, $\theta_{\text{mag}} = 8^\circ$, and $\frac{dy}{dz}$ is the slope the tracks make in the YZ plane. The factor of 0.99 is added so the TOF vs. WC momentum curve matches with theory, see Figure 3.7. Early momentum resolution studies show the resolution is about 5%.

3.2.3 Cherenkov Detector

To further discriminate electrons from other particles, we placed a Cherenkov detector close to the end of the tertiary beamline. For period 2, the Cherenkov was placed just upstream of the two downstream TOF detectors. Filled with CO₂ at 1 atm, the detector yields Cherenkov light for electrons down to 20 MeV. Each end of the pipe has two windows: a 0.006 in vinyl window followed by a 0.00175 in tedlar window. Inside the gas volume there is 0.001 in thick mylar mirror at a 45° angle to the XZ plane to direct the Cherenkov light down to a PMT.

3.2.4 Scintillator Paddles

We have 4 scintillator paddles placed in the beamline just upstream of each wire chamber. We found that triggering on a coincidence of these paddles provided more efficient triggers than triggering on

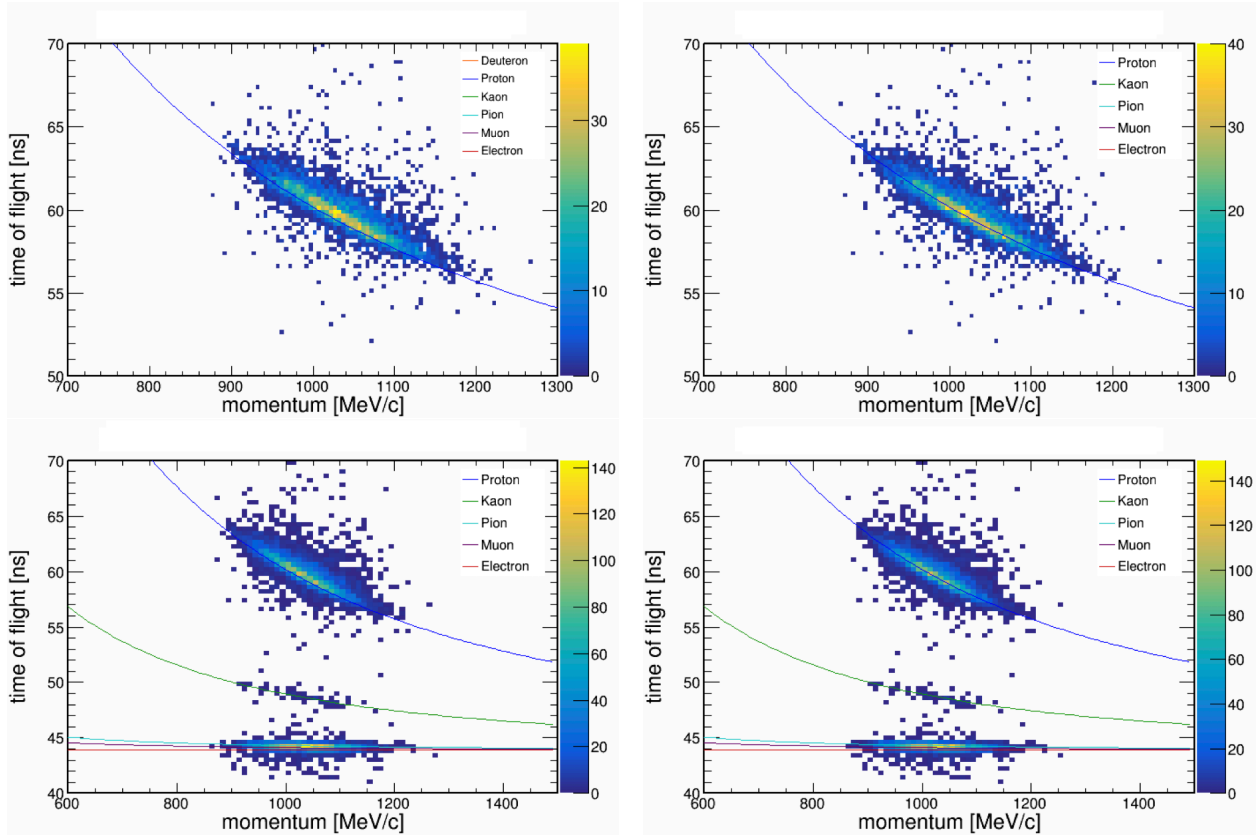


Figure 3.7: Time of flight versus momentum for 1 GeV/c protons (top) and all 1 GeV/c particles (bottom). The plots on the right have a 1% downward shift in momentum applied. The time of flight for a speed of light particle passing through the beamline is 43.9 ns.

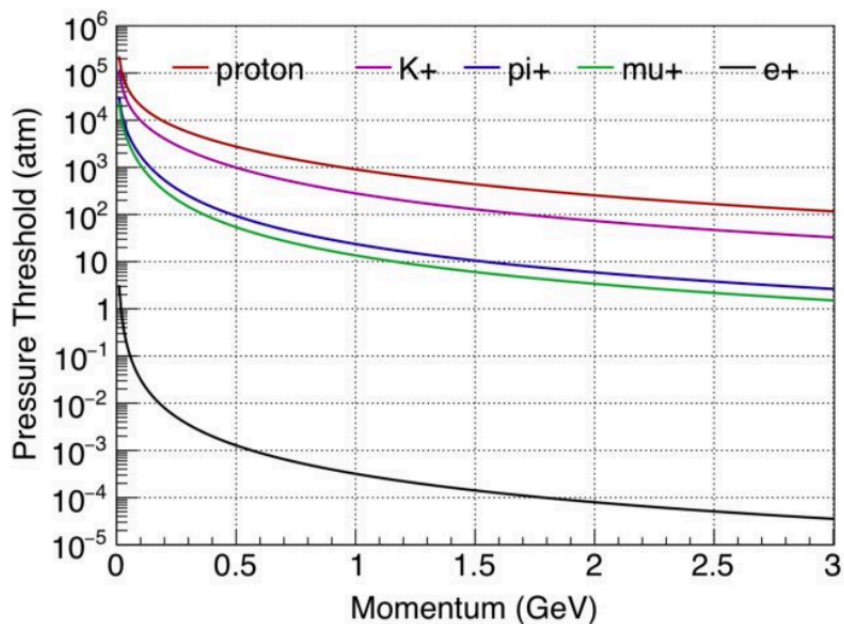


Figure 3.8: Pressure threshold for Cherenkov radiation in CO₂. NOvA Test Beam used CO₂ at 1 atm. At this pressure electrons with momentum down to 20 MeV/*c* will emit Cherenkov radiation while muons, pions, kaons and protons will not.

a coincidence of the wire chambers. The majority of data-taking was done with a 4-of-4 scintillator paddle trigger.

3.2.5 Helium pipes

For period 2 we had 4 helium pipes in the beamline to minimize interactions and energy loss as particles traverse the beamline. These were placed between WCs 1 and 2, between the magnet and WC 3, between WCs 3 and 4, and between WC 4 and the Cherenkov detector. In period 3 the last helium pipe was removed to make room for the downstream TOF detector.

3.3 NOvA Test Beam Detector

The NOvA Test Beam Detector, pictured in Figure 3.9, is a scaled down version of the Near and Far Detectors. It consists of two 31 plane blocks, starting and ending with vertical planes, with an extra horizontal plane glued in between the two blocks. The detector is 64 cells wide \times 64 cells tall \times 63 planes deep. It measures 2.6 m \times 2.6 m \times 4.2 m. The detector is outfitted with 126 front end boards (FEBs). 118 of the FEBs are v4 FEBs, like the ones we have on the Far Detector. The remaining 8



Figure 3.9: Picture of the NOvA Test Beam detector in the MC7b enclosure at the Fermilab Test Beam Facility. The silver tube to the right (upstream) of the detector is the Cherenkov detector.

are the faster v5 FEBs used on the Near Detector. The v5 FEBs are located in the middle 2 planes of each block, planes 16, 17, 48, and 49. We used a mix of FEB types to study the differences in their response in the same environment.

3.3.1 Triggers

For Test Beam, we have three beam-based triggers, one pulsed trigger, and two data-driven triggers. The first beam-based trigger is a 1 Hz pulsed trigger from Fermilab's Accelerator Division. This ensures our connection to the beam signal is intact. We also record 5 s approximately centered on the 4.2 s beam spill based on a start spill signal, referred to as the Spill trigger. The final beam-based trigger, the Beamline trigger, is the one we use primarily for analysis. When the trigger conditions for the beamline are met (more details in section 3.4), the trigger board sends a signal to the beamline Timing Distribution Unit (TDU), which in turn sends a signal to the detector TDU. The signal passes through a secondary input and tells the detector to read out. For each Beamline trigger we record 150 μ s of data. The data-driven triggers are both activity-based triggers. The first is intended to record cosmic ray induced events for use in calibrating the detector. The second has additional requirements about the location of the tracks, requiring that they enter the front face along the

central axis of the detector. This was created to pick up beamline particles in case the Beamline trigger failed.

3.3.2 Detector Geometry

In March 2019 the Fermilab survey and alignment group ensured our beamline detectors were aligned and took precise measurements of their locations, along with measurements along the NOvA detector planes. For most of the vertical (even-numbered) detector planes, we had 5 data points, located as illustrated in Figure 3.10. Most horizontal (odd-numbered) planes had 10 data points, illustrated in Figure 3.11. I used this data to determine the relative position and roll of each plane.

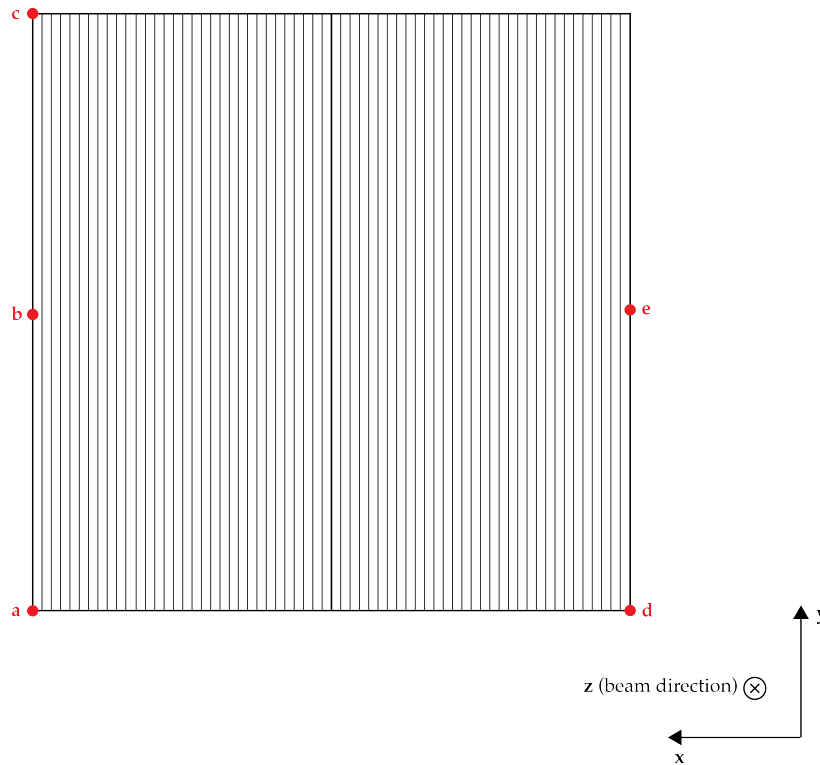


Figure 3.10: Vertical plane with locations of survey points. Plane 6 was missing point *a*.

For vertical planes,

- I used the x location of all 5 points to find the horizontal center.

$$x = \text{avg}(\text{avg}(a_x, b_x, c_x), \text{avg}(d_x, e_x))$$

- Since points b and e are located semi-randomly in y , usually located either side of the module boundary but with no clear patter, I only used 3 points for the vertical center.

$$y = \text{avg}(\text{avg}(a_y, d_y), c_y)$$

- The z coordinate of each plane is not needed, since all planes are the same depth, but I calculated it for a sanity check. For each plane, points a - c were measured on the front face, while d and e were measured on the back.

$$z = \text{avg}(\text{avg}(a_z, b_z, c_z), \text{avg}(d_z, e_z))$$

- I used the line from a to c to find the roll of the plane.

$$\text{roll (around } z) = \arctan(\text{slope}(a \rightarrow c))$$

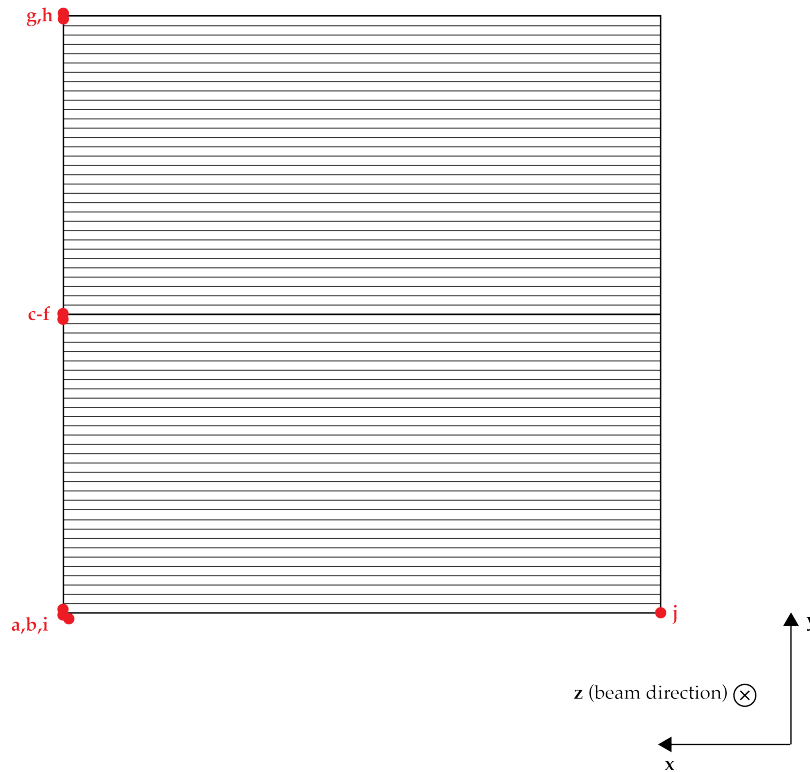


Figure 3.11: Horizontal plane with locations of survey points.

For horizontal planes,

- I used the x location of all 10 points to find the horizontal center.

$$x = \text{avg}(\text{avg}(a_x - i_x), \text{avg}(j_x))$$

- Points a and b are opposite g and h , while i and j were measured from the bottom. Points i and j were dropped from the y location calculation.

$$y = \text{avg}(a-h)$$

- Again, the z coordinate is not needed, but calculated as a sanity check. For each plane, points a , c , e , and g were measured on the front face, while b , d , f , and g were measured on the back. Points i and j were measured around the middle of the plane, but were somewhat randomly distributed so I dropped them from this calculation.

$$z = \text{avg}(a-h)$$

- I used the line from a and b to g and h to find the roll of the plane.

$$\text{roll (around } z) = \arctan(\text{slope}(a, b \rightarrow g, h))$$

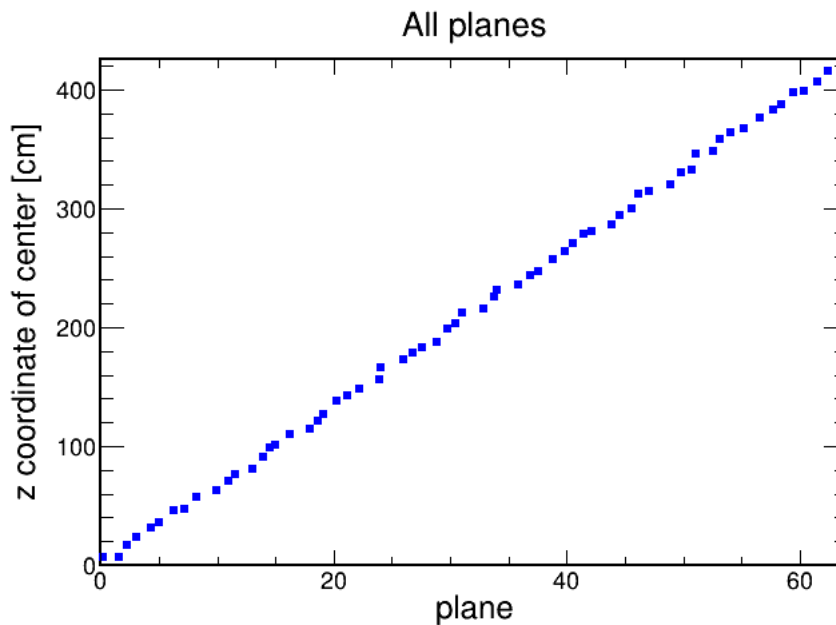


Figure 3.12: **z (depth in beam direction) location of each plane.** The front face of the detector is at $z = 0$. Plane centers are an average of 6.68 cm apart. The variation along this line is due to variation in where the measurements were taken, not in plane depth.

The relative position of each plane in x , y , and z is shown in Figure 3.13, Figure 3.14, and Figure 3.12. The roll around the beam axis is in Figure 3.15. The x (horizontal) coordinate for vertical planes is known to within a few millimeters. For the horizontal planes, although the 1.5 cm shift in x between blocks is evident, the precise locations within the block move around by about 0.5 cm. These locations could shift that much in reality, or the calculated value could be affected by only having one measurement on the east ($-x$) side of the detector compared to the ten measurements on the west ($+x$) side. The y (vertical) coordinate for vertical planes moves around by about 1 cm. This calculation suffers from a similar problem as the x coordinate on horizontal planes: there is only one measurement on the top ($+y$) edge of each plane and two measurements on the bottom ($-y$)

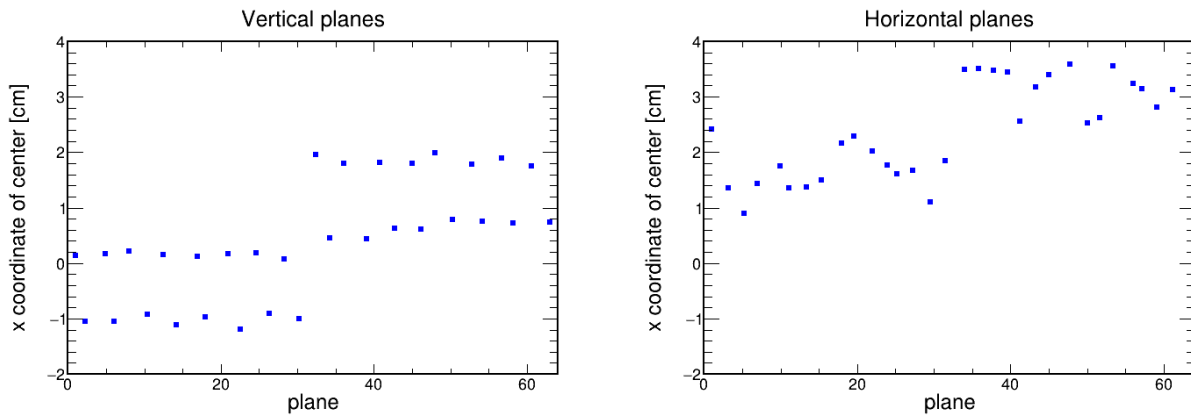


Figure 3.13: **x (horizontal) location of each plane.** Vertical planes show the expected stagger. This is done so that if a particle passes through the plastic between cells in one plane, it will enter the cell in the next vertical plane. The stagger between planes is about 1 cm, with a shift of 1.5 cm between blocks. Horizontal planes also shift about 1.5 cm between blocks.

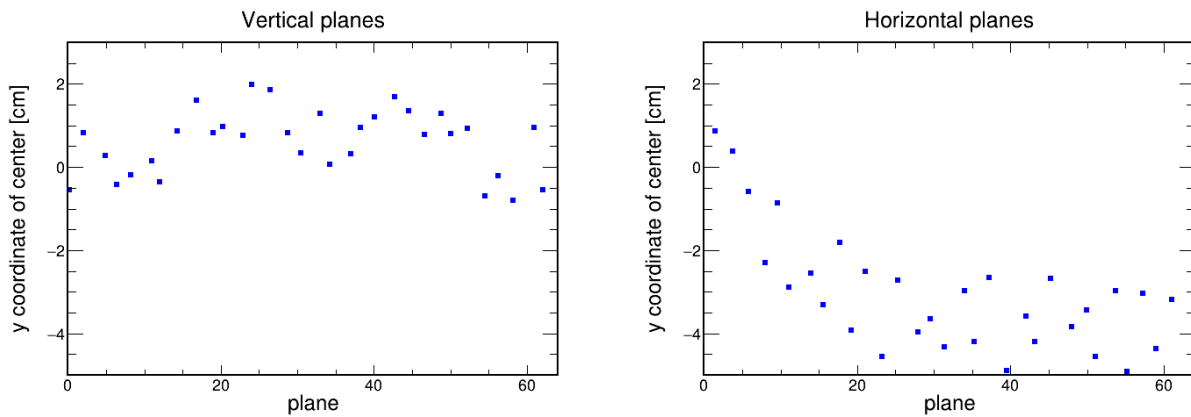


Figure 3.14: **y (vertical) location of each plane.** The horizontal planes are staggered in their vertical position, but not as precisely as the horizontal stagger. There is no obvious shift between blocks in the vertical position.

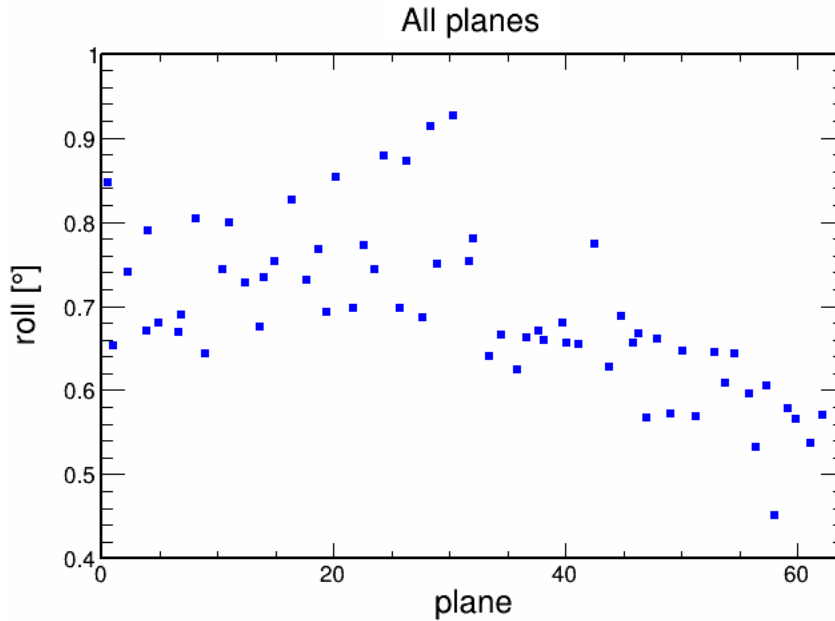


Figure 3.15: **Roll (around beam direction) of each plane.** Unfortunately, the direction of the roll means the east side of the detector is slightly lower than the west side. The east side is where the readout and fill ports for the scintillator are. As a result, the top cell in each horizontal module is underfilled, with an air bubble on the west side.

edge. For horizontal planes, the stagger in y from plane to plane is evident, but the amount of stagger is not constant. The horizontal planes do not sit on the detector support like the vertical planes, so placing them with a well-defined stagger in y is more difficult. The z (depth into detector) coordinate varies mostly due to where in z the measurements were taken. The placement and rotation of the NOvA detector relative to the beamline detectors was more difficult to determine. The geometry file has a single location for the center of the detector, and determining where the center is based on survey points taken around the outside is not a simple task. I used a data-driven method to determine the placement instead. I compared the starting point of tracks in the detector to where the track from the wire chambers (WCs) intersects the front face of the detector. Distributions of the X and Y location of tracks at the front face of the detector after tuning are in Figure 3.16. Detector cells are 4 cm wide, so there is an unavoidable discrepancy due to the granularity of the detector. To determine the pitch and yaw of the detector, I compared the direction of track in the detector to the WC track direction for tracks with a z direction cosine > 0.99 , distributions shown in Figure 3.17. Very forward going tracks were selected to remove protons that inelastically scattered in the detector. The pitch and yaw of the detector was 2.464° around x and 0.487° around z . Following all of the

alignment, we know the relative location of planes within the detector to about 1 cm in x and y. The placement of the detector relative to the beamline has a larger uncertainty of about 4 cm and the rotation uncertainty is about 20 mrad.

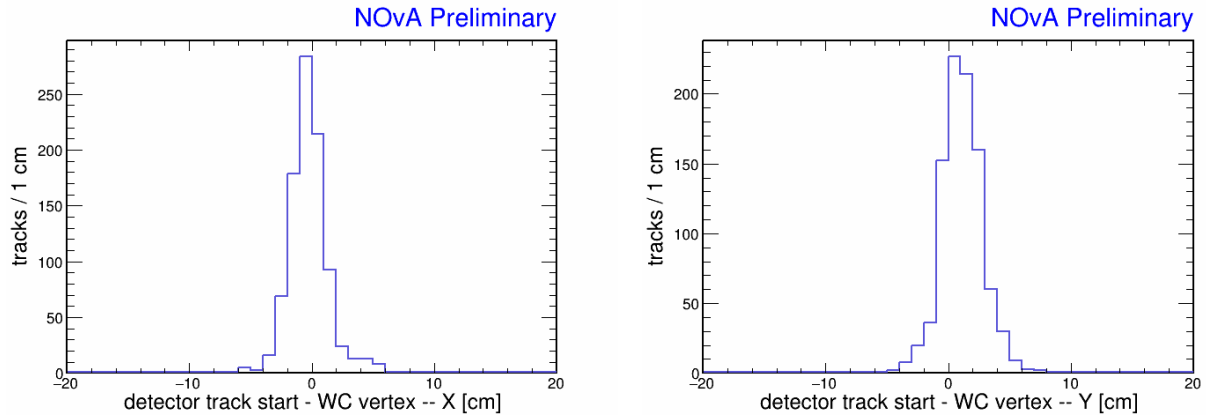


Figure 3.16: Difference between start location of track in NOvA detector and wire chamber (WC) track projected forwards to the front face of the NOvA detector after tuning the placement of the detector.

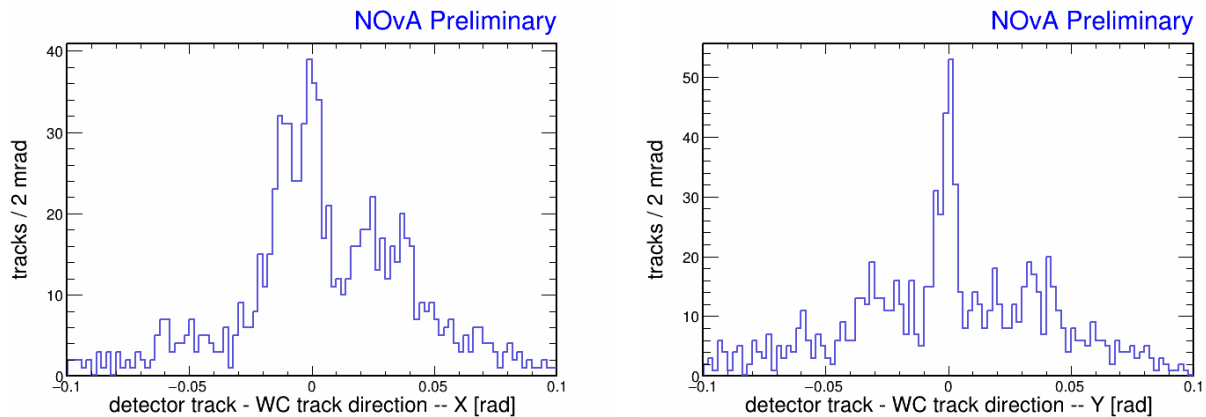


Figure 3.17: Difference between direction of track in NOvA detector and direction of wire chamber (WC) track after tuning the rotation (pitch and yaw) of the detector. Plot made using tracks with a z direction > 0.99 to remove any protons that may have inelastically scattered, thus changing their direction. Due to the granularity of the NOvA detector, some directions are favored over others based on the geometry of the cells. The rotation of the detector was chosen so that the peak in these distributions is at 0.

3.3.3 Detector Calibration

The energy scale of the detector depends on the response of the fiber, scintillator, and electronics. We use cosmic ray muons to calibrate these responses. Fiber attenuation characteristics can reduce

how much light is detected by 10-20% as a function of how far away from the readout the light is deposited. The effect is not identical for each cell, so we fit attenuation curves for each cell. We select “through-going muons”, muons that pass all the way through the detector, to measure the relative response of each cell. After reconstructing a track through the detector for each muon, we step through each cell in the track to measure the number of photoelectrons per centimeter (pe/cm), using location information from adjacent planes to determine dx and provide an estimate of how far along the cell the energy was deposited. Example attenuation curves for two different cells in the Test Beam Detector are in Figure 3.19. Once the relative differences between cells are accounted for, we compare pe/cm of muons that stop in the detector to GeV/cm values from simulated muon tracks to determine the absolute energy scale of the detector. The resulting energy scale shown as energy per centimeter as a function of distance to the end of the muon track is in Figure 3.18.

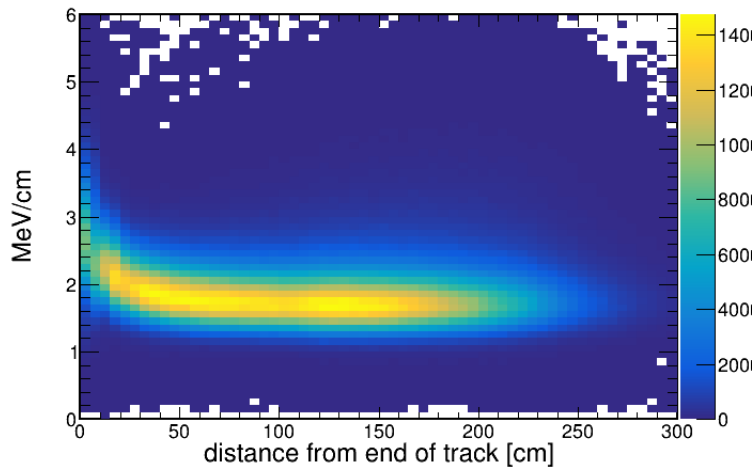


Figure 3.18: MeV/cm vs. distance from the end of the muon track for stopping muons in Test Beam data. Muons deposit just under 2 MeV/cm in the detector in the minimally ionizing portion of their track.

Along with setting the energy scale of the detector, we need to calibrate the timing of the readout system for the detector. The Data Concentrator Modules (DCMs) responsible for collating the data from multiple FEBs get their timing information via a daisy chain originating at the detector TDU. Each DCM in the chain has a timing offset relative to the DCM before it, with the last DCM having the earliest time. Following the procedure described in [66], I used timing information from hits on cosmic ray muon tracks that pass through multiple DCMs to determine the relative offsets between DCMs, shown in Figure 3.20. The offset between DCMs 1 and 2 is comparable to a typical offset

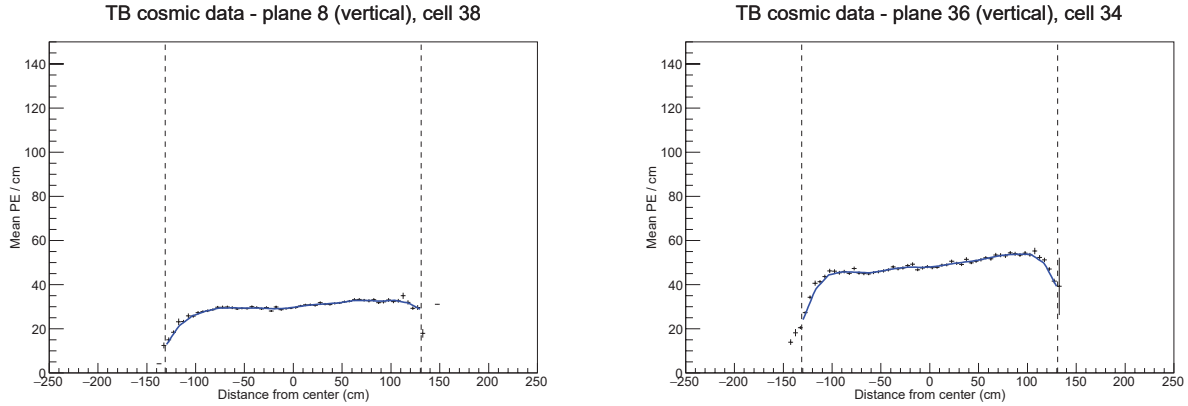


Figure 3.19: Photoelectrons/cm as a function of distance along the cell for cosmic ray muon hits in the Test Beam Detector in two different cells. Data points are in black and the attenuation fits are the blue lines. The dashed lines show where the edges of the detector are.

at the Far Detector. The offset for DCM 3 is larger, but this DCM has the FEBs with faster timing on it so a direct comparison cannot be made. The timing resolution for the Test Beam Detector is comparable to that of the Far Detector (Figure 3.21).

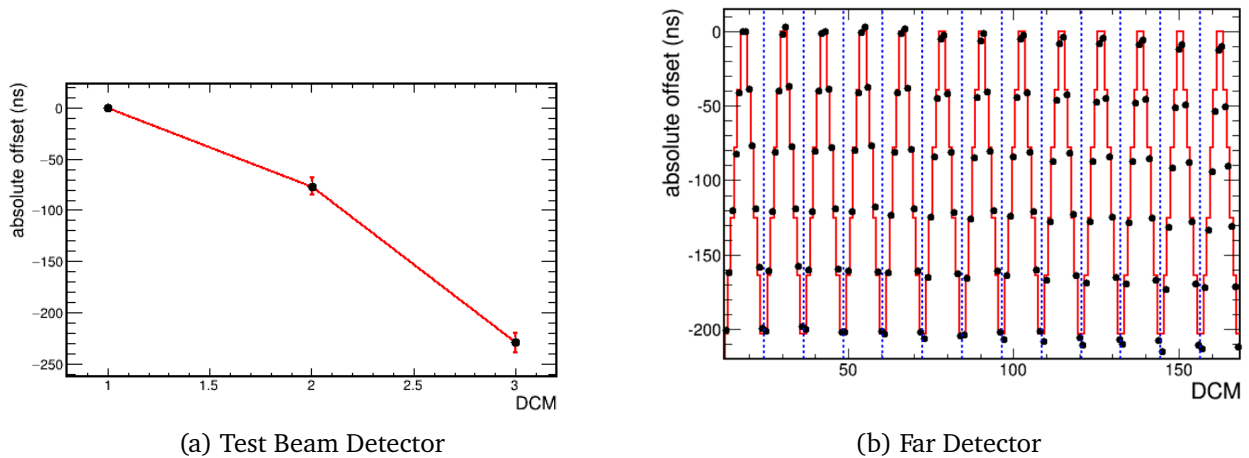


Figure 3.20: DCM timing offsets for Test Beam Detector (left) and Far Detector (right). The Far Detector has 28 timing chains, with 6 DCMs each. Offsets between DCMs at the Far Detector are comparable to the offset between DCMs 1 and 2 on the Test Beam Detector. DCM 3 has faster electronics, so the offset cannot be directly compared.

3.4 Test Beam Installation, Commissioning, and Data-Taking Summary

During the spring of 2018 I began working with our data acquisition (DAQ) code, making sure it would work with a new detector. A few parts of the code were written with enough forward-thinking

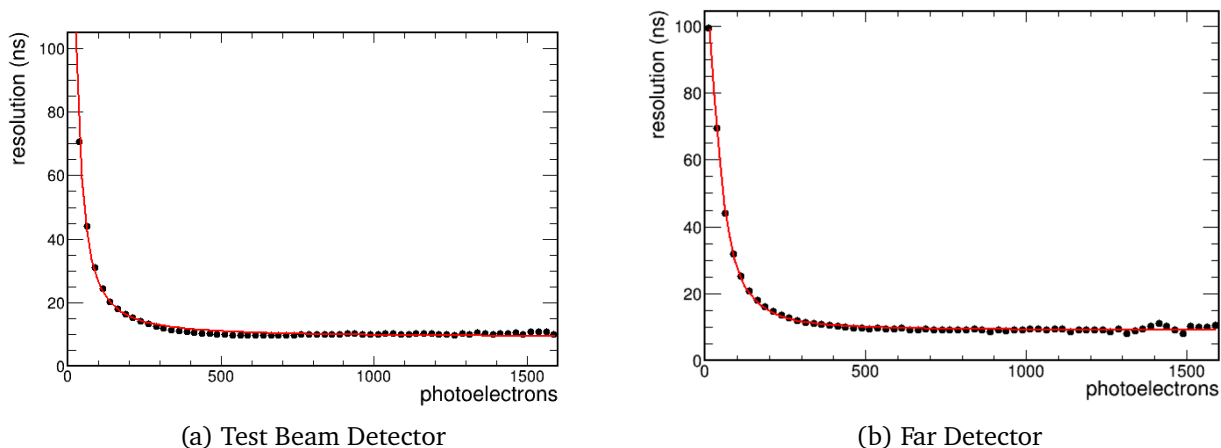


Figure 3.21: Timing resolution vs. pulse height of Test Beam Detector (left) and Far Detector (right). The timing resolution of the two detectors is similar.

to include the Test Beam Detector from the beginning, but much of it needed small adaptations. Prior to the detector being fully put together, we had a handful of FEBs hooked up to a test stand to ensure the DAQ was working. Following that work, I began adapting our offline simulation and analysis code to work with the Test Beam Detector as well. Some of this work was complicated by the fact that the detector is rotated 180° around the y-axis compared to the Near and Far Detectors, meaning the readout end of our horizontal modules is on the opposite side of the detector, and the vertical modules are flipped relative to the other detectors, so some assumptions built into the code needed adjusting.

In April 2019 we began to fill the detector with scintillator. Following the filling of the first block (of two), we had to transfer more scintillator from storage in an onsite tank farm into an oil tanker. Unfortunately, once the scintillator was in the tanker it appeared cloudy and we chose not to risk filling the remainder of the detector with it. To take advantage of the remaining beam before the summer shutdown, we outfitted the first half of the detector with electronics in May. It took a few more weeks for final safety documents to be approved, but by the last week of May we were permitted to operate the detector 24/7 and receive beam. Due to budget constraints at Fermilab, the beam was operating on a 5 days on, 9 days off schedule, so we were only able to record 15 days of beam during our commissioning period.

We received the first beam in our detector on 5 June 2019. The main thing we noticed when we recorded our first beam data was that the detector was in a much noisier environment than we

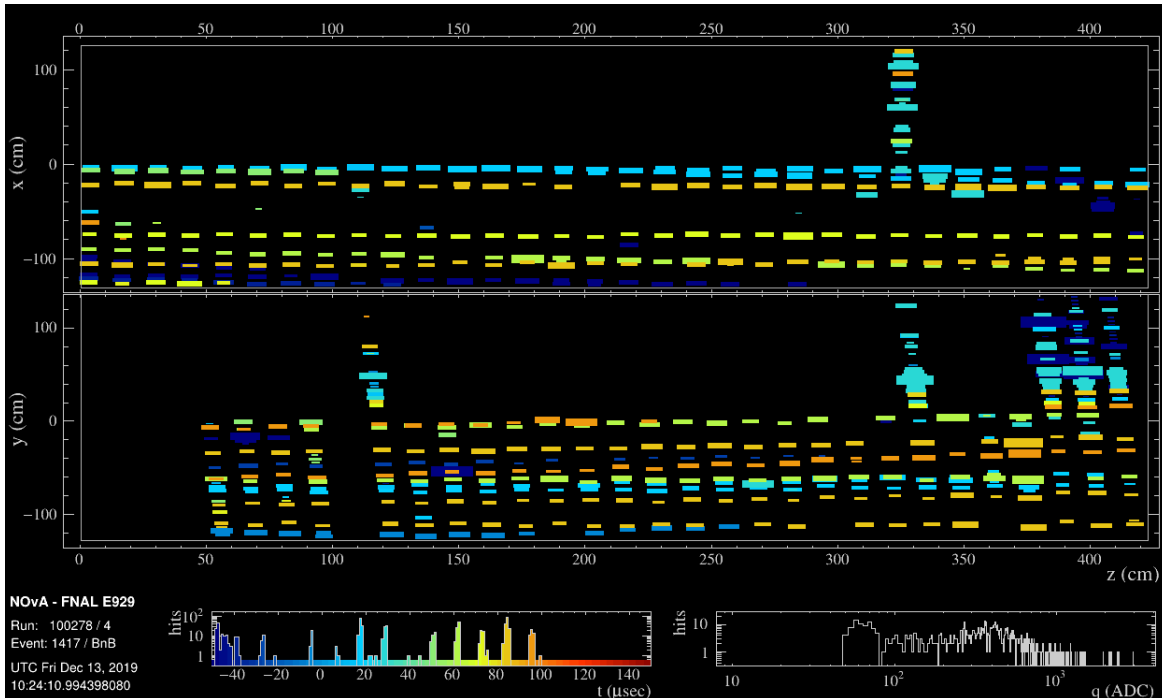


Figure 3.22: Event display of triggered event in period 2. Large blank spaces and gaps are a result of shutoff electronics. The hits that do show up are from high energy muons that passed through the detector during the 150 μ s readout window. The tertiary beam spot is around $x=0$, $y=-7$.

expected. Example event displays showing the noisy environment and electronics shutoffs are in Figure 3.23 and Figure 3.22. A view of the hits on the front face of the detector looking upstream towards the beamline is in Figure 3.24. When a beam spill started, we saw hits in the detector for about the first second of the spill but by the end of the 4.2 s spill the detector electronics had all shut themselves off. At that point in time, the re-enable signal that tells the electronics to turn back on was set to 10 minutes since that was all we needed for the NOvA Near and Far Detectors. By the end of period 1, we reconfigured the re-enable to send a signal at a rate of 10 Hz, which helped some, but was not sufficient to keep the detector live throughout each spill. The spill structure as seen by a single pixel on the detector that shuts off during the spill is in Figure 3.25.

With only 15 days of beam, there was not much time for beam tuning or any studies to figure out where the extra particles were coming from. Once the summer beam shutdown began, we had some time to start looking at the data we collected to learn what we could about the beam plume and to take a look at the beamline triggers we had collected. I studied the tracks in the detector to try to determine their direction and determine a common source. Unfortunately, the exact detector

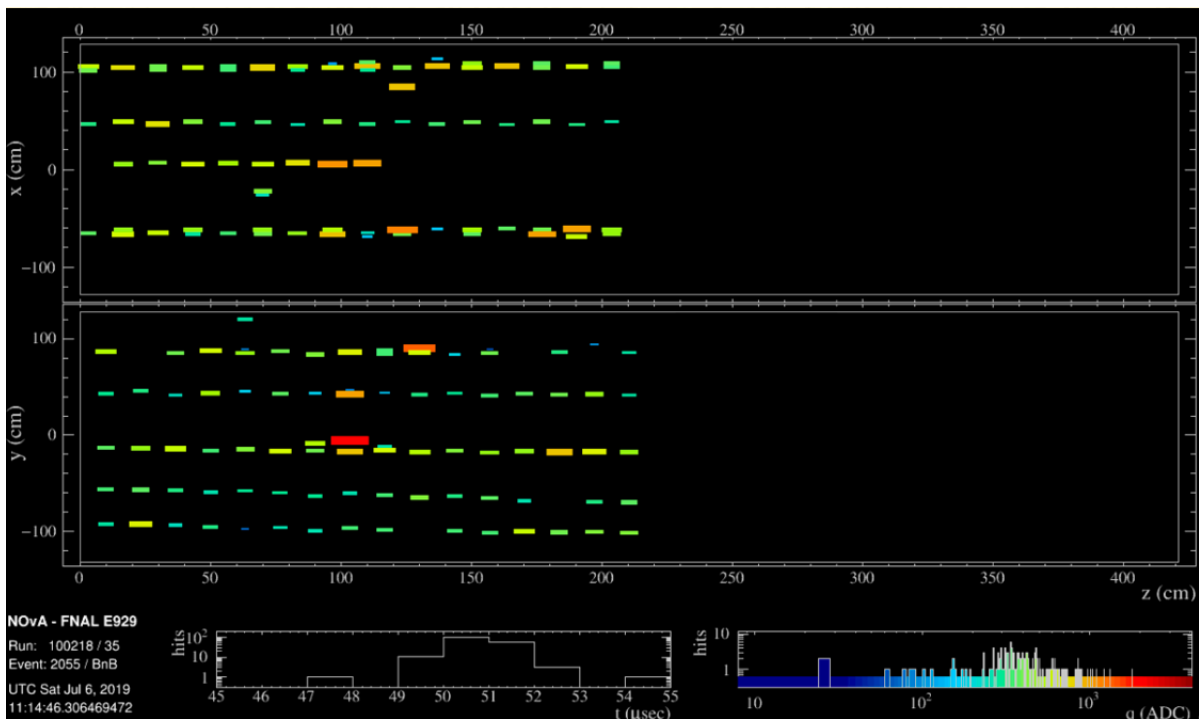


Figure 3.23: Event display of triggered event in period 1 zoomed in on the 10 μ s around the particle that caused the trigger. Even though there are no clear signs of electronics shutoff, there are a number of particles passing through the detector alongside the particle of interest. The second block was not active for period 1.

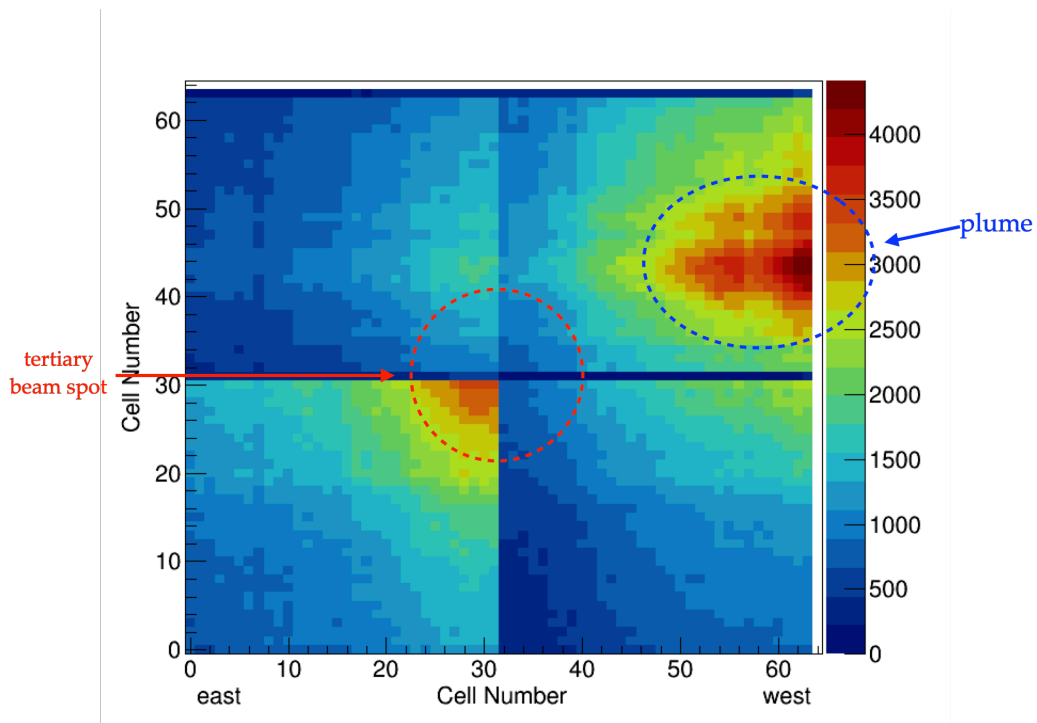


Figure 3.24: Hits on the front face of the NOvA detector, looking upstream towards the beamline. The tertiary beam spot is approximately centered on the detector, while the beam plume is most prominent in the upper west quadrant. The beam spot is most visible in the lower east quadrant because the electronics in this region do not shut off as much as in the other three quadrants.

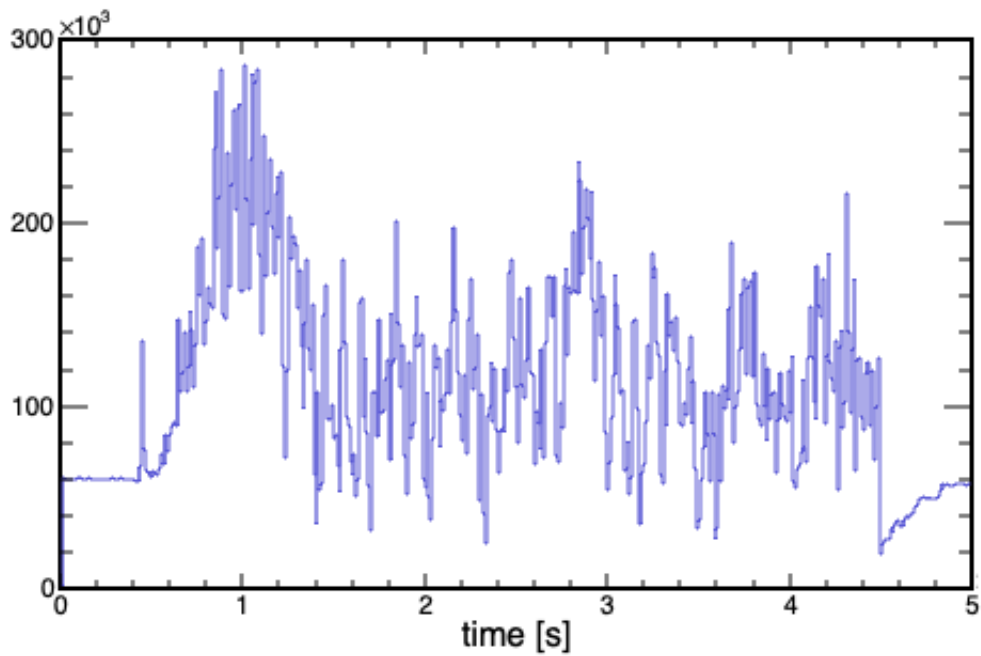


Figure 3.25: Hits on a pixel during the 4.2 s spill found by counting up hits on a single pixel in the NOvA detector and integrating over multiple spills. Data collected with a beam intensity of 5×10^9 ppp. You can see the initial ramp-up of the beam and then a drop from the electronics shutting off. Throughout the spill the electronics are turned back on at a rate of 10 Hz and then shut off again once their buffers fill up.

geometry placement relative to the axis of the beamline was uncertain at this point, so they pointed back to a point above the beamline. The profiles of where tracks in the upper west quadrant of the detector point back to, tracing back from the front face of the detector using the direction of tracks in the detector, are in Figure 3.26. Ultimately, we were not able to determine the source of the beam plume with data from period 1, but with no obvious peak within the tertiary beamline we were fairly confident the source of the beam plume was upstream of our beamline. Without more information we had to wait until we had beam again to learn more about the beam plume. To try to prevent shutoffs, we asked one of the developers of the FEB firmware to create a new firmware with an expanded buffer. In the end, we had two more firmware versions with $\times 8$ and $\times 16$ buffer depths. See chapter 4 for more details about electronics shutoffs.

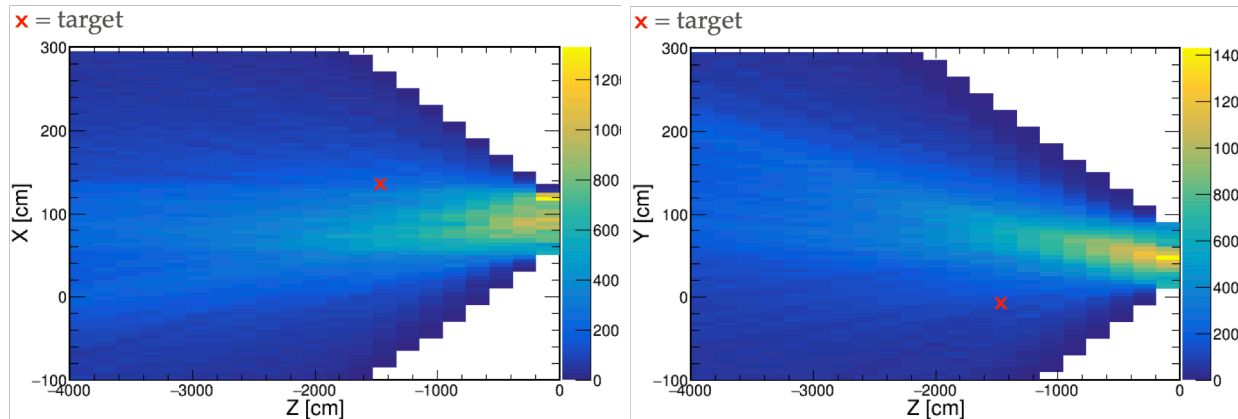


Figure 3.26: Top (left) and side (right) views of where tracks in the upper west region of the detector point back to. The front face of the NOvA detector is at the far right side of the plot and the location of the secondary target is indicated with a red x.

In parallel to the analysis work done during the beam shutdown to try to find the source of the beam plume, we worked on deciding what to do to resolve the cloudy scintillator problem. In the end, we shipped spare scintillator that had been stored in totes at the Far Detector site in Ash River, MN and drums stored at the University of Texas at Austin to Fermilab. The first two thirds of the second block was filled with the Ash River scintillator, and the remaining third was filled with the Texas scintillator. We account for the slightly different light yield of the scintillators was account for in data through our standard calibration process, and in simulation with a cell by cell brightness file. More details about this are in chapter 6. Following the filling, we outfitted the rest of the detector with electronics and we were able to take our first cosmic data with the full detector active on 26

November 2019.

We received our first beam to the full detector 6 December 2019. We started out with a trigger based on the coincidence of 3 of 4 WCs, but this was not a very reliable trigger. After about the first week we switched to a TOF-based trigger. The initial configuration of this triggered each time the downstream (DS) TOF saw signal, which resulted in a very high trigger rate, but not many of these triggers had existing reconstruction information for the TOF and/or WC. Once we switched to a configuration that looked at the time difference between signals in each TOF, we had many more trigger with existing TOF reconstruction, and the relative number of events with existing WC information also increased. To further improve the efficiency of our triggers, we decided to trigger on the coincidence of scintillator paddles that were placed immediately upstream of each WC. This increased the percentage of triggers that had both WC and TOF information from 7.2% to 15.9%. See Table 3.1 for more details about the efficiency of various trigger configurations. There were a handful of tests run throughout the rest of period 2, but from 23 January to 20 March 2020 the majority of the data was taken with the 4-of-4 scintillator paddle coincidence trigger.

Trigger	% of events with TOF reco	% of events with WC reco	% of events with TOF & WC reco
TOF Prompt	81.7	7.7	7.2
3 of 4 scintillator paddle	8.3	9.4	4.3
4 of 4 scintillator paddle	22.6	28.6	15.9

Table 3.1: Efficiencies for beamline trigger conditions. For the majority of period 2, we ran with the 4 of 4 scintillator paddle trigger.

Most of the rest of the condition changes during period 2 were beam related, expect for the FEB firmware changes. There were a number of secondary beam intensity scans through the period, along with one secondary beam momentum scan and a couple collimator scans. The tertiary magnet current was set to 1000 A (selecting 1 GeV/ c particles) for the majority of the period, expect for one day in February when we performed a tertiary momentum scan, and the final 10 days of beam, for which the current was set to 500 A (selecting 500 MeV/ c particles). Details of the running conditions are summarized in Table 3.2.

As we were running, I ran a weekly analysis to determine how many particles we selected as we varied beam and detector conditions. The basic selection cuts I used were:

- Existing wire chamber reconstruction (requires hits in 8 of 8 WC planes),

Date	Secondary beam intensity [ppp]	Tertiary magnet current [A]	Trigger	FEB firmware
6 Dec 2019	8.5×10^9	1000	3 of 4 WC	v4.10.2E
9 Dec 2019	1×10^{10}	“ ”	“ ”	(nominal FD)
13 Dec 2019	“ ”	“ ”	“ ”	“ ”
16 Dec 2019	“ ”	“ ”	TOF DS	“ ”
24 Dec 2019	5×10^8	“ ”	“ ”	“ ”
3 Jan 2020	1×10^9	“ ”	“ ”	“ ”
7 Jan 2020	“ ”	“ ”	TOF Prompt	“ ”
9 Jan 2020	3×10^9	“ ”	“ ”	“ ”
9 Jan 2020	1×10^9	“ ”	“ ”	“ ”
16 Jan 2020	“ ”	“ ”	“ ”	v4.11.30
23 Jan 2020	“ ”	“ ”	4 of 4 scintillator paddle	($\times 8$ buffer)
28 Jan 2020	“ ”	“ ”	TOF Prompt	“ ”
29 Jan 2020	5×10^9	“ ”	4 of 4 scintillator paddle	“ ”
30 Jan 2020	1.5×10^{10}	“ ”	“ ”	“ ”
“ ”	1×10^9	“ ”	“ ”	“ ”
“ ”	“ ”	“ ”	3 of 4 scintillator paddle	“ ”
3 Feb 2020	“ ”	“ ”	4 of 4 scintillator paddle	“ ”
4 Feb 2020	“ ”	“ ”	“ ”	“ ”
“ ”	2.5×10^9	“ ”	“ ”	“ ”
“ ”	5×10^9	“ ”	“ ”	“ ”
“ ”	7.5×10^9	“ ”	“ ”	“ ”
“ ”	1×10^{10}	“ ”	“ ”	“ ”
5 Feb 2020	“ ”	“ ”	3 of 4 WC	“ ”
6 Feb 2020	“ ”	“ ”	scintillator paddle 2 & 3	“ ”
10 Feb 2020	“ ”	“ ”	3 of 4 scintillator paddle	“ ”
11 Feb 2020	“ ”	“ ”	target counter (prescaled)	“ ”
“ ”	“ ”	“ ”	3 of 4 scintillator paddle	“ ”
12 Feb 2020	“ ”	“ ”	scintillator paddle 3 & 4	“ ”
14 Feb 2020	“ ”	“ ”	“ ”	“ ”
“ ”	“ ”	500	“ ”	“ ”
“ ”	“ ”	750	“ ”	“ ”
“ ”	“ ”	1500	“ ”	“ ”
15 Feb 2020	“ ”	2000	“ ”	“ ”
“ ”	“ ”	1000	“ ”	“ ”
“ ”	“ ”	“ ”	4 of 4 scintillator paddle	“ ”
“ ”	2×10^9	“ ”	“ ”	“ ”
17 Feb 2020	1×10^9	“ ”	“ ”	“ ”
18 Feb 2020	“ ”	“ ”	“ ”	v4.11.33
20 Feb 2020	1×10^{10}	“ ”	“ ”	($\times 16$ buffer)
“ ”	7.5×10^9	“ ”	“ ”	“ ”
“ ”	5×10^9	“ ”	“ ”	“ ”
“ ”	2.5×10^9	“ ”	“ ”	“ ”
“ ”	7.5×10^8	“ ”	“ ”	“ ”
“ ”	1×10^9	“ ”	“ ”	“ ”
4 Mar 2020	1×10^8	“ ”	TOF US	“ ”
“ ”	1×10^{10}	“ ”	4 of 4 scintillator paddle	“ ”
5 Mar 2020	1×10^9	“ ”	“ ”	v4.10.2E
13 Mar 2020	“ ”	500	“ ”	(nominal FD)
20 Mar 2020	beam off	0		

Table 3.2: Running conditions for period 2.

- time of flight > 40 ns,
- track mean time between 45 and 55 μs (we expect the trigger particle around 51-52 μs), see Figure 3.27,
- track in detector with more than 5 hits,
- and track starts within beam spot - $|x| < 20$, $-25 < y < 15$, $z < 10$ [cm], see Figure 3.28.

For particle identification, I included the following cuts, see4-of- Figure 3.5):

- electron: $40 < \text{TOF} < 45$ ns, Cherenkov signal
- muon, pion: $40 < \text{TOF} < 45$ ns, no Cherenkov signal
- kaon: $45 < \text{TOF} < 50$ ns, no Cherenkov signal
- proton: $50 < \text{TOF} < 70$ ns, no Cherenkov signal

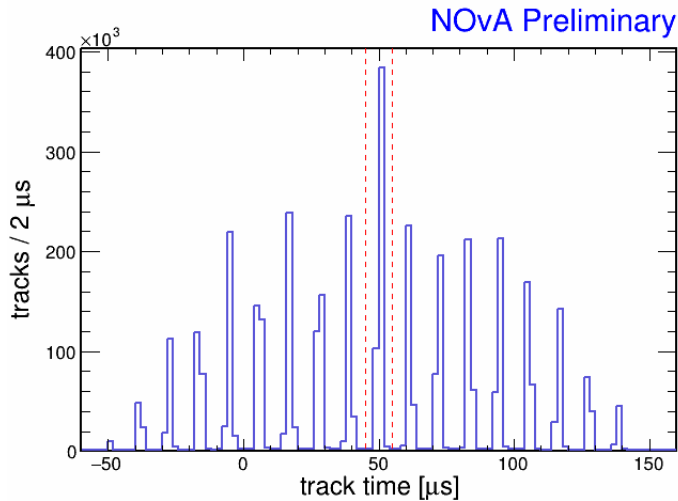


Figure 3.27: Time of tracks in detector. The particle that caused the trigger should enter the detector around 51-52 μs . Peaks either side of this are from adjacent buckets of beam, spaced 11.2 μs apart.

The total number of particles of each type selected per day are shown in Figure 3.29a. There were no electrons selected in December because the digitizer channel the Cherenkov readout was connected to was broken. It was swapped to a different channel on 27 December 2019, but then there was a beam downtime until the new year. The dropoff in particle rate after 9 March 2020 is due to reduction in a collimator opening in the secondary beamline. This was done to try to reduce electronics shutoffs, but it also greatly reduced the number of beamline triggers, so the change was reverted on 16 March 2020. We ran with a tertiary magnet current of 500 A 13-20 March 2020,

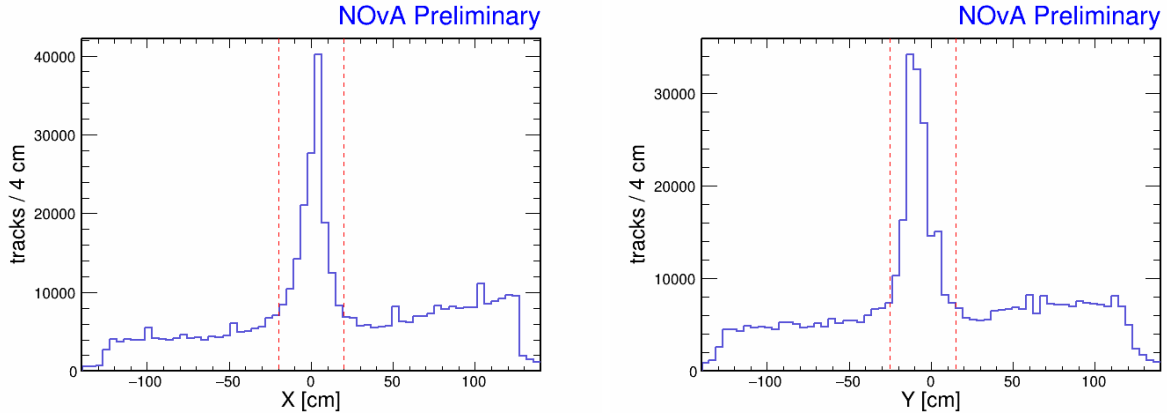


Figure 3.28: X (left) and Y (right) start location of in-time tracks in the detector. In-time tracks have a mean time between 45 and 55 μ s.

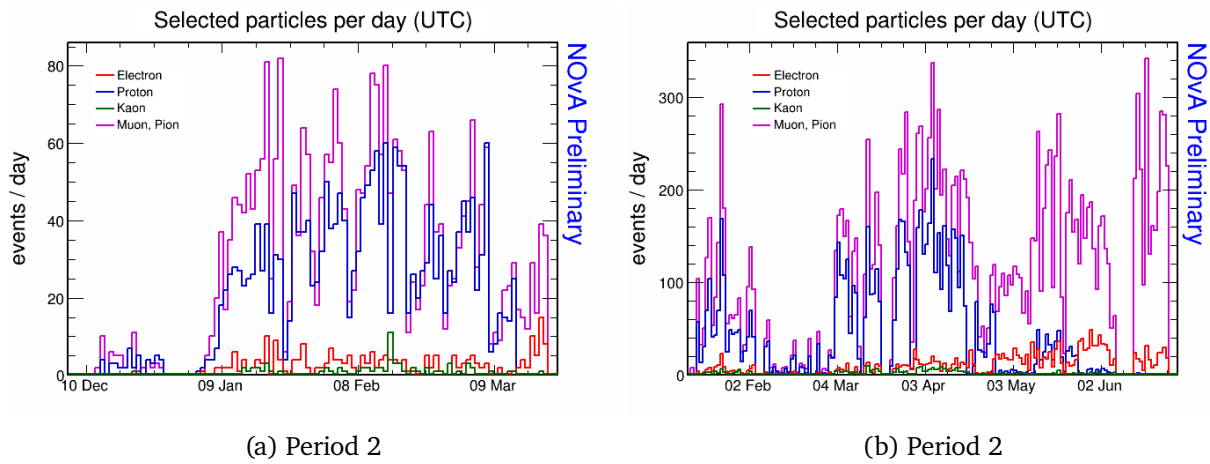


Figure 3.29: Number of particles passing basic selection cuts in periods 2 (left) and 3 (right).

leading to more electrons and fewer of everything else. In total, without accounting for electronics shutoffs, we have 239 electrons, 2983 pions and muons, 70 kaons, and 2126 protons from period 2.

Period 2 ended earlier than planned with a long beam shutdown starting 20 March 2020. We installed concrete blocks upstream of the tertiary beamline to shield some of the high energy muons in an attempt to decrease the beam plume and therefore electronics shutoffs. Beam returned to Test Beam 12 January 2021, marking the beginning of period 3. There was significantly more beam tuning done at the beginning of period 3. Unfortunately, tuning the 1.5 miles of beamline devices upstream of the tertiary beamline is non-trivial and the good particle rates in February were lower than most of period 2, but at the beginning of March we started seeing good particle rates again, with another increase after some additional tuning towards the end of the month. The TOF cuts for particle selection were adjusted for period 3 since we moved the downstream TOF from after to before the Cherenkov detector. Different TOF cuts were also used for the various tertiary momentum settings. Selected particles per day for period 3 are in Figure 3.29b. In total, without accounting for electronics shutoffs, we have 1767 electrons, 18648 pions and muons, 293 kaons, and 6720 protons from period 3. These particles were collected with momenta of $1 \text{ GeV}/c$, $750 \text{ MeV}/c$, and $500 \text{ MeV}/c$. For the majority of the period the magnet was set to positive polarity, selecting positively charged particles. More details on the running conditions are in Table 3.3. The analysis in the following chapters only uses data from period 2.

Date	Secondary beam intensity [ppp]	Tertiary magnet current [A]	Trigger	FEB firmware
12 Jan 2021	1×10^9	1000	4 of 4 scintillator paddle	v4.10.2E
19 Jan 2021	5×10^8	“ ”	“ ”	“ ”
“ ”	1×10^8	“ ”	“ ”	“ ”
20 Jan 2021	“ ”	“ ”	“ ”	“ ”
16 Feb 2021	“ ”	“ ”	“ ”	v4.11.35
“ ”	5×10^9	“ ”	“ ”	“ ”
18 Feb 2021	“ ”	“ ”	“ ”	v4.11.33
“ ”	“ ”	“ ”	“ ”	v4.10.2E
24 Feb 2021	“ ”	“ ”	“ ”	“ ”
8 Mar 2021	“ ”	“ ”	“ ”	“ ”
“ ”	9×10^9	“ ”	“ ”	“ ”
“ ”	7×10^9	“ ”	“ ”	“ ”
“ ”	3×10^9	“ ”	“ ”	“ ”
“ ”	1×10^9	“ ”	“ ”	“ ”
13 Mar 2021	5×10^9	“ ”	“ ”	“ ”
14 Mar 2021	3×10^9	“ ”	“ ”	“ ”
17 Mar 2021	7×10^9	“ ”	“ ”	“ ”
18 Mar 2021	5×10^9	“ ”	“ ”	“ ”
22 Mar 2021	4×10^9	“ ”	“ ”	“ ”
24 Mar 2021	3×10^9	“ ”	“ ”	“ ”
29 Mar 2021	“ ”	500	“ ”	“ ”
30 Mar 2021	“ ”	750	“ ”	“ ”
“ ”	“ ”	1000	“ ”	“ ”
5 Apr 2021	4×10^9	“ ”	“ ”	“ ”
6 Apr 2021	3×10^9	“ ”	“ ”	“ ”
16 Apr 2021	“ ”	-1000	“ ”	“ ”
17 Apr 2021	“ ”	-750	“ ”	“ ”
18 Apr 2021	“ ”	-500	“ ”	“ ”
19 Apr 2021	“ ”	1000	“ ”	“ ”
26 Apr 2021	“ ”	500	“ ”	“ ”
10 May 2021	“ ”	750	“ ”	“ ”
24 May 2021	“ ”	500	“ ”	“ ”
12 Jun 2021	“ ”	-750	“ ”	“ ”
24 Jun 2021	beam off	0		

Table 3.3: Running conditions for period 3. FEB versions: v4.10.2E (nominal FD), v4.11.35 ($\times 16$ w/ shutoff bit), and v4.11.33 ($\times 16$ buffer).

Chapter 4

Accounting for Detector Electronics Shutoff

4.1 Front End Board Shutoffs

The NOvA detector electronics are designed to read out 100% of the time, sending all data to a circular buffer from which data is then written to disk if it meets various trigger conditions. Before data is sent to the circular buffer, it is stored in a small buffer internal to the front end boards (FEBs). If this internal buffer fills up, the FEB shuts off until it receives a re-enable signal from the DAQ. Under typical conditions at the Near and Far Detectors, this buffer filling up is an indication of a noisy pixel on an APD or a noisy front end board. Because of our beam plume, the Test Beam Detector is in a much noisier environment than our Near and Far Detectors, leading to much higher hit rates and therefore a higher rate of electronics shutting off. We send a re-enable signal to all FEBs at a rate of 10 Hz, but if the buffer on a given FEB has not cleared yet, the FEB will not turn back on until the buffer has cleared and the re-enable signal is received again. If an FEB is shutoff when a particle passes through the detector, the energy deposited in the corresponding cell(s) will not be recorded. Given the importance of accurate energy reconstruction, we need a way to determine if part of the detector was shutoff for a given event. For each FEB that shuts off, we lose half of a plane in the detector (bottom or top half for horizontal planes, east or west for vertical planes). Figure 4.1 shows an example of high-intensity beam causing shutoffs in much of the detector. We ran at a lower intensity for the majority of our run to mitigate this effect, but we still saw shutoffs.

For data taken with FEB firmware version v4.10.2E, we have access to a bit in the FEB status register that flips when the FEB is shut off. The way this bit is recorded within the data, we either receive the bit in the last nanoslice reported by the FEB prior to shutting off, or in the first nanoslice reported after it has been re-enabled. The only way to know if an FEB has been re-enabled is if it sees a hit. New FEB firmware was created with $\times 8$ (v4.11.30) and $\times 16$ (v4.11.33) buffer available in an attempt to mitigate the shutoffs. The $\times 8$ firmware was tested and rolled out on the detector 16 January 2020, with the $\times 16$ rolled out on 18 February 2020. While the newer firmware versions did reduce shutoffs, the FEB status register no longer changed with shutoffs, making them more

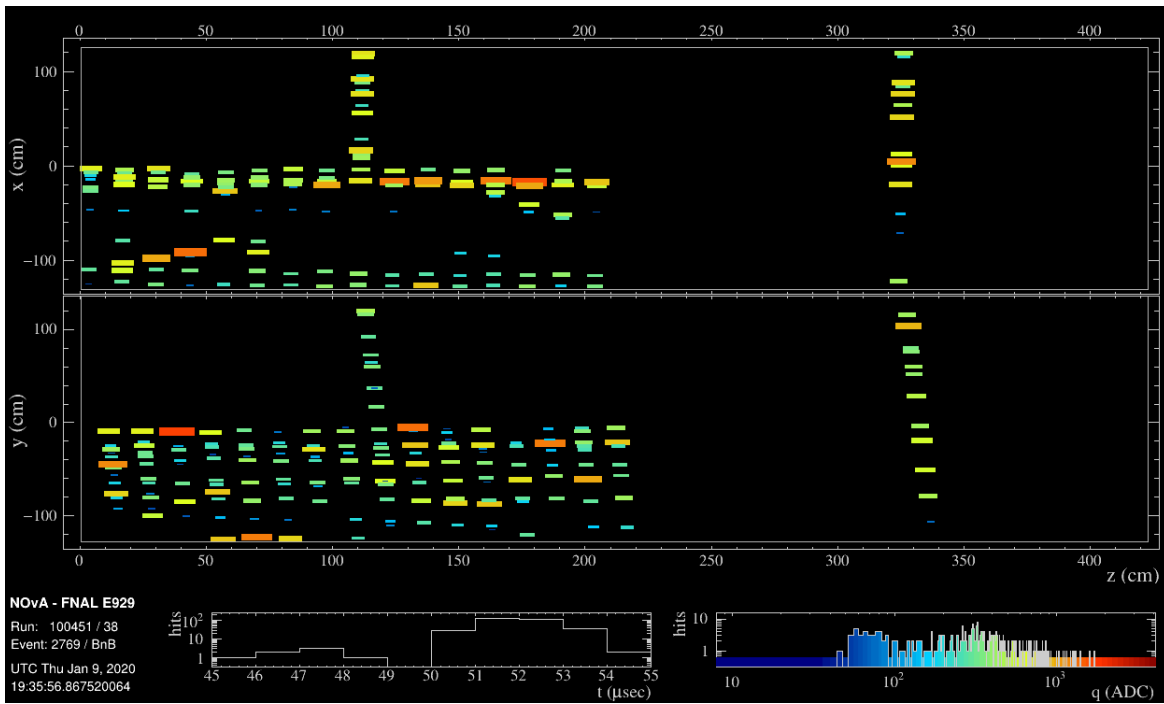


Figure 4.1: Event display of selected event, zoomed in on the 10 μ s around the particle that caused the trigger. At least half of the v4 FEBS in the first block and all of the v4 FEBS in the second block are missing, indicating they were likely shut off during the event. The line of cells lit up in the middle of each block is from the v5 FEBS.

difficult to keep track of. We rolled back to the original firmware on 5 March 2020.

Since not all our data was recorded with the status bit available, and due to the uncertainty on whether the bit is reported before or after the shutoff, I developed a different method to track shutoffs in the detector. Since the development of this infrastructure, we discovered there are two different classes of shutoffs: the individual FEB shutoffs described above, and Data Concentrator Module (DCM) dead time in which groups of 8 FEBs on a DCM, up to the entire DCM, will stop reporting for a period of time, often on the order of milliseconds. The v4 FEBs on the first block of the detector are read out by one DCM, the second block by another DCM, and the v5 FEBs in the middle of each block are read out by a third DCM. Each DCM has 60, 58, and 8 FEBs connected to it. The DCM with the 8 v5 FEBs has much less data throughput, so dead time on this DCM is much less frequent than on the others. Although the following infrastructure was not designed with the dead time in mind, since it uses hit rate information to search for shutoffs it should still catch instances of DCM dead time along with FEB shutoffs.

4.2 Overall Infrastructure Description

We record $150\ \mu\text{s}$ long events for each particle that meets our tertiary beamline trigger conditions. In addition to this Beamline stream, we have a Spill data stream that is a continuous 5 s of data, approximately centered on the 4.2 s beam spill. These Spill triggers are split up into 25 200 ms long sub-triggers. From this data stream, we can obtain FEB hit rate information for a time window before and after the event time of interest (ie. the trigger time of a selected proton).

The idea behind the shutoff infrastructure is to use FEB hit rate information from the Spill data stream to determine if any FEBs were shutoff for an event in the Beamline data stream. Given a selected event in the Beamline data stream, you can then find the corresponding event(s) in the Spill data stream based on run, subrun, and event time. Once you have the event(s) you need, you can count up the hits on each FEB in the event in a given time window before and after the event time of interest, and if both are above a given cutoff, the FEB is considered active. If any FEB in an event is determined to be shutoff, then the event as a whole is marked as a ‘shutoff’ event. Depending on where the shutoff electronics are in the detector relative to where the beamline particles pass through, it is possible that an event will be unaffected by the shutoffs. Each event has a map of

which electronics were shutoff associated with it that can be used to determine if an event with shutoffs contains good data. It is up to the individual analyzer to either use this map or reject all events that have any shutoffs in them.

Starting with a list of selected events, I generated a list of timestamps and run/subrun combinations to produce a list of files in the Spill data stream to process. Since these files take a relatively long time to process, I applied a time-based filter to select only the sub-triggers within 320 ms of the selected event times. After applying this filter, I ran a process that applies calibration to the hits in the file to obtain precise timing information for each hit in the detector. I then ran a process over the events that, for each selected event, counts the number of hits on each FEB in a given, configurable, time window before and after the event time.

4.2.1 Tuning the time window and cut on number of hits

I did some simple tuning to optimize the time window to check before and after the event, and the number of hits required to consider an FEB ‘good’, or active. In the FD firmware (v4.10.2E) data from epochs 2a,f, there were 1312 events passing the selection criteria listed below. With this firmware, if an FEB shutoff occurs, a status bit within the DAQ is flipped. This typically is recorded in data in the last nanoslice the FEB sends prior to shutting off, though occasionally it is reported in the first nanoslice after re-enable instead. If there were no more hits on the FEB immediately after the buffer filled up, then there will not be a nanoslice sent with the shutoff bit active. I applied the following criteria to select events for use in tuning the number of hits and time window requirements:

1. momentum from wire chamber track > 0 ;
2. time of flight > 40 ns;
3. reconstructed track in the detector which:
 - (a) starts within the beam spot on the front face of the detector ($-20 < x$ [cm] < 20 , $-25 < y$ [cm] < 15 , $z < 10$ cm); and
 - (b) has an average hit time between 45-55 μ s (we expect the triggered particle around 51-52 μ s).

1D distributions for the number of hits in various time windows before and after the event time are shown in Fig. 4.3, with the distributions broken up by whether an FEB reported a shutoff bit in Fig. 4.4. These distributions are plotted against FEB number in Fig. 4.5. Multiple time

window and number of hit, n_{hit} , requirements were applied to the selected events. Each event that passed or failed the shutoff requirements was checked against events that either had no FEB shutoff bits (as indicated by the DAQ), or events that had at least one FEB shutoff. The number of events falling into each category are displayed in Table 4.1. The goal in tuning was to minimize the off-diagonal elements in these tables. These show us our false positives (events that passed the cuts in the module but had at least one FEB shutoff indicated by the DAQ) and false negatives (events that failed cuts despite having no FEB shutoffs). From the data in Table 4.1, 10 ms was chosen as the optimal time window. The results of different n_{hit} cuts are in Table 4.2. Based on this data, a cut of $n_{hit}_{\{pre,post\}} > 0$ hits was chosen.

For a time window of 10 ms and a cut of $n_{hit}_{\{pre,post\}} > 0$,

- 1052/1312 (80%) events passed the cuts;
 - 30 of the 1052 that passed had at least 1 FEB that reported an FEB shutoff;
 - * 16 of these were from 1 FEB - dcm-5-01-02:42.
- 114 of the 260 that failed had at least 1 FEB that failed with no shutoff bit;
 - 89 of these had other shutoff bits in the event, leaving
 - 25 events that failed despite having no FEB shutoff bits;
 - * 19 of these were from 1 FEB - dcm-5-01-02:42.

dcm-5-01-02:42 spent a couple days going in and out of cooling alarms, and eventually we disabled cooling on this FEB. Ignoring this FEB, these cuts led to 14 false positives (1%) and 6 false negatives (2%).

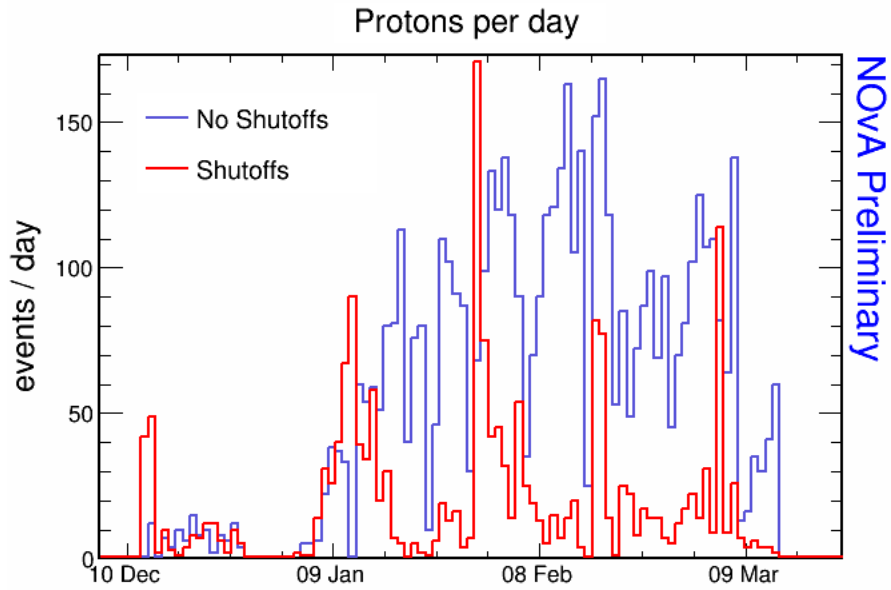
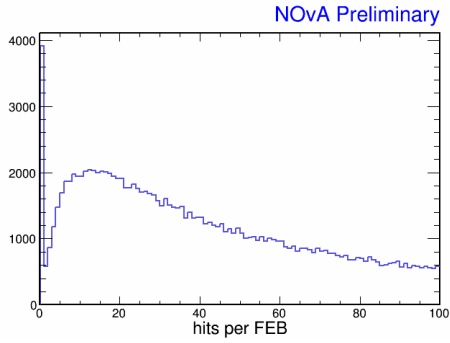


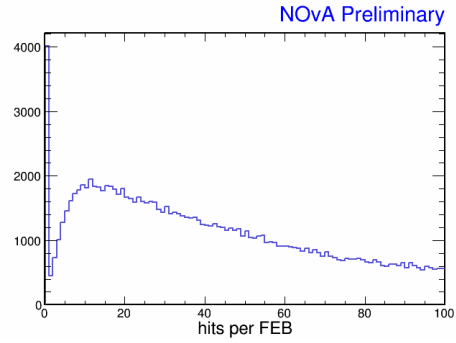
Figure 4.2: Shutoff status for selected protons plotted against time for period 2. Spikes in shutoffs correspond to days when we ran at higher intensities for various intensity studies and other beam tuning.

	No FEB shutoffs	At least one FEB shutoff	Total		No FEB shutoffs	At least one FEB shutoff	Total
Event passed	969	28	997	Event passed	1022	30	1052
Event failed	78	237	315	Event failed	25	235	260
Total	1047	265	1312	Total	1047	265	1312
(a) 5 ms, $\text{nhit}_{\{\text{pre},\text{post}\}} > 0$				(b) 10 ms, $\text{nhit}_{\{\text{pre},\text{post}\}} > 0$			
	No FEB shutoffs	At least one FEB shutoff	Total		No FEB shutoffs	At least one FEB shutoff	Total
Event passed	1020	33	1053	Event passed	1023	57	1080
Event failed	27	232	259	Event failed	24	208	232
Total	1047	265	1312	Total	1047	265	1312
(c) 10 ms, $\text{nhit}_{\{\text{pre},\text{post}\}} > 5$				(d) 50 ms, $\text{nhit}_{\{\text{pre},\text{post}\}} > 5$			

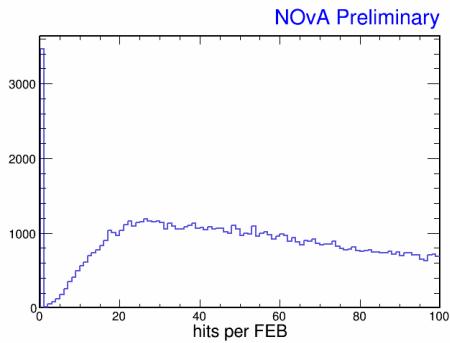
Table 4.1: Cuts applied to 1312 selected events with shutoff bit information available. Rows show events that passed or failed based on the cuts being tuned for the EventFEBStatus module. Columns show events that did or did not have FEB shutoffs based on the status bit information from the DAQ. Off diagonal elements show the false positives and false negatives.



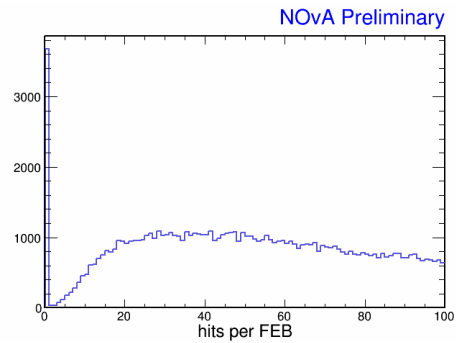
(a) Hits in 5 ms before event time



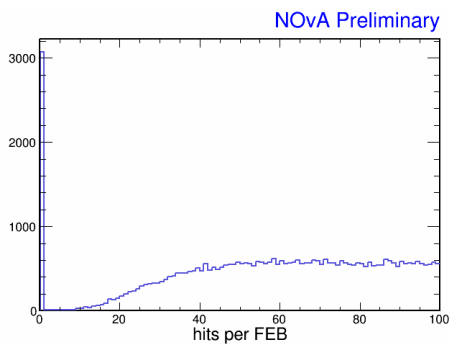
(b) Hits in 5 ms after event time



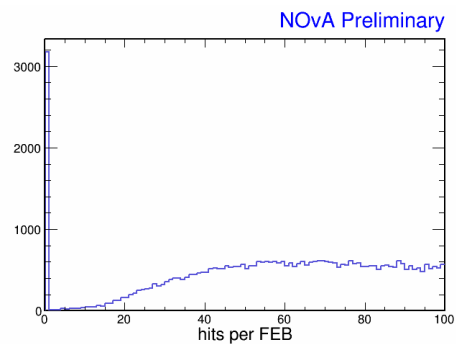
(c) Hits in 10 ms before event time



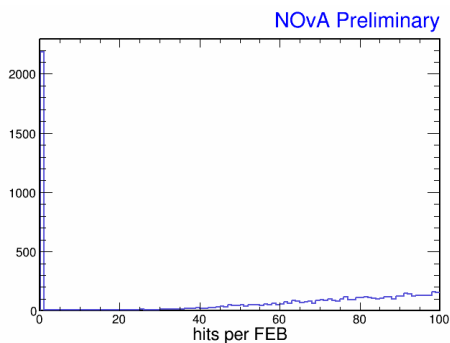
(d) Hits in 10 ms after event time



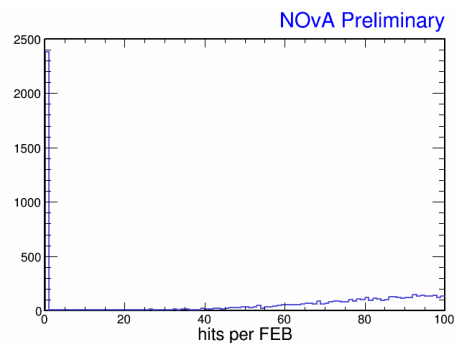
(e) Hits in 20 ms before event time



(f) Hits in 20 ms after event time



(g) Hits in 50 ms before event time



(h) Hits in 50 ms after event time

Figure 4.3: Number of hits in a given time window before (left) and after (right) the event time of interest. Time window ranges from 5 ms (top) to 50 ms (bottom). The large peak at zero are FEBs that are shutoff, while the population of FEBs with non-zero hits in the time window are presumed to be active. I chose a time window of 10 ms (Figure 4.3c and Figure 4.3d).

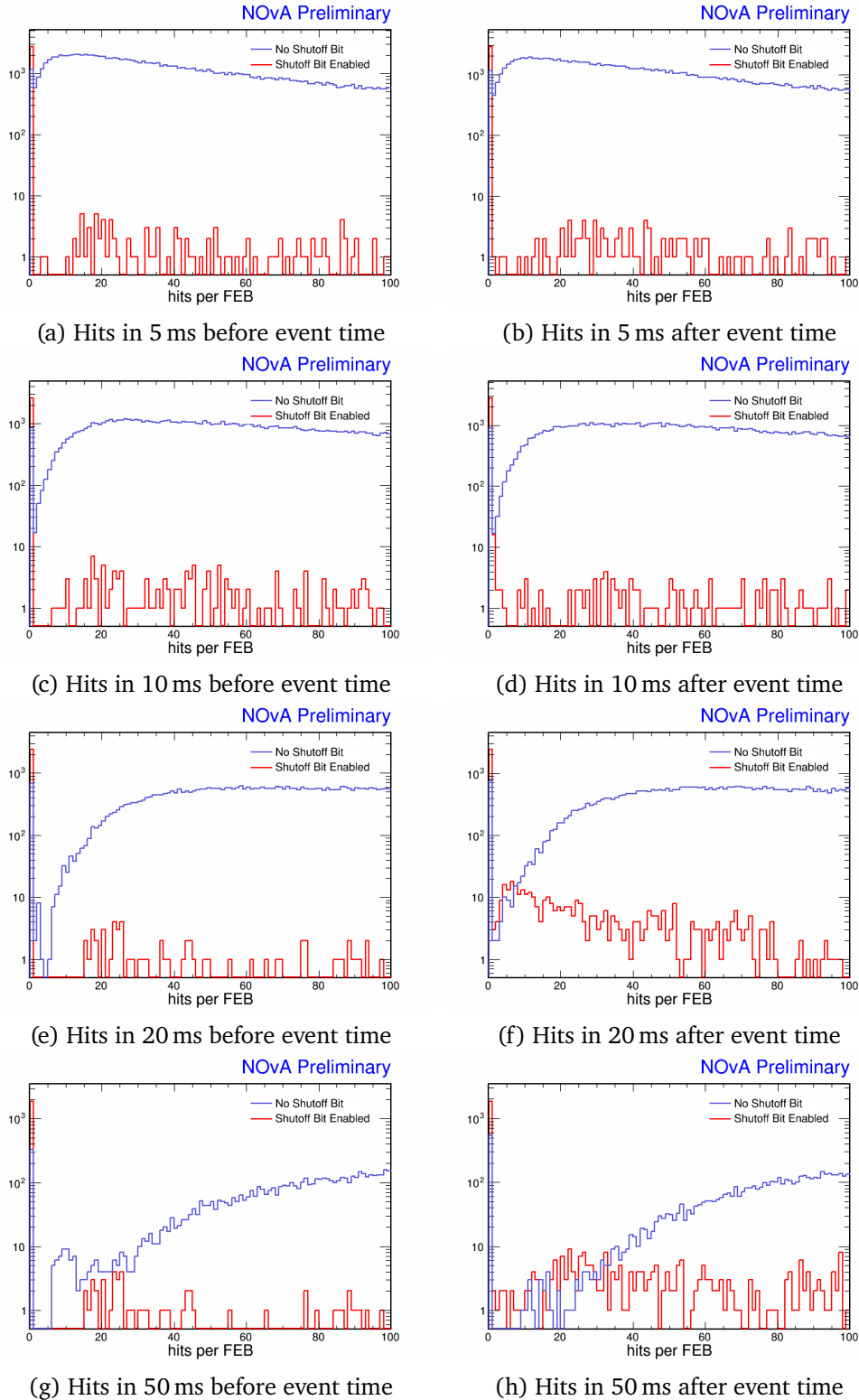


Figure 4.4: Number of hits in a given time window before (left) and after (right) the event time of interest. Time window ranges from 5 ms (top) to 50 ms (bottom). The red line shows FEBs that reported a shutoff during the 110 ms prior to the event, while the blue line shows FEBs that were not shutoff during this time. I chose a time window of 10 ms (Figure 4.4c and Figure 4.4d).

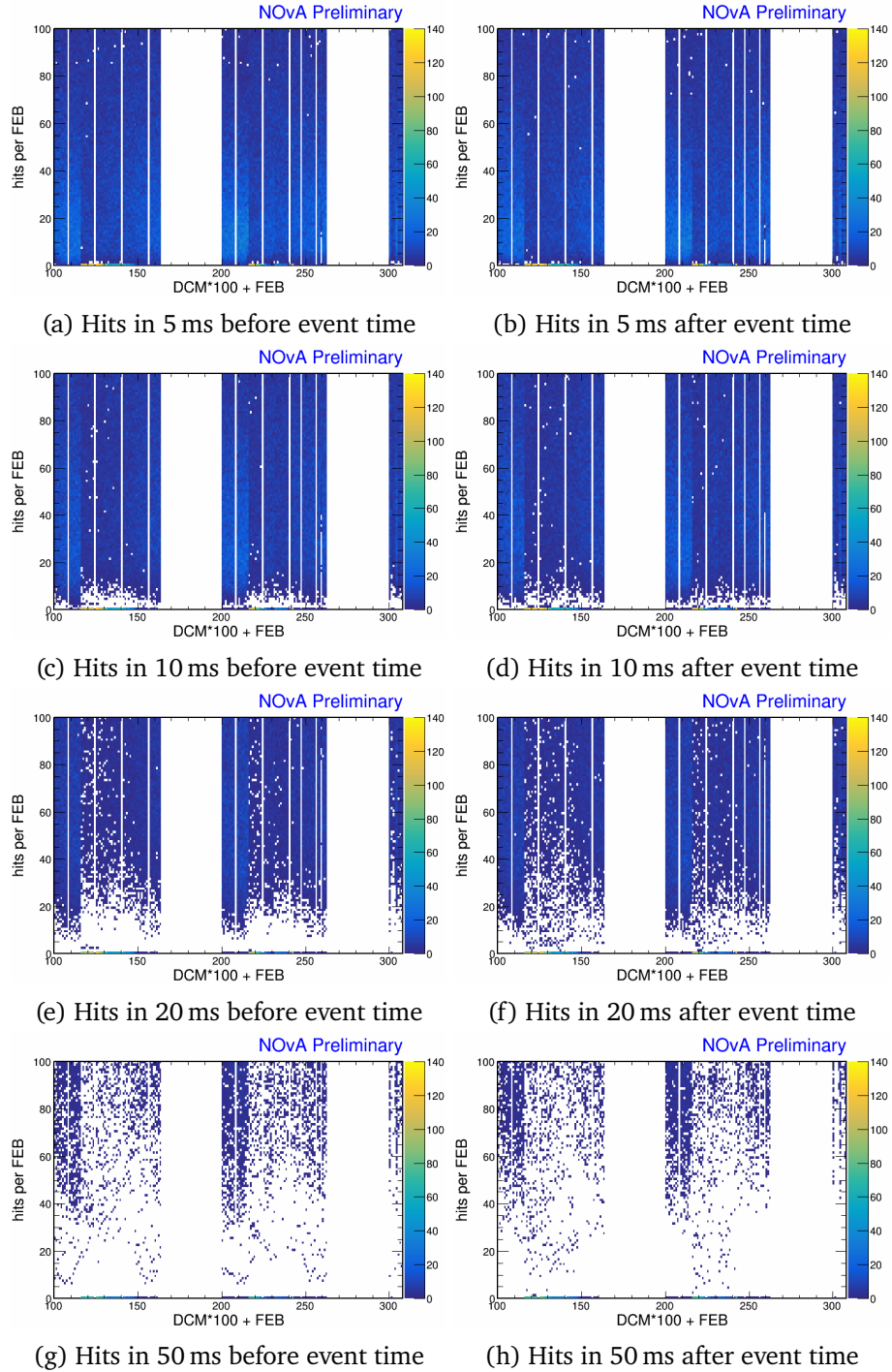


Figure 4.5: Number of hits in a given time window before (left) and after (right) the event time of interest vs. FEB #. Time window ranges from 5 ms (top) to 50 ms (bottom). FEBs 16-31 (west-vertical modules) in both blocks shut off the most frequently, while FEBs 0-15 (east-vertical modules) shut off the least frequently. The beam plume is most intense for the west-vertical modules, then top-horizontal, bottom-horizontal, and finally, east-vertical. DCM 3 contains the ND v5 FEBs which, due to a higher readout rate, shut off less frequently than the FD v4 FEBs using the original firmware (v4.10.2E). The selected time window needs to be long enough to ensure the quietest FEBs have a hit in them so they are not incorrectly marked as shutoff, while keeping it short enough that you do not miss a shutoff due to an FEB being re-enabled at the edge of the window.

	No FEB shutoffs	At least one FEB shutoff	Total
Event passed	1022	30	1052
Event failed	25	235	260
Total	1047	265	1312

(a) 10 ms, $\text{nhit}_{\{\text{pre},\text{post}\}} > 0$

	No FEB shutoffs	At least one FEB shutoff	Total
Event passed	1015	30	1045
Event failed	32	235	267
Total	1047	265	1312

(b) 10 ms, $\text{nhit}_{\{\text{pre},\text{post}\}} > 1$

	No FEB shutoffs	At least one FEB shutoff	Total
Event passed	1001	27	1028
Event failed	46	238	284
Total	1047	265	1312

(c) 10 ms, $\text{nhit}_{\{\text{pre},\text{post}\}} > 2$

	No FEB shutoffs	At least one FEB shutoff	Total
Event passed	947	26	973
Event failed	100	239	339
Total	1047	265	1312

(d) 10 ms, $\text{nhit}_{\{\text{pre},\text{post}\}} > 5$

Table 4.2: Cuts applied to 1312 selected events with shutoff bit information available, focussed on a time window of 10 ms. Rows show events that passed or failed based on the cuts being tuned for the EventFEBStatus module. Columns show events that did or did not have FEB shutoffs based on the status bit information from the DAQ. Off diagonal elements show the false positives and false negatives.

Chapter 5

Data Selection

Over the course of period 2 we recorded over 2 million triggers in 100,000 spills. Many of these triggers were recorded towards the beginning of the period when we ran less efficient triggers, most of which do not have time of flight and/or momentum information from the beamline detectors. In order for an event to be useful for analysis, it needs to have beamline information so I can determine the particle type and momentum; it also needs to be a good quality event in the NOvA detector, without too many coincident overlapping particles and with all the detector electronics reading out. I began by selecting protons using only the beamline information, and checked each of these events for shutoffs in the NOvA detector. Once I had an event for which all detectors were fully reporting, I applied other quality cuts on the track from the wire chambers and the track in the NOvA detector to ensure a clean event for analysis.

I selected particles using the Beamline trigger stream. When a particle passing through the beamline detectors met certain trigger conditions, the data in the beamline detectors was recorded, and a trigger was sent to the NOvA detector. We ran a number of different triggers throughout period 2 as we tried to optimize the number of good triggers. The triggers fell into two categories based on the beamline system they used: 1) time of flight (TOF) based triggers that required either signal in a single TOF detector or a time difference between signals in both TOF detectors and 2) scintillator paddle based triggers that required a coincidence of scintillator paddles located downstream of each wire chamber. Table 3.2 has details about the specific triggers we ran throughout period 2. When the NOvA detector receives a Beamline trigger, it writes out data beginning at least $50 \mu\text{s}$ before the time the particle passed through the beamline detectors. This data stream records $150 \mu\text{s}$ of data for each particle. We combine the data from the beamline detectors and the NOvA detector in the first stage of our offline processing, using timestamps from the two timing units to match the data.

From the beamline we have information about the particles time of flight, momentum from wire chamber tracks, and electron discrimination from a Cherenkov detector. In the first stage of selection, I looked at only the beamline information to select $\sim 1 \text{ GeV}/c$ momentum protons with

good wire chamber (WC) tracks. Since we did not vary the tertiary beam momentum frequently in period 2, I applied a simple run range cut to select the runs we took with the tertiary magnet current set to 1000 A, corresponding to particles with momentum of approximately 1 GeV/c. To select protons, I required a time of flight between 52 and 70 ns and no signal in the Cherenkov detector. Finally, I required an existing WC track. The time of flight and momenta of particles from 1000 A runs is shown in Figure 5.1. The first round of cuts, summarized in Table 5.1 and Table 5.2, selected 7195 protons.

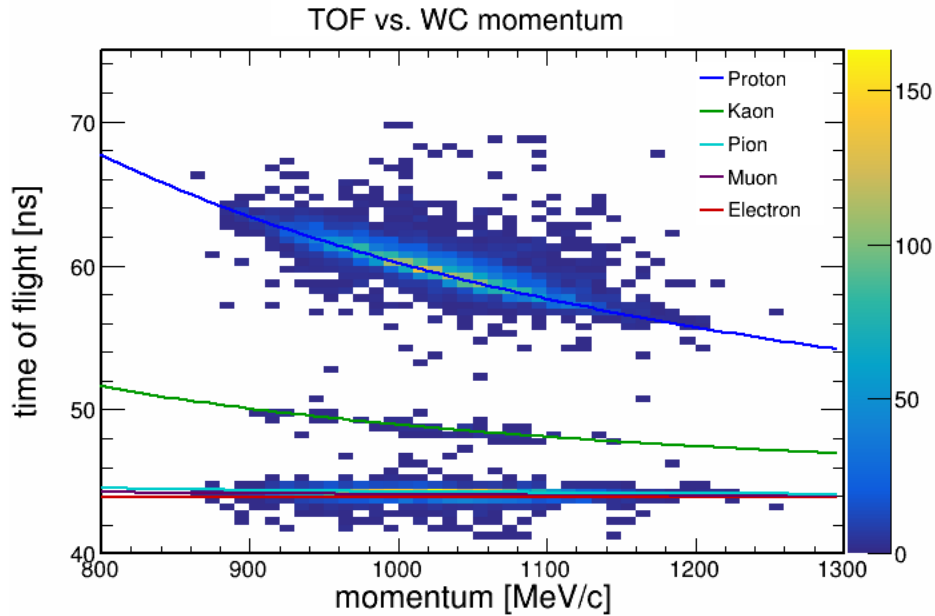


Figure 5.1: Time of flight vs. momentum for beamline particles from 1000 A runs. Lines overlaid are theoretical curves assuming a path length of 13.2 m between the time of flight detectors. Particles with a time of flight between 52 and 70 ns were identified as protons.

1000 A runs	$(100224 \leq \text{run} < 100668) \parallel (100673 \leq \text{run} < 100827)$
TOF	$52 \text{ ns} < \text{time of flight} < 70 \text{ ns}$
No Cherenkov signal	Cherenkov ADC = 0
Existing wire chamber track	WC momentum > 0

Table 5.1: First round of cuts applied to events to select $\sim 1 \text{ GeV}/c$ protons.

As discussed in chapter 4, the NOvA Test Beam detector has a big problem with the high rate environment that causes the electronics to shut off until they can clear their buffer(s) and receive a signal to turn back on. If any part of the detector the proton is passing through is shutoff, it will not record the energy in that location. For range-based energy calculations this only affects the energy if we miss hits at the beginning or end of the track. For calorimetric energy, missing any hits along

	# of triggers
Period 2	2,477,653
1000 A	2,436,456
TOF reconstruction exists	88,935
WC reconstruction exists	28,142
TOF & WC reconstruction exist	16,380
Proton selection	7,195

Table 5.2: Number of triggers that pass beamline selection cuts. Time of flight (TOF) and wire chamber (WC) reconstruction requirements only check for the existence of reconstruction, not the value of the parameter. Proton selection requires $52 \text{ ns} < \text{time of flight} < 70 \text{ ns}$ and no signal in the Cherenkov detector, along with an existing wire chamber track.

the track will lead to a measurement of lower energy. We want to ensure the events we use are not impacted by shutoffs. Using the infrastructure discussed in chapter 4, I rejected any event that showed an indication of shutoffs anywhere in the detector. This infrastructure is not perfect, so it is possible there are still events in the sample with electronics that are shutoff, but this should take care of the majority of them. Following the removal of shutoffs, I had 5354 protons.

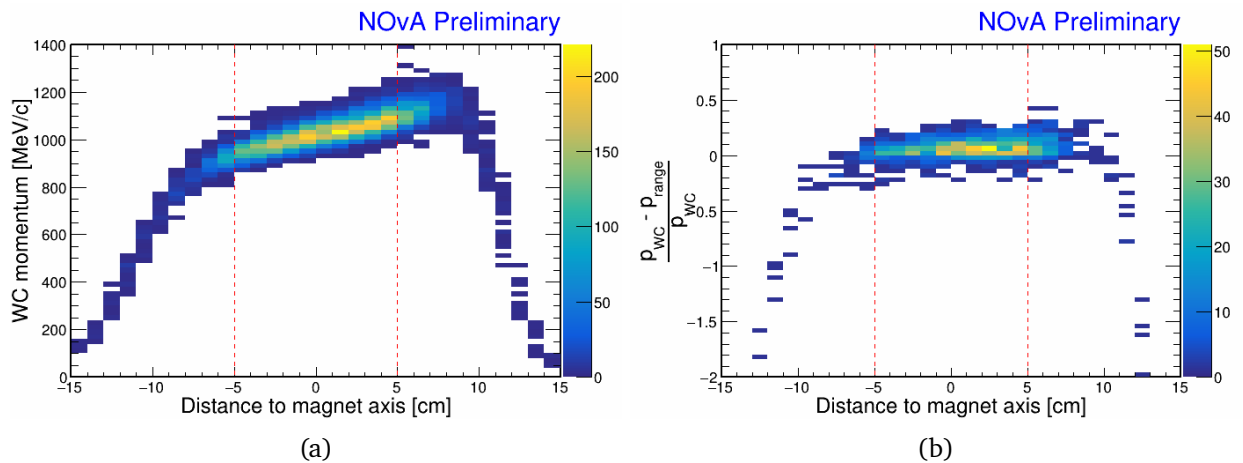


Figure 5.2: Left: Momentum calculated from wire chamber (WC) track plotted against the distance in the horizontal (XZ) plane between where the track enters the magnet and the central axis of the magnet. Right: Fractional difference in momentum calculated using range in the detector and using the WC track. The west side of the magnet is the positive side. The magnetic field will bend particles towards the west. Events outside of the red lines are rejected.

I then applied further selection on the quality of the WC track by checking both where it intersects with the NOvA detector and where it passes through the magnet. If a particle passes through the edges of the magnetic field, where we do not know the field as accurately as through the center, we will not have as accurate of a momentum measurement for the particle. The magnetic field falls off sharply 10 cm away from the central axis of the magnet in the horizontal plane, but comparing the

momentum calculated using the range of protons in the detector to the momentum from the WC track (see Figure 5.2b) shows that the WC track underestimates the momentum for tracks that pass closer to the center of the magnet than 10 cm. I chose a conservative cut of keeping only events that entered the magnet within 5 cm of the central axis. As an extra check that the WC track lies within our beam spot, I apply a cut on where the track enters the NOvA detector, shown in Figure 5.3. At this point, 5264 protons remain.

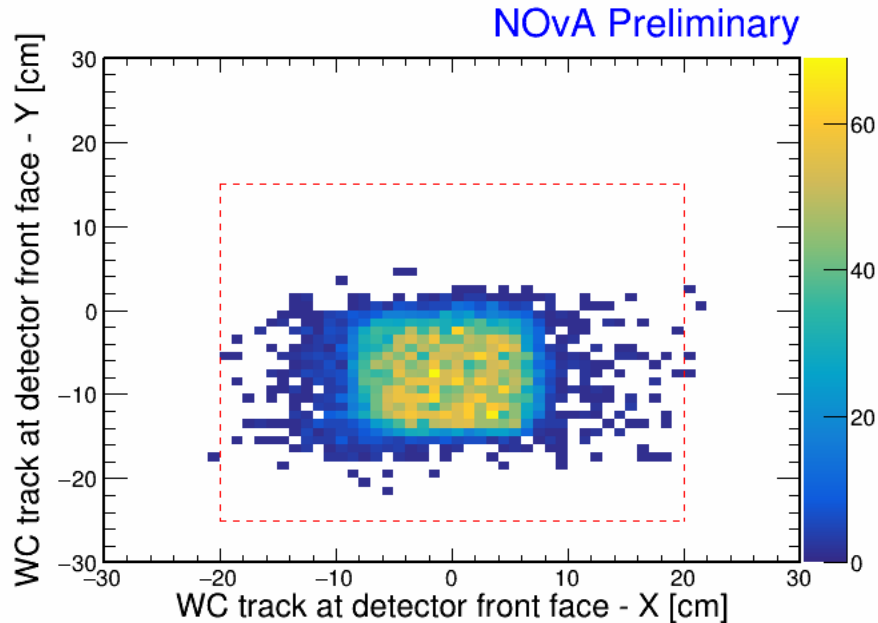


Figure 5.3: NOvA detector (X,Y) coordinates of wire chamber (WC) track where it intersects with the front face of the detector ($Z=0$). Events outside the red box are rejected.

$$\begin{aligned}
 &|\text{Distance between track and central axis of magnet}| < 5 \text{ cm} \\
 &|\text{WC Vertex, X}| < 20 \\
 &-25 < \text{WC Vertex, Y} < 15
 \end{aligned}$$

Table 5.3: Cuts to ensure quality of wire chamber (WC) track.

The remaining cuts serve to further remove potential beam plume contamination, along with ensuring we have long enough tracks in the detector for accurate direction and momentum reconstruction. For the majority of the detector reconstruction, we can reuse algorithms created for and extensively tested on the NOvA Near and Far detectors. There are some minor changes made for this Test Beam specific analysis that I will mention as we go. The first stage of reconstruction in the detector converts hits from (ADC, TDC) values to (GeV, ns) values. Once we have the correct charge and time values, accounting for calibration, we can begin to cluster hits together that are

close in space and time [67]. When adding hits to clusters for Test Beam I added an additional cut that drops any hits outside of the central region of the detector, where the tertiary beam spot is, and outside of a time window zoomed in on when the particle enters the detector. This helps remove some of the plume contamination, making it less likely for extraneous hits to be clustered in with those associated with the proton. When choosing the values for the timing cut, I noticed two distinct peaks in the distribution, shown in Figure 5.4. Plotting the hit times versus detector run number shows the peaks are due to the different triggers we ran. Triggers from our TOF system took a little longer to reach our timing units than triggers from our scintillator paddles. This is likely just due to a difference in cable length or logic time for the triggers. This results in the proton entering the detector a little earlier compared to the trigger time for the TOF based triggers than the paddle based ones. I made two sets of timing cuts, shown in Figure 5.5, based on the detector run number so these could be tighter cuts, dependent on the trigger system. For the spatial cuts, I used a file of simulated protons to determine which cells in each plane the protons would pass through. The cell versus plane distributions for all hits in simulation and data are in Figure 5.6. This cut has the potential to drop the occasional hit from a neutron originating from an inelastic scatter, but the benefit from removing more plume hits, which are most prevalent in the upper west quadrant of the detector, far outweighs the downside of missing an occasional hit.

Once the hits have been clustered together, I associate each cluster with a vertex found by projecting the wire chamber (WC) track forward to the front face of the detector. This vertex is used as a seed for tracking algorithms. Hits are grouped together to form tracks that follow the path of the particle out from the vertex [68]. I made additional cuts on the mean time of the hits on the track and the maximum plane (depth into the detector) of the track. The timing cut, shown in Figure 5.7, removes tracks that had out-of-time plume hits grouped into them, and the max plane cut, in Figure 5.8, is beyond where the maximum energy proton could reach, thus removing long tracks also due to beam plume particles. Any event for which a reconstructed track does not exist is removed. There are a number of reasons a track will not be reconstructed, the primary one being if there are fewer than 10 hits on the track. A final cut on the total number of hits in the clusters in the event is applied to remove noisier events that are more likely to have plume contamination. Following these cuts, 1260 protons remain. Calorimetric energy and track length distributions of the final selected sample are in Figure 5.10. A breakdown of how many protons came from each

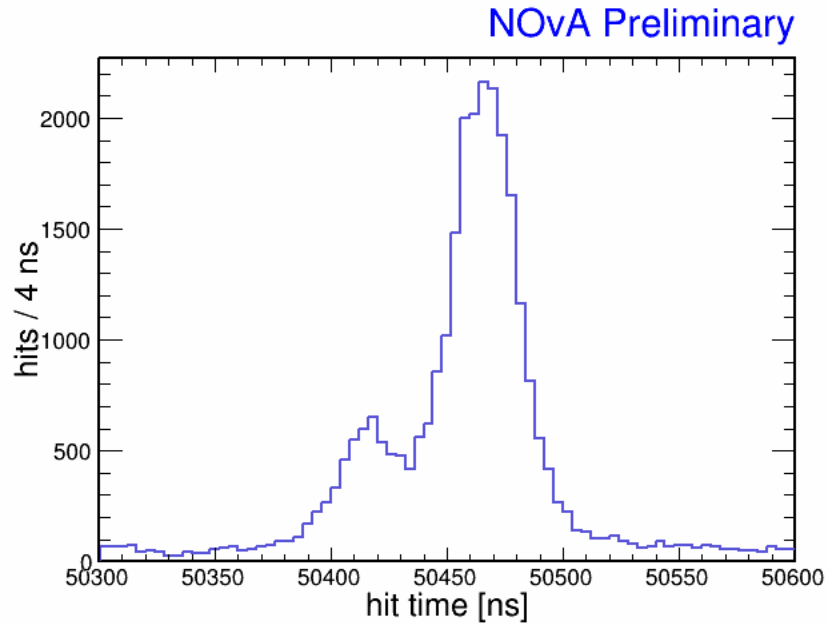


Figure 5.4: Time in ns of hits within each event, zoomed in on the window around the particle the beamline triggered on. The earlier peak is from TOF based triggers and the later peak is from scintillator paddle based triggers.

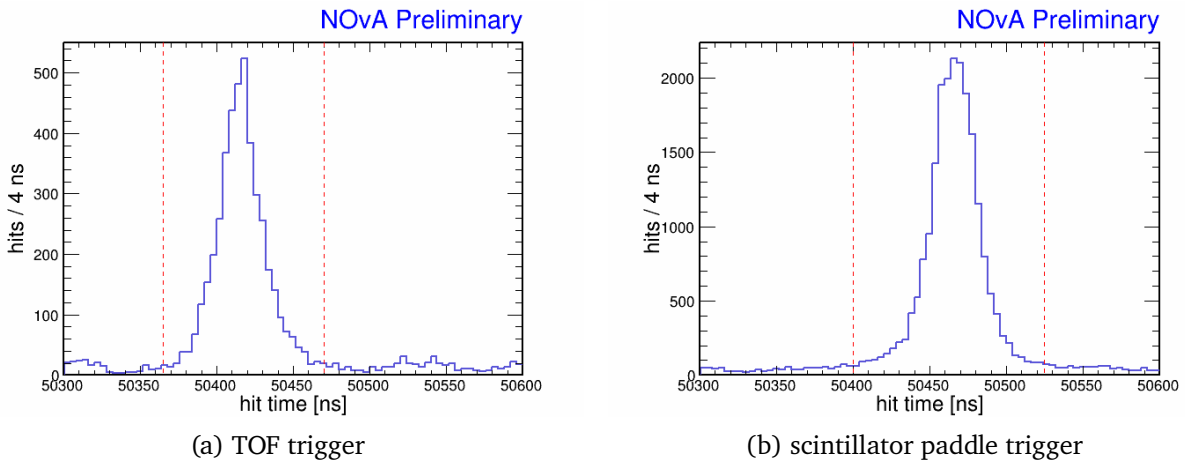


Figure 5.5: Time in ns of hits within each event for TOF (left) and scintillator paddle (right) based triggers. Hits outside of the red lines are dropped prior to the clustering stage.

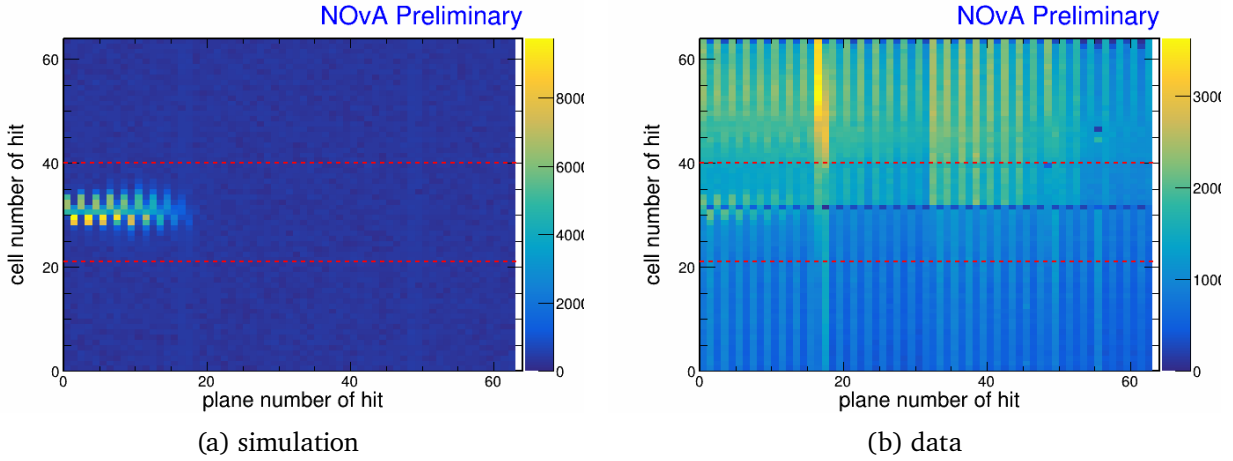


Figure 5.6: Cell and plane location for each hit in the detector for simulated (left) and data (right) protons. Hits outside of the red lines are dropped prior to the clustering stage. The plane to plane offsets are due to the beam spot being centered in vertical (even) planes and just low of center in horizontal (odd) planes.

trigger type is in Table 5.6.

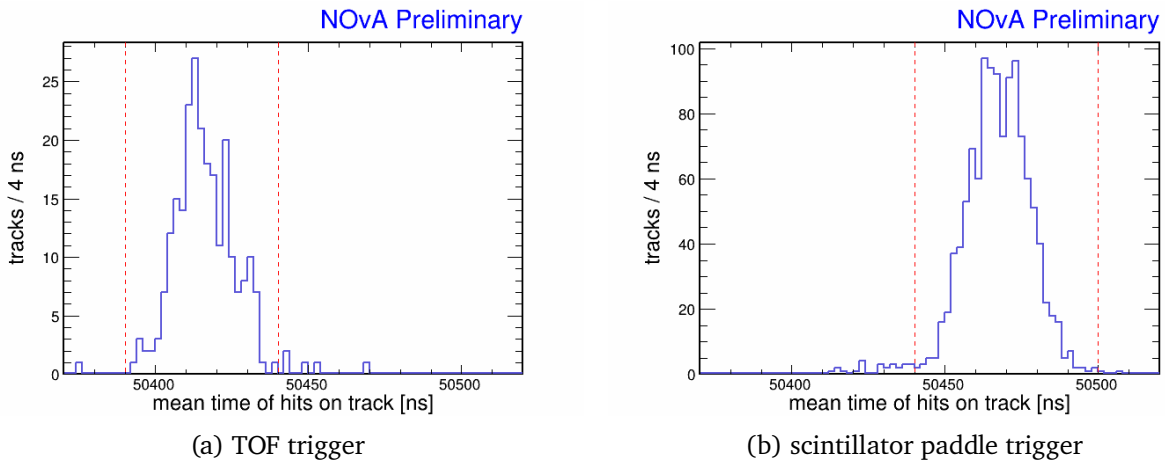


Figure 5.7: Mean time of hits on the track. As with the time of individual hits, this cut is split by trigger conditions to account for the slightly different timing of TOF vs scintillator paddle based triggers. Tracks outside of the red lines are rejected.

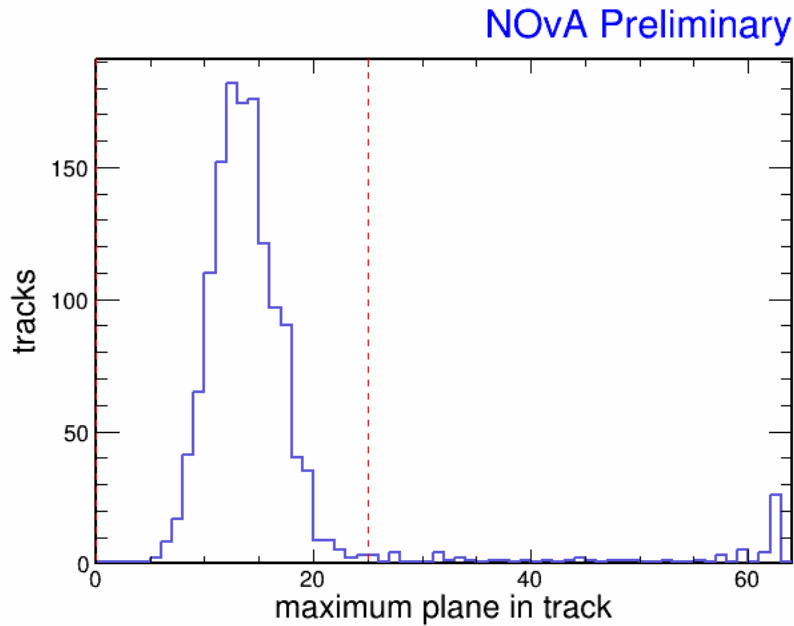


Figure 5.8: Maximum plane the track reaches. Longer tracks are caused by plume particles and are rejected.

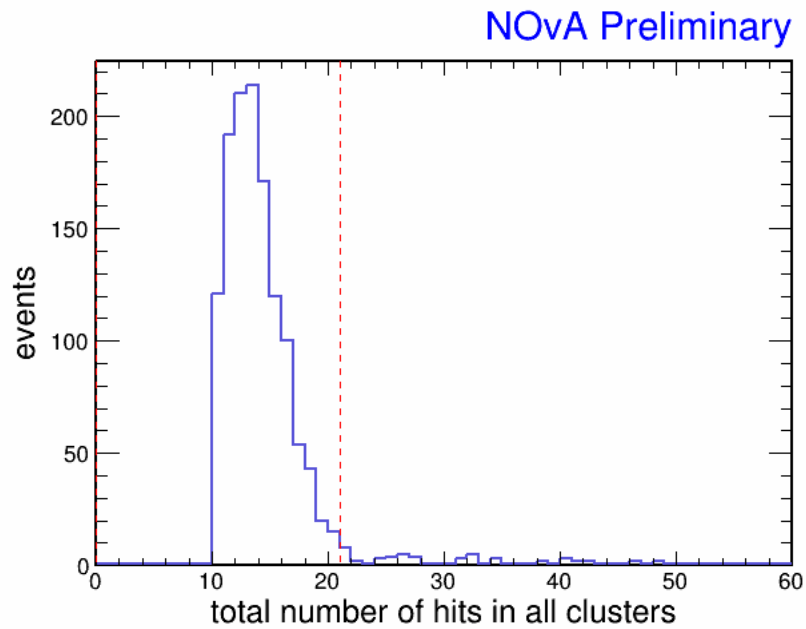


Figure 5.9: The sum of hits in all clusters in the event. Noisier events are more likely to have plume contamination and are rejected.

	hit time [ns]	cell
TOF Trigger	$50365 < t < 50470$	$20 < \text{cell} < 40$
Paddle Trigger	$50400 < t < 50525$	

Table 5.4: Cuts applied to hits in the NOvA detector prior to clustering.

	track mean time [ns]	maximum plane	hits in event
TOF Trigger	$50390 < t < 50440$	25	< 21
Paddle Trigger	$50440 < t < 50500$		

Table 5.5: Cuts applied at the track and event level in the NOvA detector.

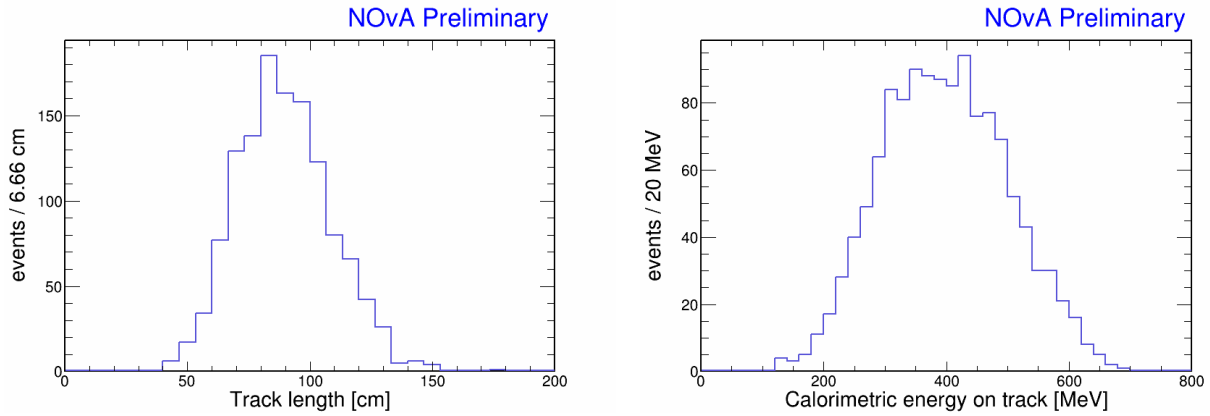


Figure 5.10: Distributions of the final selected sample of protons. Length of the proton track in the NOvA detector is on the left and calorimetric energy of the track is on the right.

time of flight (TOF DS,US and TOFPrompt)	213
3 of 4 scintillator paddle	142
4 of 4 scintillator paddle	735
scintillator paddle 2 & 3, scintillator paddle 3 & 4	170

Table 5.6: Number of protons that came from each trigger type.

Chapter 6

Simulation

Now that we have a sample of protons to analyze, we need simulation to compare them to. First, we need to adjust some parameters in the simulation that differ for each detector such as individual channel thresholds and the relative brightness of each cell in the detector. I will discuss some of the work I did to set some of these parameters and then describe how I generated a sample of simulated protons based on the data events I selected and show some comparison plots.

6.1 Cosmic simulation

Cosmic simulation samples for the Near and Far Detectors are generated using the Cosmic-Ray-Shower Library (CRY) [61] generator. We initially used CRY to generate a Monte Carlo (MC) sample for Test Beam as well, but the generation is inefficient, leading to many empty, unusable events, and our first sample did not have sufficient statistics to tune the light level parameters (section 6.4). Rather than using up more CPU hours to generate more CRY statistics, I developed a data-driven approach to generating a new cosmic simulation sample. This sample was used for calibration and light level tuning.

The first step is to select cosmic ray events in the data. Our calibration sample for Test Beam

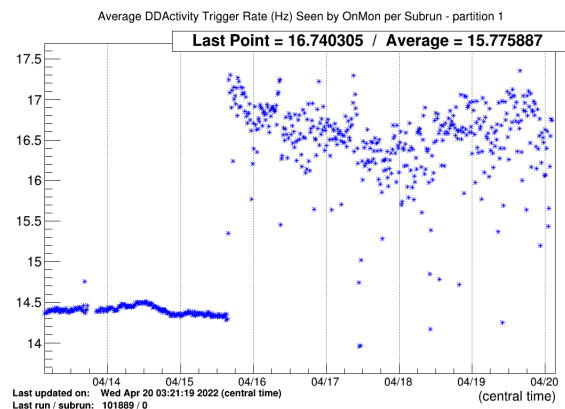


Figure 6.1: Data-driven activity trigger rate for one week in the Test Beam Detector. Beam was off for the beginning of the week, where the rate is flatter around 14.4 Hz.

is recorded using a data-driven activity trigger. The trigger performs some basic clustering on data in the buffer, and if it finds any cluster with at least 10 hits spanning at least 8 planes with at least 3 planes in each view, it sends the DAQ a signal to record the time period containing the cluster. To avoid interfering with the beam readout this trigger is pre-scaled, so we only read out about 14 Hz of activity with beam off, and an average of 20 Hz during periods when the beam is on, see Figure 6.1. Since the activity trigger does not have a beam inhibit, the first step in processing these files is to remove 5 s around each beam spill, using spill timing information from Fermilab’s Intensity Frontier Beam Database (IFDB). During processing, we found some beam spills were not recorded in IFDB, so some beam spills are included in the calibration sample. When using this data to seed the simulation, an angle cut was applied to remove the very horizontal particles coming from the beam.

After removing beam spills from the data sample, a clustering algorithm groups hits together in time and space. A tracking algorithm [69] is run on each cluster, assigning a beginning and end to each group of hits, accounting for possible Coulomb scattering along the track, rather than assuming straight lines. We then run a vertexing algorithm [70] that assigns a vertex pinned to the edge of the detector closest to the start of the track. This vertex and track are used as inputs to an algorithm which reclusters the hits [71] and a tracking algorithm [68] that generates momentum estimates based on the particle’s range in the detector for protons, pions, and muons. Using the muon assumption, the momentum of muons that stop in the detector can be extracted, along with the start location for each track. To remove very horizontal tracks coming from beam spills that were not in the database, I applied a direction cut requiring $|\text{dir}Z| < 0.98$, where $\text{dir}Z$ is the z-component of the particle’s direction unit vector.

For each stopping muon in data, I generated 20 simulated events, smearing the momentum by 2%, the start location by a cell width (4 cm) in x and y, and by about a cell depth (6 cm) in z. The direction is varied with the azimuthal angle around the particle’s original direction varied uniformly and the polar angle, measured from the particle’s original direction, smeared by 4 mrad. The resulting vertex, or start location, and momentum vector combinations are used to generate a file in the HEPEVT format, which is then used as input to our detector simulation. Each event is assigned as μ^+ or μ^- to match the expected ratio of $\mu^+/\mu^- \approx 1.1$ for the energy of muons that would stop in our detector (see Figure 6.2).

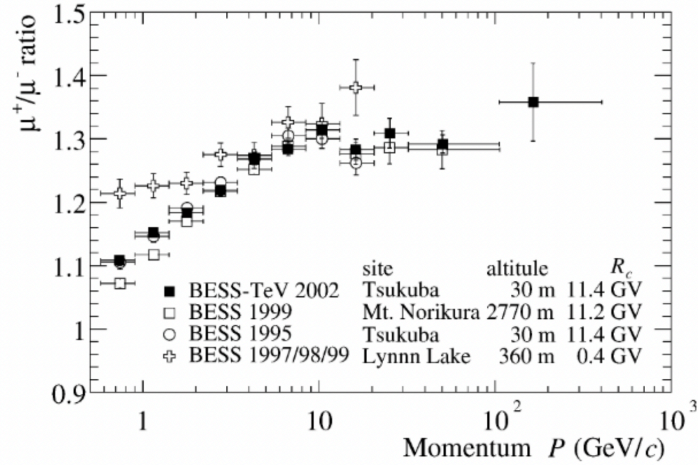


Figure 6.2: From [72], μ^+/μ^- ratio as a function of muon momentum measured by BESS. Muons that stop in the Test Beam Detector have momentum < 1 GeV/c.

After reading in the events, NOvA's simulation passes information about the particles' type and momentum vectors to Geant4 [58], which tracks the particles through the detector geometry, using information about the various materials the particle passes through to simulate interactions in the detector.

6.2 Threshold and Baseline Distributions

The readout simulation, which models how the detector electronics respond to charge from the APDs, assigns a baseline level for each cell by pulling from a gaussian distribution with a configurable mean and sigma. The threshold for each cell is pulled randomly from a file with a distribution of thresholds in it. I used data from pedestal scans of the Test Beam Detector to create threshold files for the two FEB types (v4 and v5) and find the baseline mean and sigma for each. Threshold distributions are in Figure 6.3 and baseline distributions are in Figure 6.4.

6.3 Brightness Levels

As mentioned in subsection 3.3.3, each cell has a slightly different response to light depositions dependent on fiber, scintillator, and electronics differences. While there are cell-to-cell variations within each plane, the most obvious differences for Test Beam Detector cells are from the different types of scintillator in the detector. The first 32 planes (the first block) of the detector were filled

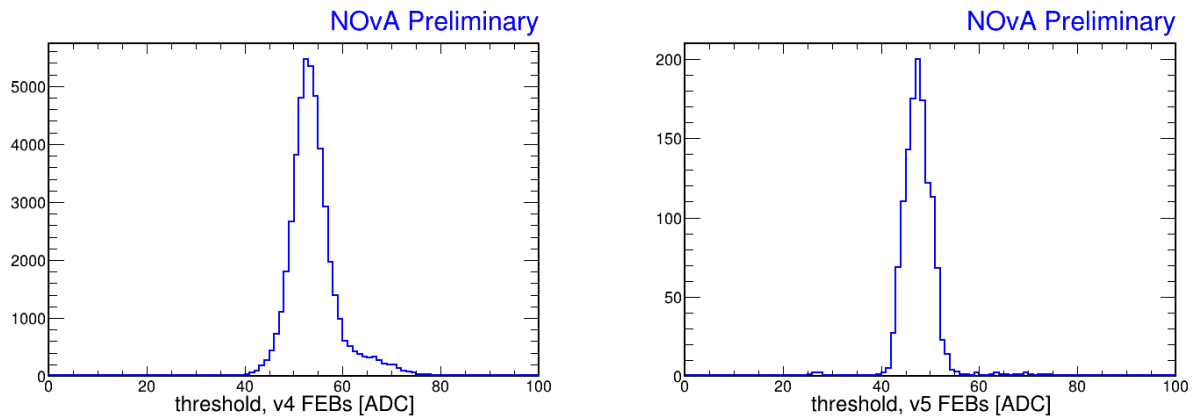


Figure 6.3: Threshold distributions for v4 (left) and v5 (right) FEBS on the Test Beam Detector from pedestal scans taken during period 3.

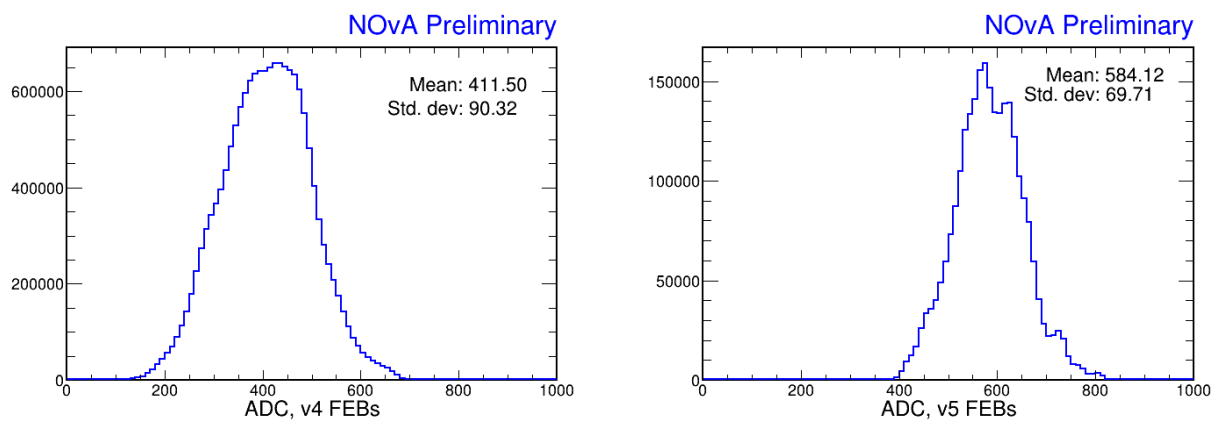


Figure 6.4: Baseline distributions for v4 (left) and v5 (right) FEBS on the Test Beam Detector from pedestal scans taken during period 3.

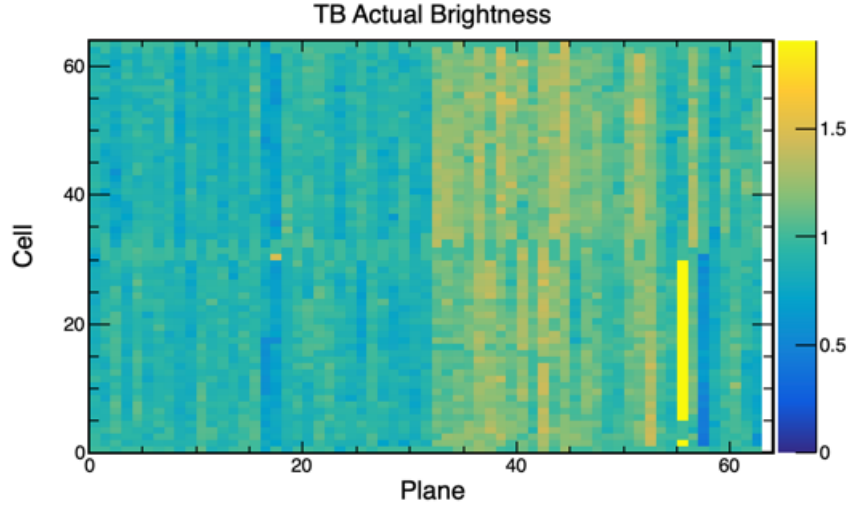


Figure 6.5: Relative brightness of each cell in the Test Beam Detector. There is a distinct increase of brightness between the first 32 planes and the next 21, where the scintillator from Ash River was used. The brightness decreases slightly in the last 10 planes. The very bright region in plane 55 is from a single noisy FEB.

with scintillator from a tanker stored onsite at Fermilab . This scintillator originated from NOvA's prototype near detector. Scintillator from totes that had been stored at Ash River after filling the Far Detector were used for the next 21 planes (the first 2/3 of the second block). The remaining 10 planes of the detector (the last 1/3 of the second block) were filled with scintillator that had been stored in drums at the University of Texas - Austin. We use the response at the center of each cell from the relative attenuation calibration to model the relative brightness of each cell in the detector. The resulting brightness map of the detector is in Figure 6.5.

6.4 Light Level View Factors

Our light model accounts for both scintillation and Cherenkov light. The main part of light level tuning entails adjusting the number of scintillation and Cherenkov photons so their sum matches the data by fitting for the parameters in

$$N_\gamma = F_{x,y}(Y_s E_{\text{Birks}} + \epsilon_C C_\gamma) \quad (6.1)$$

where N_γ is the total number of photons seen, $F_{x,y}$ are the view factors described below, Y_s is the scintillation light yield (photons/MeV), E_{Birks} is the total energy deposited from scintillation light

(using Birks' law [73]), ϵ_C is the efficiency of the scintillator absorbing and reemitting Cherenkov light, and C_γ is the number of photons from Cherenkov radiation. Most of the parameters involved in the simulation of light in the detector are the same across detectors. When simulating the expected amount of light in each cell, a scale factor is applied separately for the horizontal and vertical planes in the detector. Cosmic ray muons tend to be downward-going and enter at the top of the detector. As a result, their path length through vertical cells is longer on average and they deposit more total charge in them. Since the detectors vary in location (above or underground) and size, we set the view factors, $F_{x,y}$, independently for each detector. F_x (F_y) is for the vertical (horizontal) planes. Y_s and ϵ_C are properties of the scintillator, so I used the same values for these that had been previously found using Near and Far Detector data. An interesting future study would be to tune these separately on the different regions of scintillator in the Test Beam Detector to see if these parameters vary significantly. The use of the brightness map described in section 6.3 already accounts for light yield differences between scintillators.

I tuned the view factors using cosmic simulation generated as described in section 6.1. For my initial sample, I used the values from the latest tuning performed for the Near Detector with $F_x = 0.5078$ and $F_y = 0.4927$. The tuning procedure [74] selects muons that stop in the detector. Each hit on a muon track is placed into a bin of its distance to the end of the muon track, see Figure 6.8. Fitting for $F_{x,y}$ results in $F_x = 0.4791$ and $F_y = 0.4473$. A combined plot of pe/cm for all muon hits with the old and new view factors is in Figure 6.9.

6.5 Simulating Beamline Events

Following tuning of the simulation, I used the beamline information for each proton selected in chapter 5 to generate a simulation sample. For each event, I use the momentum and direction from the wire chamber (WC) track to seed the simulation. Each track was started just downstream of WC 4, 445 cm upstream of the NOvA detector, with the position in the XY plane determined by projecting the track to the $z=-445$ cm plane. I added all the beamline material downstream of WC 4 to the detector geometry file so the simulated protons would pass through the same material as the data ones would following the measurement of their momentum. Immediately downstream of WC 4 is a Helium pipe with mylar windows. Following that is the Cherenkov detector with vinyl and

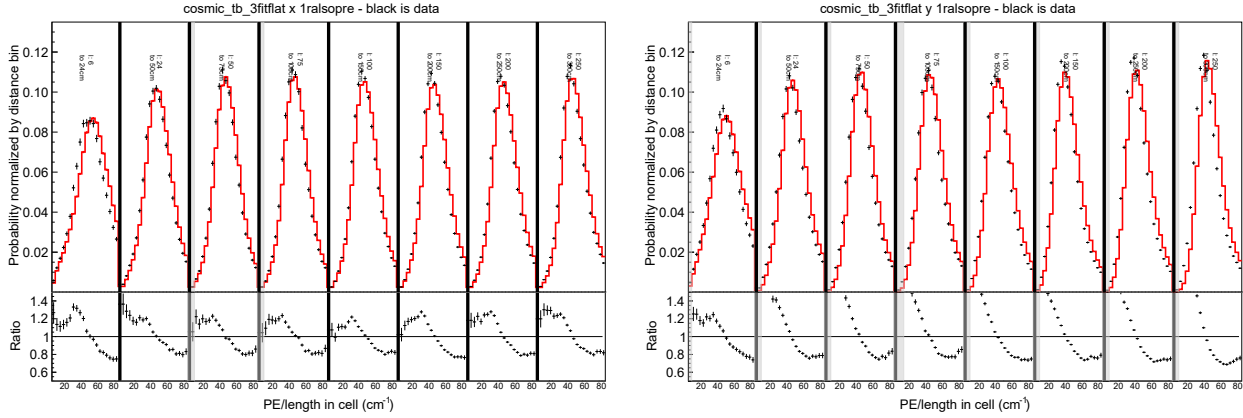


Figure 6.6: x-view, vertical planes

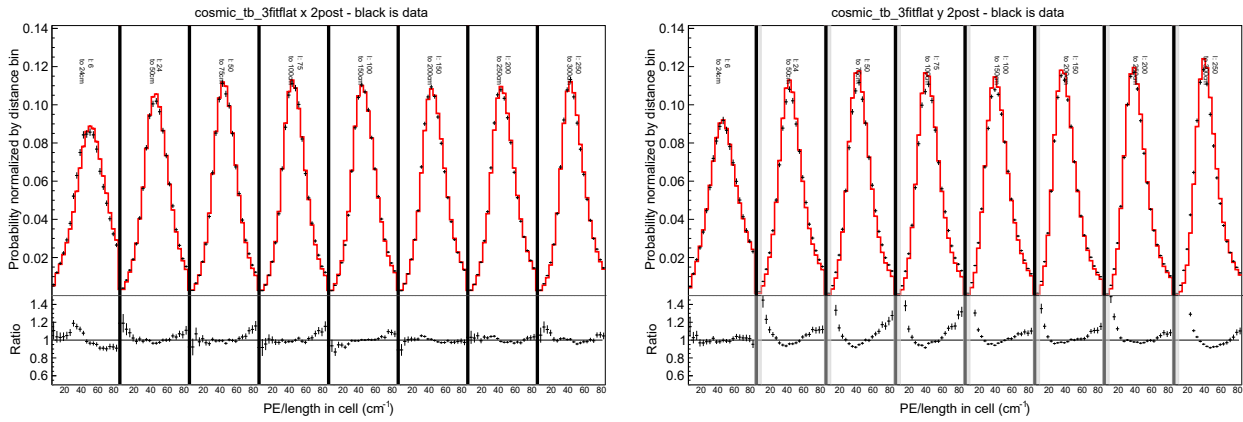


Figure 6.7: y-view, horizontal planes

Figure 6.8: pe/cm of muon hits in vertical (left) and horizontal (right) cells split up by bins of distance to the end of the muon track. Data points are in black, the red line is simulation before (top) and after (bottom) fitting for $F_{x,y}$.

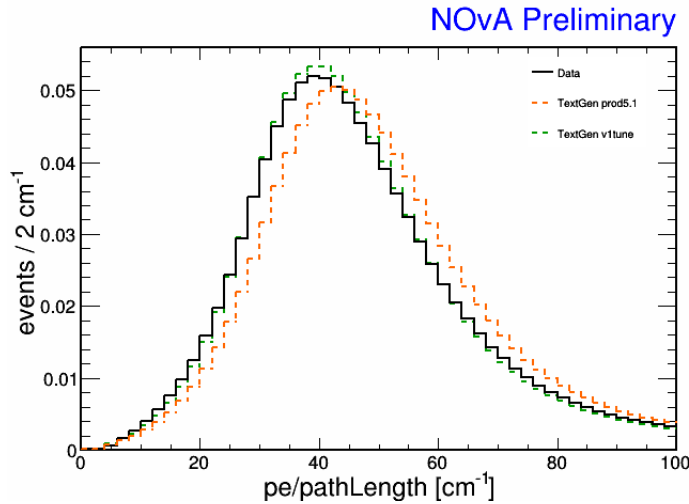


Figure 6.9: pe/cm for all muon hits in data (black), simulation before tuning (orange) with $F_x = 0.5078$ and $F_y = 0.4927$, and simulation after tuning (green) with $F_x = 0.4791$ and $F_y = 0.4473$.

tedlar windows on either end. The mylar mirror inside the Cherenkov detector was not simulated due to issues with it overlapping the CO₂ volume in the gdml, but it only accounts for $1.3 \times 10^{-4} X_0$. The two downstream time of flight detectors are between the Cherenkov detector and the NOvA detector. For each of the beamline devices listed, I simulated the correct length in z, and inflated their sizes in the xy plane by about 100% to account for any potential uncertainty in the placement of the material relative to the z-axis of the NOvA detector, see Figure 6.10.

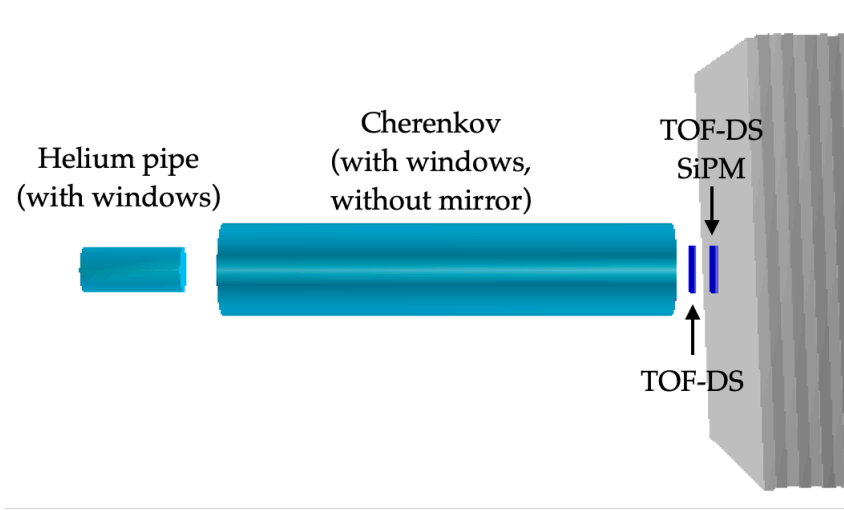


Figure 6.10: Diagram of beamline material between the fourth wire chamber and the NOvA detector. The grey block on the right is the NOvA detector. Sizes of beamline detector are inflated in the XY plane to ensure simulated particles will pass through them even if they are misaligned in the geometry.

Reconstruction and selection of simulated events is done the same as it is for data as much as possible. We have no simulated information for the beamline detectors so the beamline cuts in Table 5.1 and Table 5.3 are not applied to simulation. At the clustering stage, any hits outside of the central region of the detector are dropped, just like in data. The timing cut applied to simulation at this stage keeps all the hits, but the spatial cut does remove some simulated noise hits. As an analog to using the wire chamber vertex to seed tracking algorithms, I used the true vertex of the proton, where the proton intersects with the front face of the NOvA detector, as a seed. A cut on the mean time of hits in simulated proton tracks keeps all events with a reconstructed track. Cuts on the maximum plane in the track and total number of hits in all clusters in the event are the same as for data. Comparisons of the maximum plane in the track and total number of hits are in Figure 6.12 and Figure 6.13. To ensure each data event is equally represented in the simulation, I generated

events until I had exactly 20 simulated events that passed all the selection cuts. In total, I had 1260 selected data events and 25200 simulated protons.

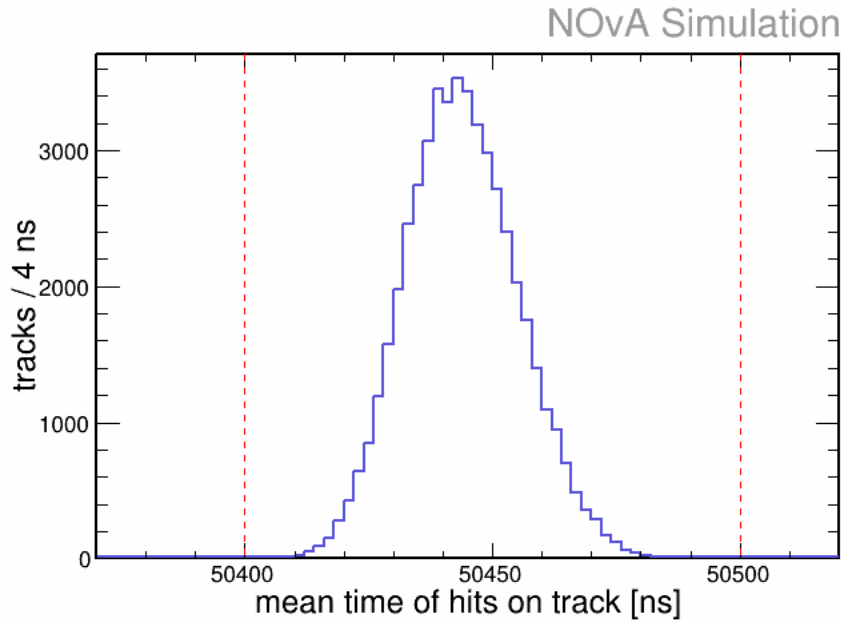


Figure 6.11: Mean time of hits on the track for simulation. Tracks outside of the red lines are rejected.

		hit time [ns]	cell
Data	TOF Trigger	$50365 < t < 50470$	
	Paddle Trigger	$50400 < t < 50525$	$20 < \text{cell} < 40$
Simulation		$50300 < t < 50600$	

Table 6.1: Cuts applied to hits prior to clustering.

		track mean time [ns]	maximum plane	hits in event
Data	TOF Trigger	$50390 < t < 50440$		
	Paddle Trigger	$50440 < t < 50500$	25	< 21
Simulation		$50400 < t < 50500$		

Table 6.2: Cuts applied at the track and event level.

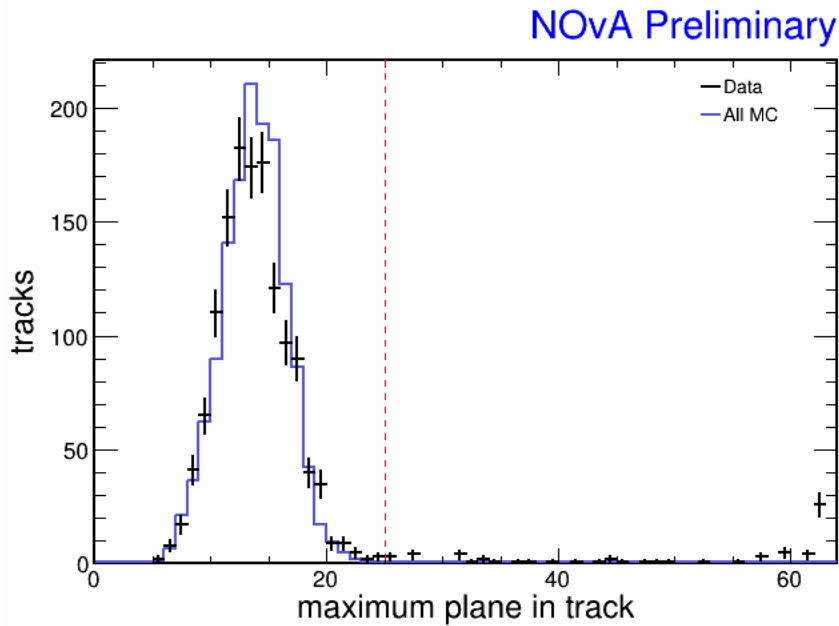


Figure 6.12: Maximum plane the track reaches. Longer tracks are caused by plume particles and are rejected. Simulation is area normalized to data. Tracks in data are about a plane shorter on average than tracks in simulation. The cause for this is unknown.

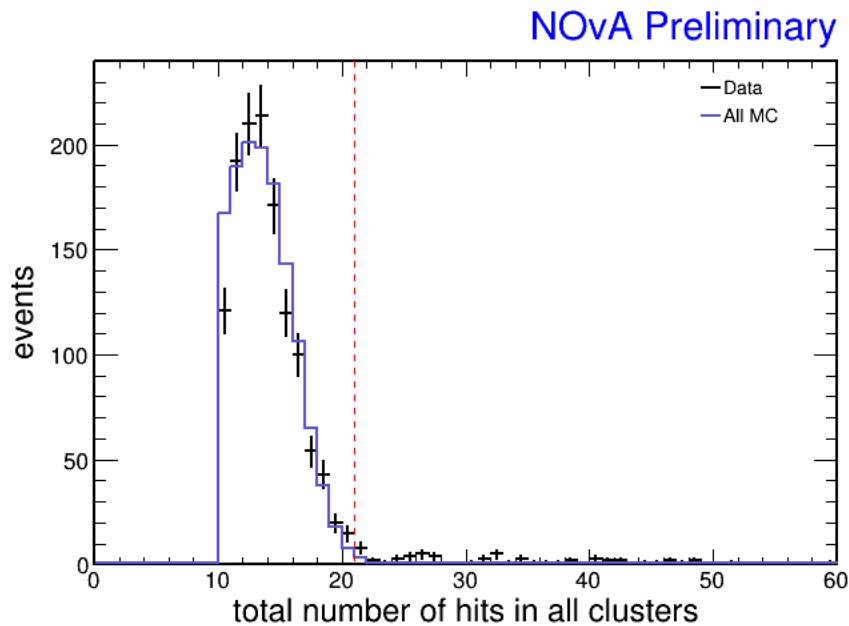


Figure 6.13: The sum of hits in all clusters in the event. Noisier events are more likely to have plume contamination and are rejected. Simulation is area normalized to data.

Chapter 7

Nuclear Interaction Length

7.1 Proton interactions

When protons interact with matter, there are a few different processes that can occur. In the simplest case, a proton will pass through matter depositing energy lost through ionization until it ranges out, depositing its final kinetic energy in a Bragg peak at the end of the track. There are also a few scattering processes that can occur. The protons can elastically scatter off nuclei, slightly changing their trajectory while continuing to range out. They can also inelastically scatter, resulting in a greater energy loss and higher transverse momentum. The parameter that determines how likely a proton is to inelastically scatter is the nuclear interaction length, λ_i . To determine λ_i for the NOvA detector, I approximated the detector as a ‘soup’ consisting of the correct mass fractions of each of its components. Then I calculated λ_i using the interaction length for each element in the soup, weighted by its mass fraction. Interaction lengths were taken from the PDG [75] summary tables. They are based on the Glauber model [76], calculated for 200 GeV/ c neutrons. For the NOvA detectors, $\lambda_i = 86.6$ cm.

I also attempted to calculate the interaction length for 1 GeV/ c protons using available data from [77]. Since 1 GeV inelastic cross section data was only available for carbon and oxygen, I used the middle panel of Fig. 8 from the paper (copied to Figure 7.1) to obtain the relationship between atomic weight and cross section. Fitting a power law to the inelastic cross section line gives

$$\sigma_{in} [\text{mb}] = 40.4A^{0.701} \quad (7.1)$$

where A is the atomic weight. From the cross section, the interaction length for each element can be found with

$$\lambda_i = \frac{A}{N_A \sigma} [\text{g/cm}^2] \quad (7.2)$$

where N_A is Avogadro’s number. Using the same ‘soup’ method to calculate λ_i for the detector as a whole gives $\lambda_i = 83.7$ cm, which is fairly close to the PDG-calculated value of 86.6 cm. I will use

the PDG value for the rest of this chapter, assuming a 5% error, which encapsulates my calculated value for 1 GeV/c protons.

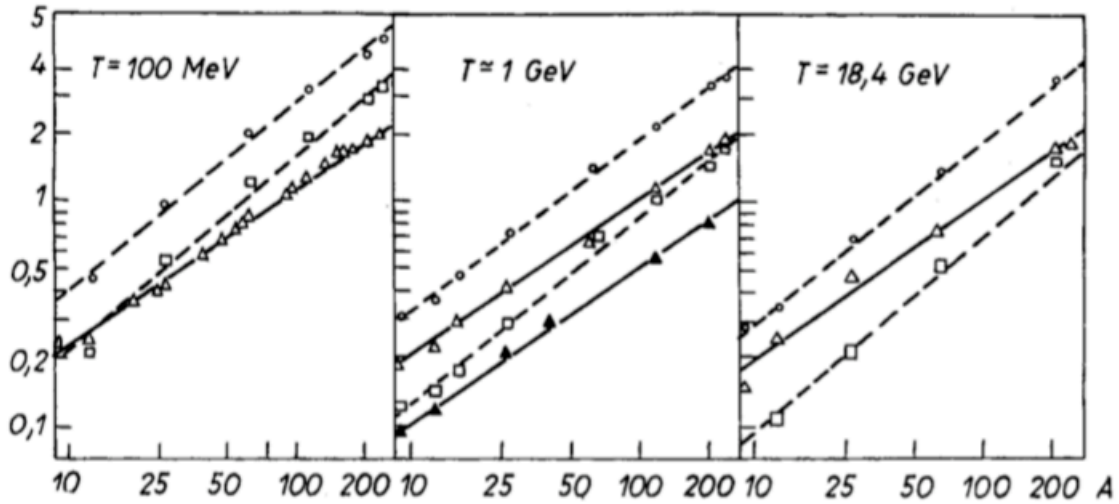


Figure 7.1: From [77], nucleon-nucleus cross sections (y-axis, in barns) as a function of mass number A (x-axis). The middle panel is for 1 GeV particles, with the open triangles for the inelastic cross section.

One question the proton sample from the NOvA Test Beam Detector can help to answer is if we correctly simulate the fraction of protons that have an inelastic scattering interaction versus ranging out. To reconstruct the neutrino energy for each event in our detectors, we handle the lepton and hadronic system separately. For ν_μ events, we use the range of the muon to determine its energy, and then add the calorimetric energy of the hadronic system, accounting for energy loss in the dead material of the detector. For ν_e events, we use calorimetric energy for both the electromagnetic (EM) shower from the electron and the hadronic system, but scale the two separately to account for the different detector response for EM versus hadronic energy. If protons inelastically scatter at different rates in our simulation and data, the correction applied to the hadronic system could be inaccurate, since events with inelastic scattering will deposit less visible energy in the detector. This is particularly important for quasielastic ν_μ events, which have the lowest hadronic energy resolution, and therefore give us our best measurements of Δm_{32}^2 and θ_{23} .

As GEANT propagates protons through matter, it checks the cross section for various processes at each step to determine if a given process should occur. For protons below 91 GeV, GEANT uses the Barashenkov intranuclear cascade model for the inelastic scattering cross section. [58, 78] The cross

section for protons scattering off of carbon is shown in Figure 7.2. The solid line is the Barashenkov cross section used for the proton energies in the NOvA Test Beam detector.

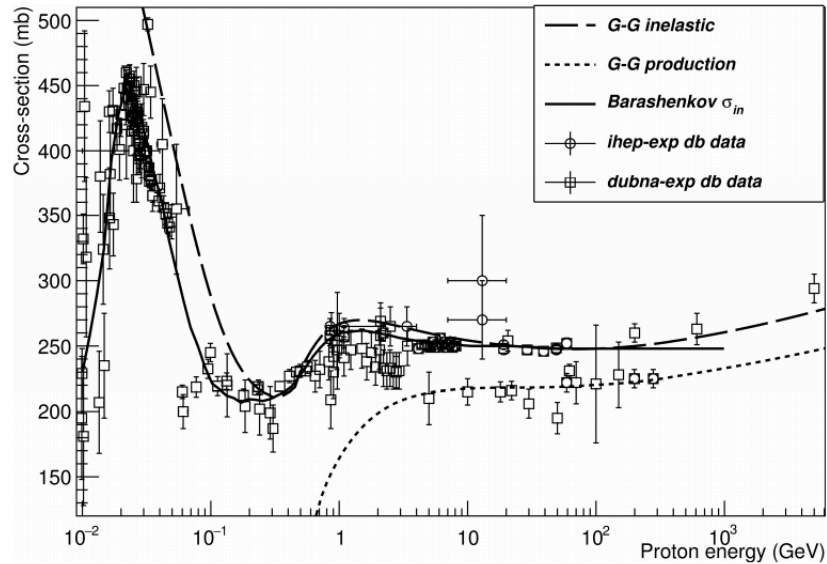


Figure 7.2: From [58], inelastic and production cross sections of protons on a carbon target. For the energies in NOvA Test Beam, GEANT uses the Barashenkov (solid line) interpolations. The NOvA detectors are 67% carbon by mass.

For each simulated proton event in Test Beam, I checked the GEANT process code for every immediate daughter of the proton to determine what process create the daughter(s). The GEANT codes are summarized in Table 7.1. 44.6% of the simulated events had an inelastic scatter, 35.1% had an elastic scatter, and 29.6% ranged out without creating any daughter particles. I separated the simulation sample into two populations: any events with daughter particles of the proton resulting from the ‘protonInelastic’ GEANT process code were placed in the inelastic scatter population, while the remaining events were placed in the range out population.

7.2 Data Selection and Simulation

Protons were selected as described in chapter 5. The selection was designed to minimize the beam plume contamination. The high-rate environment the NOvA Test Beam experiment was in can lead to other particles passing through the detector coincident in space and/or time with the particle that caused the Beamline to trigger. If hits from a muon in the beam plume get clustered together with the hits from the selected proton, the reconstructed track could have the incorrect direction

GEANT process code(s) for daughter particle(s)	Number of events	$\langle \text{reco } p_T \rangle$ [MeV/c]
No daughters	7468	3.3
protonInelastic	8878	14.5
hadElastic	6474	9.3
CoulombScat	11	9.3
hadElastic & protonInelastic	2365	13.1
CoulombScat & protonInelastic	5	10.8
CoulombScat & hadElastic	2	33.0

Table 7.1: GEANT process codes and average reconstructed transverse momentum, $\langle \text{reco } p_T \rangle$, for immediate daughter particles of simulated protons. Example event displays of protons with no daughters, inelastic scattering, and elastic scattering are in Figures 7.3-7.5.

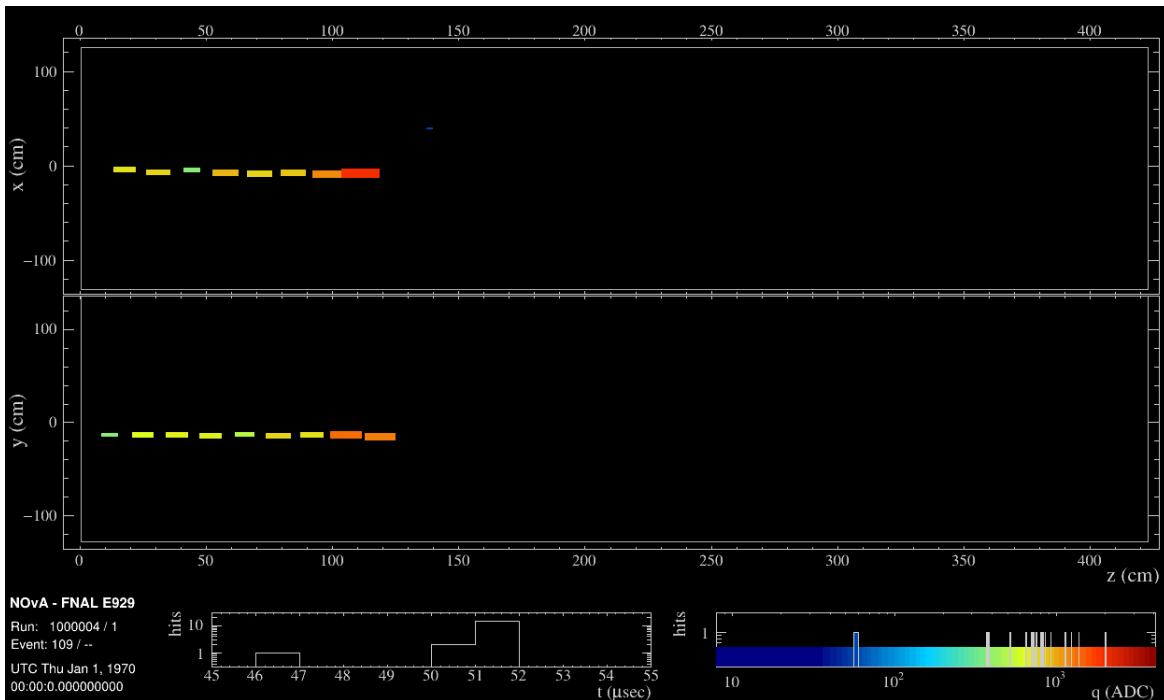


Figure 7.3: Simulated proton that ranged out without creating any daughter particles.

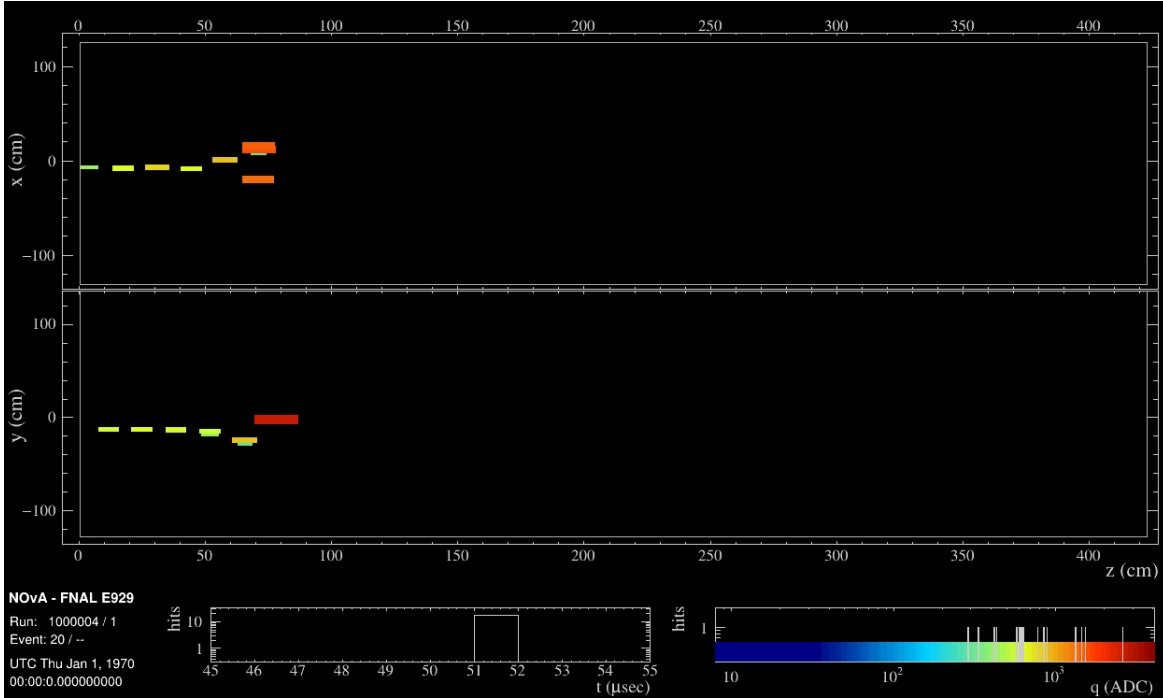


Figure 7.4: Simulated proton with a daughter particle created by the *protonInelastic* GEANT process code, indicative of an inelastic scatter.

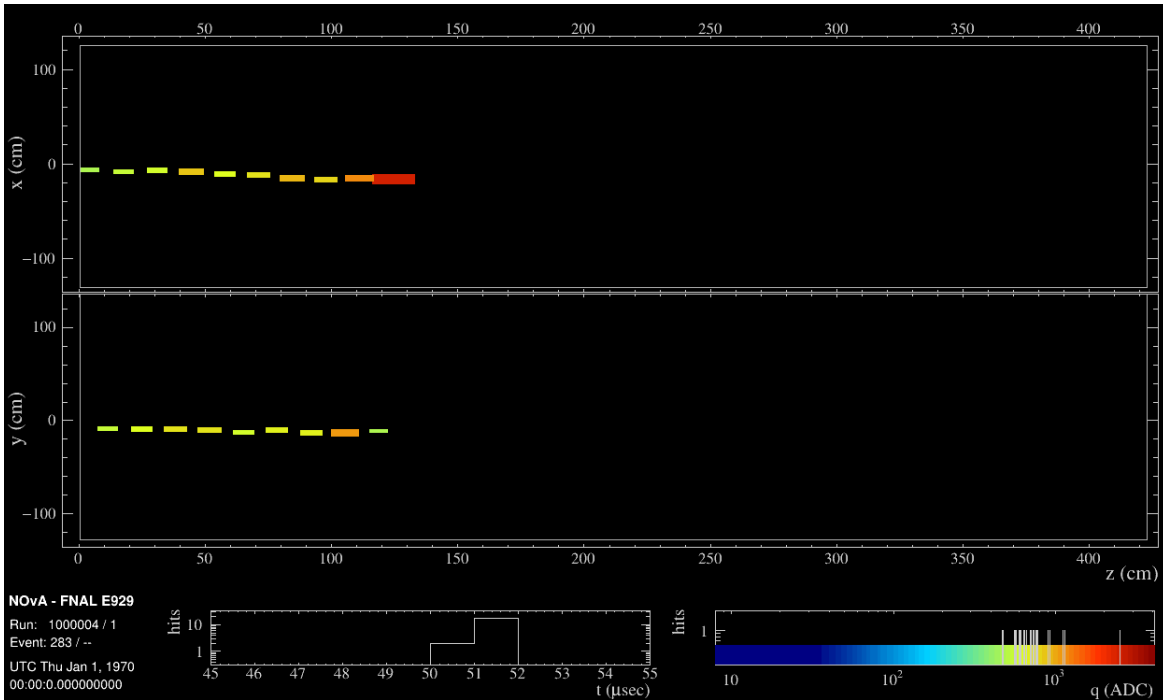


Figure 7.5: Simulated proton with a daughter particle created by the *hadElastic* GEANT process code, indicative of an elastic scatter. Events with elastic scattering have a similar topology to ones that range out with no scattering.

or length, both leading to inaccurate reconstructed quantities. Tight timing and spatial cuts on the individual hits at the clustering stage remove a majority of the hits originating from beam plume particles, but cannot remove all of them. When selecting protons for this analysis, I introduced a cut on the total number of hits in the event after the clustering stage to further remove busier events that have a high likelihood of plume contamination.

Following data selection, the simulated sample was created as described in section 6.5. For each data proton, there are 20 simulated protons that pass the selection cuts. Prior to the fit, the simulation is scaled down by 20 to match the amount of data.

7.3 Fitting in bins of p_T

After looking at a few different variables such as opening angle and track length (see Figure 7.6), the one found to have the most separation between the two MC populations was $\sqrt{p_x^2 + p_y^2}$ which, since the protons have z direction cosines very close to 1, is a good approximation of the reconstructed transverse momentum, p_T . Protons that inelastically scatter have a higher p_T on average than those that range out. Figure 7.7 shows the transverse momentum for simulated protons that had daughters created from only inelastic scattering, only elastic scattering, or no daughters. At low p_T , the inelastic and elastic scattering populations have a similar distribution, but above p_T of about 0.4 GeV/c, the elastic scatters look more like the range out population.

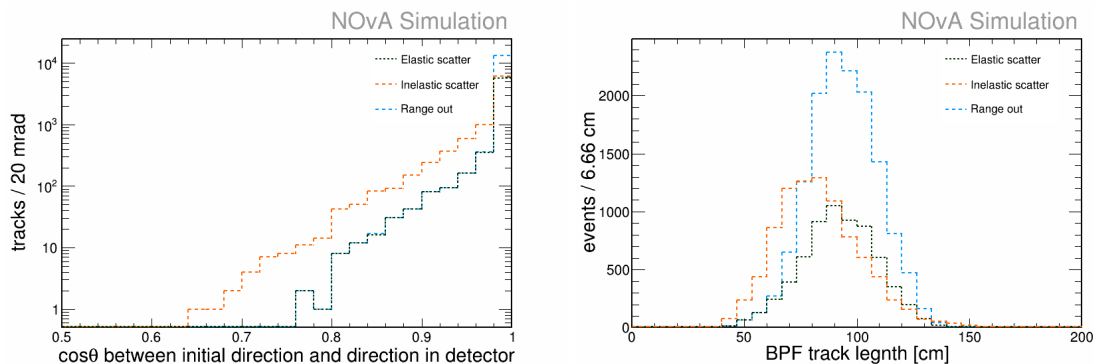


Figure 7.6: Opening angle between initial direction and direction in detector (left) and track length of proton in detector (right). While these variables show some differences between the inelastic scattering and range out populations, they do not have enough separation for a reliable fit.

To determine the relative amount of inelastic scattering in data and simulation, I used the reconstructed p_T distributions of the inelastic scattering and range out simulated populations and fit

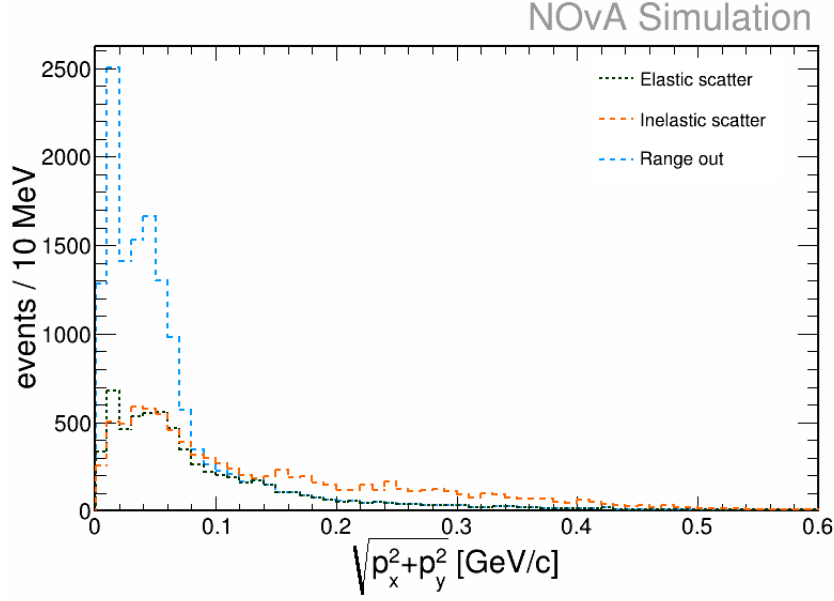


Figure 7.7: Transverse momentum for simulated events that contain an inelastic scatter, elastic scatter, or no scattering.

them to the data in 50 MeV/ c bins of p_T . The function used for the fit was

$$\text{data} = A(f \times \text{MC}_{\text{range}} + (2 - f) \times \text{MC}_{\text{scatter}}) \quad (7.3)$$

where A is an overall normalization factor, f is the scale factor applied to the range out simulation sample, and $\text{MC}_{\{\text{range}, \text{scatter}\}}$ are the simulation samples of protons that range out or have an inelastic scatter. $f = 1$ represents when the data perfectly matches the simulation. The fit was done by optimizing the Poisson log likelihood function

$$-2 \ln \lambda(\theta) = 2 \sum_{i=1}^N \left[\nu_i(\theta) - n_i + n_i \ln \frac{n_i}{\nu_i(\theta)} \right] \quad (7.4)$$

where $\nu_i(\theta)$ is the value of the function from Equation 7.3 for the i^{th} bin, and n_i is the data value for the i^{th} bin. f was initialized at 1.0 (the value it would have if the simulation and data matched perfectly) and allowed to float between 0 and 2.0. A was fixed at 1.0 since the simulation was normalized to the data prior to the fit, though it was allowed to float in a cross check. The result of the fit, shown in Figure 7.9, is $\text{data} = 1.0(0.77 \times \text{MC}_{\text{range}} + (1.23) \times \text{MC}_{\text{scatter}})$.

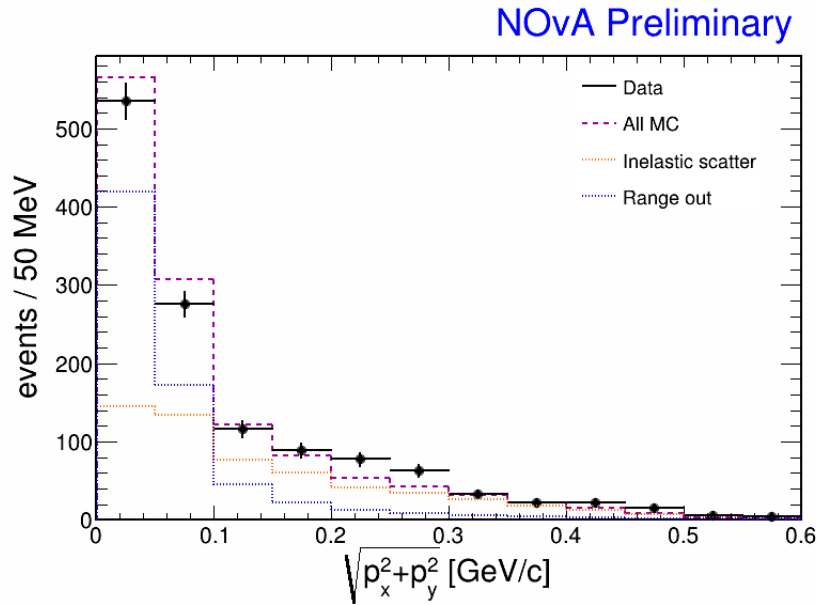


Figure 7.8: Transverse momentum for data and simulation prior to the fit.

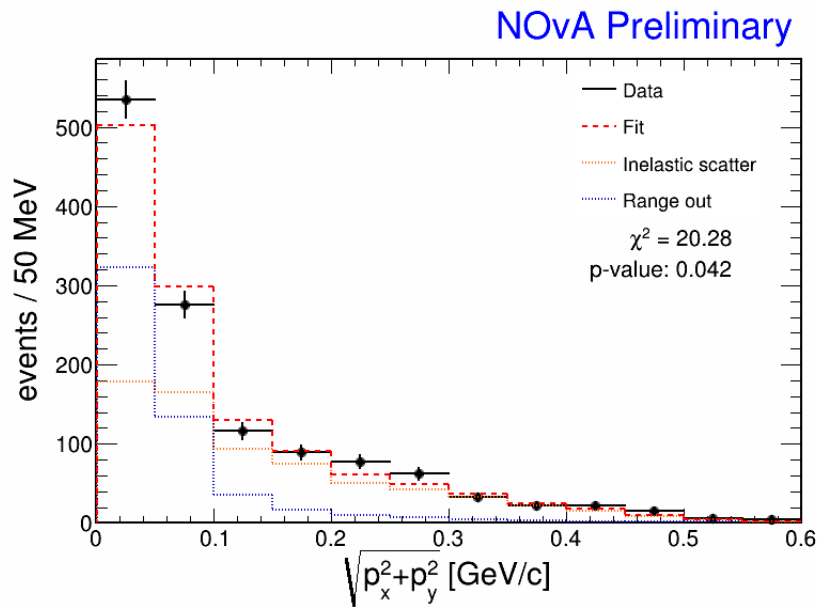


Figure 7.9: Transverse momentum for data and simulation with the fit result. Simulated population for inelastic scatter (range out) was tuned up (down) by the amount indicated by the fit. The red fit line is $1.0(0.77 \times MC_{\text{range}} + (1.23) \times MC_{\text{scatter}})$

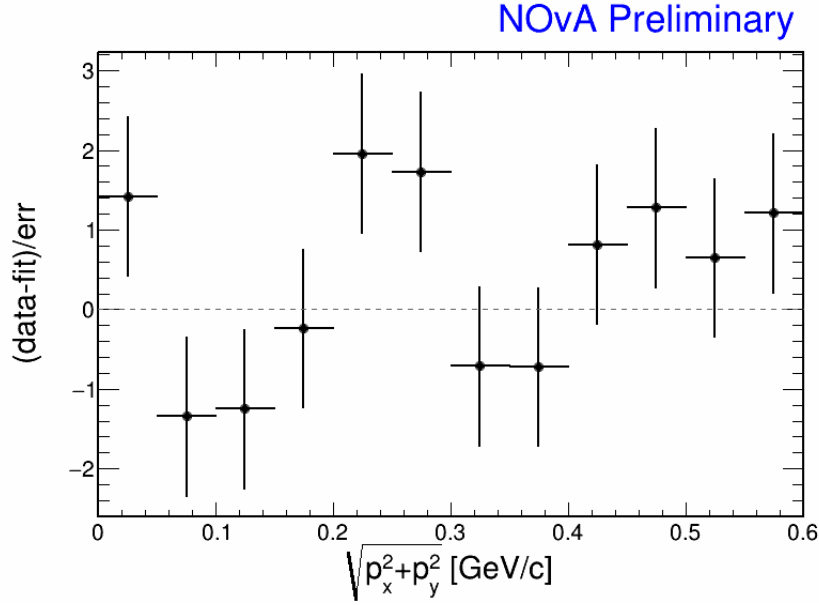


Figure 7.10: Residuals of fit.

7.4 Cross checks

I ran the fit again on a few different subsets of the data and simulation to check if the results varied under different beam and detector conditions. I also made some new simulation samples with different initial directions to assess the effect of uncertainty in detector alignment. Since the simulation sample has exactly 20 times the events of the data sample, I normalized it prior to doing the fit and set the normalization factor in Equation 7.3 to 1.0. As a check, I allowed this factor to float between 0 and 2. The value for A was 1.03 ± 0.040 , and f went down slightly to 0.757 ± 0.086 . χ^2 also went down by one, as expected when removing one degree of freedom.

I split the run period into two regions: the first had primarily TOF-based triggers while the second was primarily the 4-of-4 scintillator paddle trigger. Running the fit on these two regions separately yields similar results to the fit on the full period (see Table 7.2), indicating no dependence on trigger conditions. I also split the sample by secondary beam intensity. We ran most of the period with a beam intensity of $MC6IC = 1 \times 10^9$ protons-per-pulse (ppp), but did some studies at higher intensities while trying to optimize beam conditions. The distribution of intensities for the spills with selected protons is in Figure 7.11. Running the fit separately for intensities less (greater) than 1.55×10^9 ppp yields $f = 0.785 \pm 0.089$ ($f = 0.464 \pm 0.23$). Although the result for the higher intensity fit is much

lower than the lower intensity fit, it is only a 1.3σ difference. I looked at all 107 data events from the high intensity sample in the NOvA event display with the reconstructed track drawn on the event to check if the events with higher intensity had more beam plume contaminating the reconstruction, artificially increasing the p_T of events and thus the fraction of scattering events in the data. Of the 107 events, 3 had their direction increased by an extra hit from the beam plume, like the event shown in Figure 7.12; 1 (shown in Figure 7.13) had the wrong direction in one view likely due to the hit from a neutron kicked out of a nucleus at the end of the track being dropped by the clustering algorithm since it was too far away from the track; but none of the remaining events (example in Figure 7.14) had a reconstructed track affected by hits from the beam plume. Since I did not find any strong evidence of contamination from beam plume, I left the high intensity events in my sample.

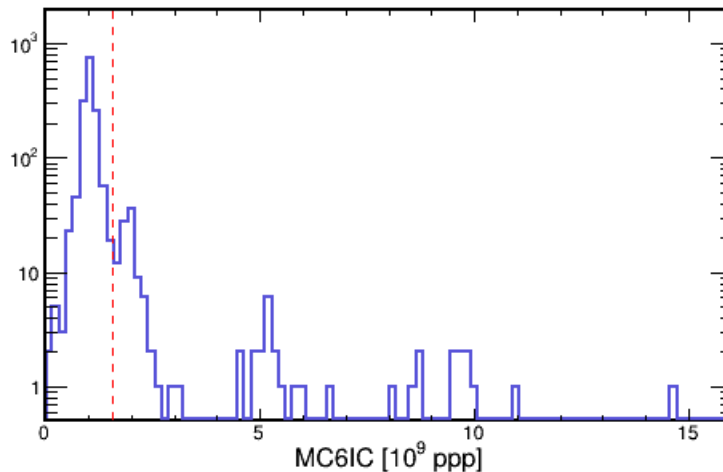


Figure 7.11: Secondary beam intensity for spills with selected protons. The red line is at 1.55×10^9 ppp. Events to the left (right) of this line are in the lower (higher) intensity sample.

While tuning the placement of the detector, I found the adjustments impacted the p_T distribution, shifting events by about 10-20 MeV/ c . This was the driving force behind choosing 50 MeV/ c bins for the fit. In order to evaluate how much of an impact uncertainty in the orientation of the detector has on the fit, I created samples with the initial direction of particles shifted by ± 10 mrad in x and y , and reran the fit on each. The results for each are summarized in Table 7.2. In each case, the value for f went up, as did χ^2 . Although each direction change affected f in the same direction, I have no reason to believe this should be a one-sided effect, so I assumed a symmetric uncertainty of 4%.

I also wanted to quantify how much of an effect any potential plume contamination would have

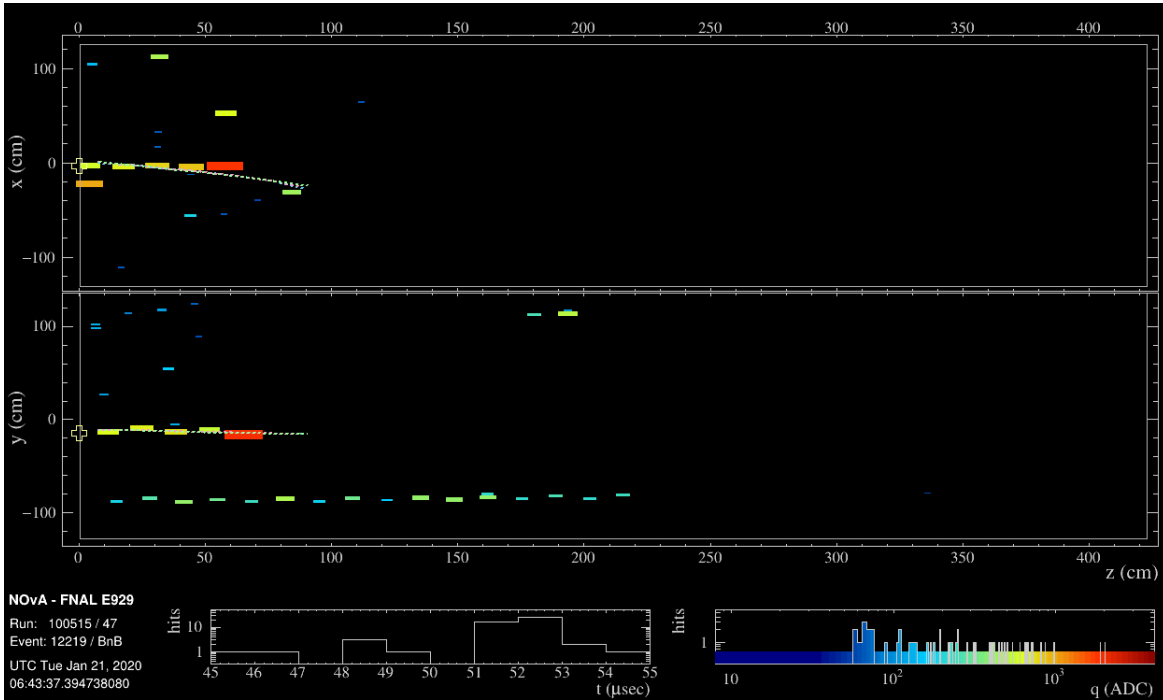


Figure 7.12: Misreconstructed track due to extra hit from beam plume. There were 3 higher intensity events that looked like this.

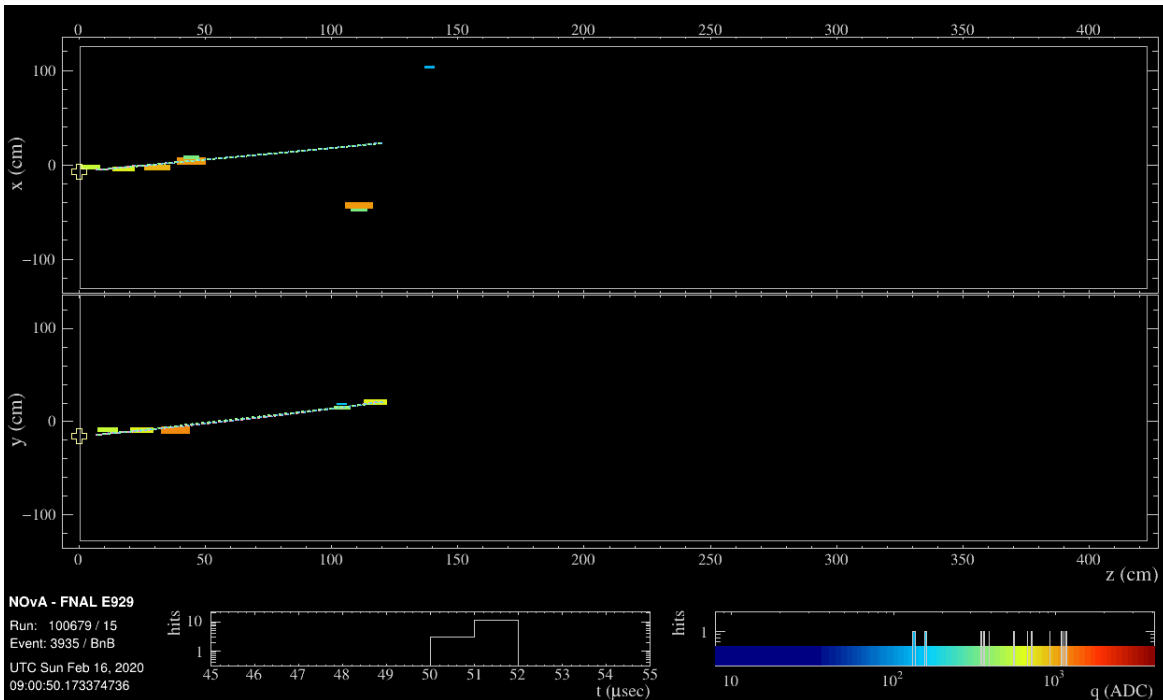


Figure 7.13: Track with the wrong direction in the x-view. The extra hits around $z=110$ are likely due to a neutron kicked out from an interaction at the end of the proton track. One hit in the x-view was missed due to the spatial cuts in the clustering algorithm. This was the only high intensity event with this problem.

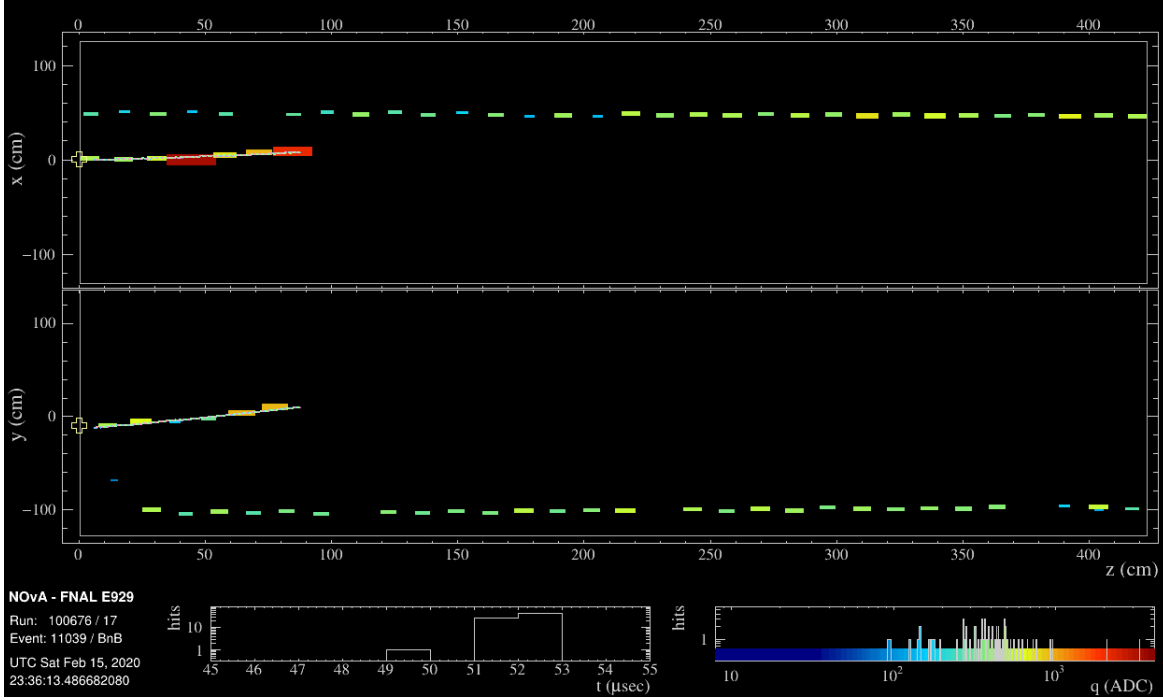


Figure 7.14: An example of an event from a high intensity spill with good reconstruction. The majority of high intensity events fell into this category. The other hits in the event are likely from a muon in the beam plume.

		Number of data events	A	f	χ^2	p-value
	Nominal	1260	fixed at 1.0	0.771 ± 0.085	20.3	0.042
	Allow A to float	1260	1.03 ± 0.040	0.757 ± 0.086	19.4	0.035
Run	TOF trigger	213	fixed at 1.0	0.870 ± 0.17	10.5	0.49
period	Paddle trigger	1047	“ ”	0.755 ± 0.086	17.6	0.091
Beam	$< 1.55 \times 10^9$ ppp	1138	“ ”	0.785 ± 0.089	20.0	0.046
intensity	$> 1.55 \times 10^9$ ppp	107	“ ”	0.46 ± 0.23	13.2	0.28
	-10 mrad in x	1260	“ ”	0.800 ± 0.10	30.3	0.0014
Detector	+10 mrad in x	1260	“ ”	0.774 ± 0.098	26.2	0.0060
alignment	-10 mrad in y	1260	“ ”	0.803 ± 0.10	28.9	0.0024
	+10 mrad in y	1260	“ ”	0.778 ± 0.090	22.4	0.022
Plume	# of hits < 20	1245	“ ”	0.774 ± 0.091	23.0	0.018
contamination	# of hits < 22	1268	“ ”	0.762 ± 0.089	22.0	0.024

Table 7.2: Fit results for cross checks. p-values expressed as fractions.

on this fit. To remove noisier events, I only kept events that had fewer than 21 hits remaining after the clustering stage. To see the effect of this cut, I shifted it up and down by 1 hit. The results for f (in Table 7.2) only vary by 1% from the original fit.

7.5 Interpretation of Results

source	error [\pm]
statistical	0.085
detector orientation	0.031
plume contamination	0.0077
total error	0.091

Table 7.3: Summary of absolute statistical and systematic errors for $f = 0.771$.

The fit result is $f = 0.771 \pm 0.085$ (stat.) ± 0.032 (syst.), meaning the scattering (range out) population needs tuning up (down) by 23% to match the data. Adjusting the fraction of protons that range out or scatter implies a change to the nuclear interaction length, λ_i . The fraction of protons that range out for a different nuclear interaction length, λ'_i , is

$$f = \frac{e^{-\frac{x}{\lambda'_i}}}{e^{-\frac{x}{\lambda_i}}} \quad (7.5)$$

where x is the proton range (track length). Solving for λ'_i ,

$$\lambda'_i = \frac{\lambda_i}{1 - \frac{\lambda_i}{x} \ln f} \quad (7.6)$$

Figure 7.15 is a plot of λ'_i for the sample of protons that range out in simulation, with an average value of 69.3 cm. Using $\lambda_i = 86.6$ cm and assuming a 5% error on λ_i , a ± 15.4 cm error on the track length (this is the spread of the distribution for protons that range out), and a total error on f of 0.091, the nuclear interaction length that would lead to the correct increase in scattering is 69.3 ± 6.8 cm.

We can convert this interaction length into an inelastic cross section for ~ 1 GeV/ c protons interacting in the NOvA detector using

$$\sigma_{in} = \frac{1}{n_t \lambda_i}. \quad (7.7)$$

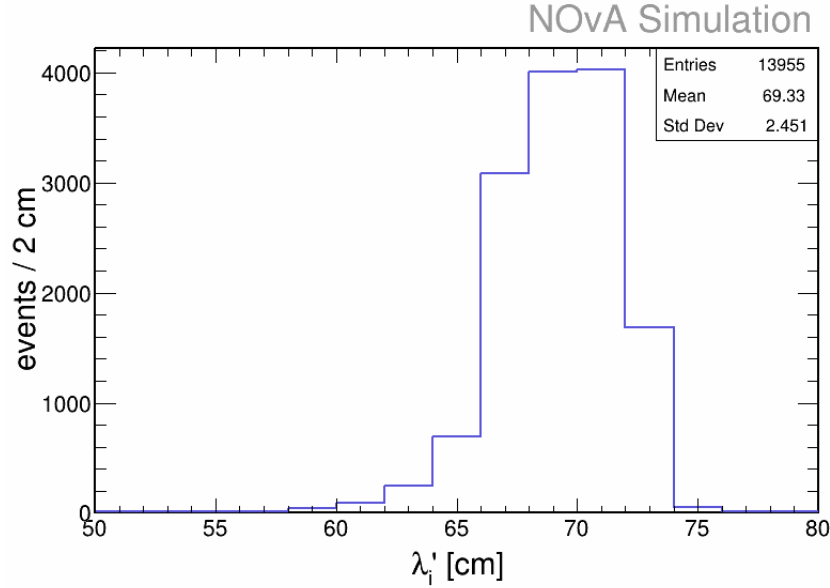


Figure 7.15: New nuclear interaction length, λ'_i , that would increase the number of protons that inelastically scatter to match the fit results. Plot made using simulated protons without any inelastic scattering.

To find the number density, n_t of the NOvA detector, I first summed the molar weight of each element in the detector, weighted by its mass fraction. For NOvA,

$$n_t = \frac{N_A}{M} \rho = \frac{6.022 \times 10^{23}}{16.04 \text{ g}} 0.971 \frac{\text{g}}{\text{cm}^3} = 3.65 \times 10^{22} \text{ cm}^{-3}. \quad (7.8)$$

Assuming a 5% error on n_t and the 10% (6.8 cm) error on the adjusted λ'_i , this yields an inelastic cross section for 1 GeV/ c protons in the NOvA detector of 395 ± 44 mb. The 11% error on this measurement is comparable to previous inelastic cross section measurements of 1 GeV/ c protons on carbon and oxygen [77]. Doing the same calculation for the original interaction length calculated using PDG values for each element and assuming a 5% error on that interaction length, yields a cross section of 316 ± 22 mb, which is 1.6σ lower than my result. Given how well we know the composition of the PVC, scintillator, and glue in the detector [51, 53], it is unlikely that we have the composition of our detectors incorrect to a degree that would cause a significantly smaller inelastic scattering cross section in simulation than in data. It is possible that the cross sections being used by GEANT are too small.

With the additional data taken in Period 3 (January-June 2021), we have at least double the

number of $1 \text{ GeV}/c$ protons, with the potential for more from a future run period. Running this same analysis on additional data would provide a more precise measurement of the cross section. It would also be interesting to increase the inelastic scattering cross section in GEANT, and see if simulation created with this change better matches the data.

Chapter 8

Summary

NOvA will continue to collect data until Fermilab begins the long beam shutdown in 2027 to prepare for PIP-II/DUNE. As NOvA's statistical errors continue to shrink, it will be more important to understand our leading sources of systematic uncertainty such as detector calibration and detector response. We aim to use data collected by the NOvA Test Beam program to learn more about our detector response and refine our calibration process.

I studied protons in the Test Beam Detector with momenta around 1 GeV/c, the high end of the momentum range relevant to quasielastic neutrino interactions in NOvA. One question this sample can help to answer is if we correctly simulate the fraction of protons that have an inelastic scattering interaction versus ranging out. If protons inelastically scatter at different rates in our simulation and data, the correction applied to the hadronic system when reconstructing neutrino energy could be inaccurate, since events with inelastic scattering will have less visible energy in the detector. This is particularly important for quasielastic ν_μ events, which have the lowest hadronic energy resolution, and therefore give us our best measurements of Δm_{32}^2 and θ_{23} .

The analysis discussed in this thesis was the first analysis done with NOvA Test Beam data. It suffered from low statistics and the challenges of running a neutrino detector in a high rate environment, but shows hints of a mismodelling of how protons interact in our detector. Since the end of the data used in this analysis, additional shielding was installed which further reduced the beam plume, resulting in less noisy events and the ability to collect events at a higher rate by increasing the beam intensity. Test Beam will stop collecting data in July 2022. There is work ongoing to expand on this proton analysis with the additional ~ 5000 good quality protons collected. Other planned analyses include studying the electromagnetic response of the detector with our electron sample and further hadronic response studies with our pion sample. As these analyses mature, work will begin to feed the information from them into our understanding of our systematic uncertainties for the NOvA analyses using our Near and Far Detectors.

References

1. Ellis, C. D. & Wooster, W. A. The average energy of disintegration of radium E. *Proceedings of the Royal Society of London. Series A, Containing Papers of a Mathematical and Physical Character* **117**, 109–123 (Dec. 1927) (cit. on p. 1).
2. Pauli, W. *Open letter to the group of radioactive people at the Gauverein meeting in Tübingen* Typed copy. Tr. by Kurt Tiesselmann. 1930 (cit. on p. 1).
3. Fermi, E. Versuch einer Theorie der β -Strahlen. I. *Zeitschrift für Physik* **88**, 161–177 (Mar. 1934) (cit. on p. 1).
4. Reines, F. The neutrino: From poltergeist to particle. *Rev. Mod. Phys.* **68**, 317–327 (1996) (cit. on pp. 1, 2).
5. Reines, F. & Cowan, C. L. Detection of the free neutrino. *Physical Review* **92**, 830–831 (1953) (cit. on p. 1).
6. Cowan, C. L., Reines, F., Harrison, F. B., Kruse, H. W. & McGuire, A. D. Detection of the free neutrino: A confirmation. *Science* **124**, 103–104 (1956) (cit. on p. 1).
7. Lee, T. D. & Yang, C. N. Question of Parity Conservation in Weak Interactions. *Phys. Rev.* **104**, 254–258 (1 Oct. 1956) (cit. on p. 2).
8. Wu, C. S., Ambler, E., Hayward, R. W., Hoppes, D. D. & Hudson, R. P. Experimental test of parity conservation in beta decay. *Physical Review* **105**, 1413–1415 (1957) (cit. on p. 3).
9. Wu, C.-S. The discovery of the parity violation in weak interactions and its recent developments. *Nishina Memorial Lectures*, 43–70 (1983) (cit. on p. 3).
10. Rose, M. E. On the Production of Nuclear Polarization. *Phys. Rev.* **75**, 213–213 (1 Jan. 1949) (cit. on p. 3).
11. Gorter, C. A new suggestion for aligning certain atomic nuclei. *Physica* **14**, 504 (1948) (cit. on p. 3).
12. Goldhaber, M., Grodzins, L. & Sunyar, A. W. Helicity of Neutrinos. *Phys. Rev.* **109**, 1015–1017 (1958) (cit. on p. 3).
13. Danby, G. *et al.* Observation of high-energy neutrino reactions and the existence of two kinds of neutrinos. *Physical Review Letters* **9**, 36–44 (1962) (cit. on pp. 3, 4).
14. Lee, T. D. & Yang, C. N. Theoretical Discussions on Possible High-Energy Neutrino Experiments. *Phys. Rev. Lett.* **4**, 307–311 (6 Mar. 1960) (cit. on p. 3).

15. Kodama, K. *et al.* Observation of tau neutrino interactions. *Physics Letters B* **504**, 218–224 (Apr. 2001) (cit. on pp. 4, 5).
16. Perl, M. L. *et al.* Evidence for Anomalous Lepton Production in $e^+ - e^-$ Annihilation. *Phys. Rev. Lett.* **35**, 1489–1492 (22 Dec. 1975) (cit. on p. 4).
17. Blondel, A. The number of neutrinos and the Z line shape. *Comptes Rendus Physique* **3**, 1155–1164 (2002) (cit. on p. 6).
18. Cleveland, B. T. *et al.* Measurement of the Solar Electron Neutrino Flux with the Homestake Chlorine Detector. *The Astrophysical Journal* **496**, 505–526 (Mar. 1998) (cit. on p. 6).
19. Hirata, K. S. *et al.* Observation of B-8 Solar Neutrinos in the Kamiokande-II Detector. *Phys. Rev. Lett.* **63**, 16 (1989) (cit. on p. 7).
20. Abdurashitov, J. N. *et al.* Measurement of the solar neutrino capture rate with gallium metal. *Phys. Rev. C* **60**, 055801 (5 Oct. 1999) (cit. on p. 7).
21. Hampel, W. *et al.* GALLEX solar neutrino observations: results for GALLEX IV. *Physics Letters B* **447**, 127–133 (1999) (cit. on p. 8).
22. Altmann, M. *et al.* GNO solar neutrino observations: results for GNO I. *Physics Letters B* **490**, 16–26 (2000) (cit. on p. 8).
23. Gribov, V. N. & Pontecorvo, B. Neutrino astronomy and lepton charge. *Phys. Lett. B* **28**, 493 (1969) (cit. on p. 8).
24. Maki, Z., Nakagawa, M. & Sakata, S. Remarks on the unified model of elementary particles. *Prog. Theor. Phys.* **28**, 870–880 (1962) (cit. on p. 8).
25. Fukuda, Y. *et al.* Evidence for Oscillation of Atmospheric Neutrinos. *Phys. Rev. Lett.* **81**, 1562–1567 (8 Aug. 1998) (cit. on p. 10).
26. Suzuki, Y. Solar neutrino results from Super-Kamiokande. *Nuclear Physics B - Proceedings Supplements* **77**, 35–42 (1999) (cit. on p. 10).
27. Abe, K. *et al.* Atmospheric neutrino oscillation analysis with external constraints in Super-Kamiokande I-IV. *Phys. Rev. D* **97**, 072001 (7 Apr. 2018) (cit. on pp. 11, 16, 31).
28. Ahmad, Q. R. *et al.* Measurement of the Rate of $\nu_e + d \rightarrow p + p + e^-$ Interactions Produced by ^8B Solar Neutrinos at the Sudbury Neutrino Observatory. *Phys. Rev. Lett.* **87**, 071301 (7 July 2001) (cit. on p. 11).
29. Alimonti, G. *et al.* The Borexino detector at the Laboratori Nazionali del Gran Sasso. *Nuclear Instruments and Methods in Physics Research Section A: Accelerators, Spectrometers, Detectors and Associated Equipment* **600**, 568–593 (2009) (cit. on p. 11).

30. Bellini, G. *et al.* Precision Measurement of the ${}^7\text{Be}$ Solar Neutrino Interaction Rate in Borexino. *Phys. Rev. Lett.* **107**, 141302 (14 Sept. 2011) (cit. on p. 11).
31. Bellini, G. *et al.* Measurement of the solar ${}^8\text{B}$ neutrino rate with a liquid scintillator target and 3 MeV energy threshold in the Borexino detector. *Phys. Rev. D* **82**, 033006 (3 Aug. 2010) (cit. on p. 11).
32. Neutrinos from the primary proton–proton fusion process in the Sun. *Nature* **512**, 383–386 (Aug. 2014) (cit. on p. 11).
33. Experimental evidence of neutrinos produced in the CNO fusion cycle in the Sun. *Nature* **587**, 577–582 (Nov. 2020) (cit. on p. 11).
34. Aartsen, M. G. *et al.* Determining neutrino oscillation parameters from atmospheric muon neutrino disappearance with three years of IceCube DeepCore data. *Phys. Rev. D* **91**, 072004 (7 Apr. 2015) (cit. on p. 11).
35. Gando, A. *et al.* Reactor on-off antineutrino measurement with KamLAND. *Phys. Rev. D* **88**, 033001 (3 Aug. 2013) (cit. on p. 12).
36. Double Chooz θ_{13} measurement via total neutron capture detection. *Nature Physics* **16**, 558–564 (Apr. 2020) (cit. on p. 12).
37. Adey, D. *et al.* Measurement of the Electron Antineutrino Oscillation with 1958 Days of Operation at Daya Bay. *Phys. Rev. Lett.* **121**, 241805 (24 Dec. 2018) (cit. on pp. 12, 13).
38. Shin, C. D. *et al.* Observation of reactor antineutrino disappearance using delayed neutron capture on hydrogen at RENO. *Journal of High Energy Physics* **2020** (Apr. 2020) (cit. on p. 12).
39. Litchfield, R. P. (*Direct*) *Measurement of theta-13* 2012 (cit. on p. 13).
40. An, F. P. *et al.* Observation of Electron-Antineutrino Disappearance at Daya Bay. *Phys. Rev. Lett.* **108**, 171803 (17 Apr. 2012) (cit. on p. 12).
41. Ahn, M. H. *et al.* Measurement of neutrino oscillation by the K2K experiment. *Phys. Rev. D* **74**, 072003 (7 Oct. 2006) (cit. on pp. 13, 14).
42. Adamson, P. *et al.* Measurement of Neutrino and Antineutrino Oscillations Using Beam and Atmospheric Data in MINOS. *Phys. Rev. Lett.* **110**, 251801 (25 June 2013) (cit. on p. 14).
43. Adamson, P. *et al.* Electron Neutrino and Antineutrino Appearance in the Full MINOS Data Sample. *Phys. Rev. Lett.* **110**, 171801 (17 Apr. 2013) (cit. on p. 14).
44. Acero, M. A. *et al.* An Improved Measurement of Neutrino Oscillation Parameters by the NOvA Experiment. arXiv: 2108.08219 [hep-ex] (Aug. 2021) (cit. on pp. 15, 16).
45. And K. Abe *et al.* Constraint on the matter–antimatter symmetry-violating phase in neutrino oscillations. *Nature* **580**, 339–344 (Apr. 2020) (cit. on pp. 15, 16, 31).

46. Adamson, P. *et al.* Precision Constraints for Three-Flavor Neutrino Oscillations from the Full MINOS+ and MINOS Dataset. *Phys. Rev. Lett.* **125**, 131802 (13 Sept. 2020) (cit. on pp. 16, 31).
47. Aartsen, M. G. *et al.* Measurement of Atmospheric Neutrino Oscillations at 6–56 GeV with IceCube DeepCore. *Phys. Rev. Lett.* **120**, 071801 (7 Feb. 2018) (cit. on pp. 16, 31).
48. Esteban, I., Gonzalez-Garcia, M., Maltoni, M., Schwetz, T. & Zhou, A. The fate of hints: updated global analysis of three-flavor neutrino oscillations. *Journal of High Energy Physics* **2020** (Sept. 2020) (cit. on p. 16).
49. Nunokawa, H., Parke, S. J. & Valle, J. W. F. CP Violation and Neutrino Oscillations. *Prog. Part. Nucl. Phys.* **60**, 338–402. arXiv: 0710.0554 [hep-ph] (2008) (cit. on p. 19).
50. Adamson, P. *et al.* The NuMI neutrino beam. *Nuclear Instruments and Methods in Physics Research Section A: Accelerators, Spectrometers, Detectors and Associated Equipment* **806**, 279–306 (2016) (cit. on pp. 19, 20).
51. Talaga, R. *et al.* PVC extrusion development and production for the NOvA neutrino experiment. *Nuclear Instruments and Methods in Physics Research Section A: Accelerators, Spectrometers, Detectors and Associated Equipment* **861**, 77–89 (2017) (cit. on pp. 23, 107).
52. Ayres, D. S. *et al.* The NOvA Technical Design Report (Oct. 2007) (cit. on p. 23).
53. Mufson, S. *et al.* Liquid scintillator production for the NOvA experiment. *Nuclear Instruments and Methods in Physics Research Section A: Accelerators, Spectrometers, Detectors and Associated Equipment* **799**, 1–9 (2015) (cit. on pp. 23, 107).
54. *SNEWS: SuperNova Early Warning System* <https://snews.bnl.gov/> (cit. on p. 25).
55. Center, N. G. S. F. *GCN: The Gamma-ray Coordinates Network (TAN: Transient Astronomy Network)* <https://gcn.gsfc.nasa.gov/> (cit. on p. 25).
56. Ferrari, A., Sala, P. R., Fasso, A. & Ranft, J. FLUKA: A multi-particle transport code (Program version 2005) (Oct. 2005) (cit. on p. 28).
57. Böhlen, T. *et al.* The FLUKA Code: Developments and Challenges for High Energy and Medical Applications. *Nuclear Data Sheets* **120**, 211–214 (2014) (cit. on p. 28).
58. Agostinelli, S. *et al.* Geant4—a simulation toolkit. *Nuclear Instruments and Methods in Physics Research Section A: Accelerators, Spectrometers, Detectors and Associated Equipment* **506**, 250–303 (2003) (cit. on pp. 28, 86, 95, 96).
59. Aliaga Soplin, L. *Neutrino Flux Prediction for the NuMI Beamline* PhD thesis (William-Mary Coll., 2016) (cit. on p. 28).
60. Andreopoulos, C. *et al.* The GENIE Neutrino Monte Carlo Generator. *Nucl. Instrum. Meth.* **A614**, 87–104. arXiv: 0905.2517 [hep-ph] (2010) (cit. on p. 28).

61. Haggmann, C., Lange, D. & Wright, D. *Cosmic-ray shower generator (CRY) for Monte Carlo transport codes in 2007 IEEE Nuclear Science Symposium Conference Record 2* (2007), 1143–1146 (cit. on pp. 28, 84).
62. Accelerator Division – Operations Department, Barak, D., Harrison, B. & Watts, A. *Concepts Rookie Book 2020* (cit. on p. 35).
63. Watts, A. *MCenter Secondary Beamline for NOvA Test Beam* (cit. on p. 36).
64. Messier, M. *Modeling the test-beam analysis magnet field* NOvA internal presentation docdb-46939. 2020 (cit. on p. 40).
65. Hahsler, M., Piekenbrock, M. & Doran, D. dbSCAN: Fast Density-Based Clustering with R. *Journal of Statistical Software* **91**, 1–30 (2019) (cit. on p. 41).
66. Niner, E. D. *Observation of Electron Neutrino Appearance in the NuMI Beam with the NOvA Experiment* p. 67-80. PhD thesis (Indiana U., 2015) (cit. on p. 51).
67. Pershey, D., Huang, J. & Judah, M. *TDSlicer Technote* NOvA internal technical note docdb-27689. 2019 (cit. on p. 79).
68. Baird, M. & Messier, M. *Track Fitting and Muon Identification with BreakPointFitter* NOvA internal technical note docdb-32455. 2018 (cit. on pp. 79, 85).
69. Rebel, B. *Window Tracking Algorithm for Cosmic Ray Muons* NOvA internal technical note docdb-15977. 2016 (cit. on p. 85).
70. Futch, A. M. & Messier, M. D. *Cross-check of muon energy calibration* NOvA internal technical note docdb-25083. 2017 (cit. on p. 85).
71. Niner, E. *Vertex Clustering with Possibilistic Fuzzy-K Means Algorithm* NOvA internal technical note docdb-7648. 2012 (cit. on p. 85).
72. Haino, S. *et al.* Measurements of primary and atmospheric cosmic-ray spectra with the BESS-TeV spectrometer. *Physics Letters B* **594**, 35–46 (2004) (cit. on p. 86).
73. Birks, J. B. Scintillations from Organic Crystals: Specific Fluorescence and Relative Response to Different Radiations. *Proceedings of the Physical Society. Section A* **64**, 874–877 (Oct. 1951) (cit. on p. 89).
74. Yu, S. *Measurement of Electron Neutrino and Antineutrino Appearance with the NOvA Experiment* p. 14-28. PhD thesis (IIT, Chicago, 2020) (cit. on p. 89).
75. Group, P. D. *et al.* Review of Particle Physics. *Progress of Theoretical and Experimental Physics* **2020**. 083C01. eprint: <https://academic.oup.com/ptep/article-pdf/2020/8/083C01/34673722/ptaa104.pdf> (Aug. 2020) (cit. on p. 94).

76. Glauber, R. J. in *Lectures in Theoretical Physics* (eds Britten, W. E. *et al.*) 315–414 (Inter-Science, New York, 1959) (cit. on p. 94).
77. Barashenkov, V. S., Gudima, K. K. & Toneev, V. D. Cross Sections for Fast Particles and Atomic Nuclei. *Fortschritte der Physik* **17**, 683–725 (1969) (cit. on pp. 94, 95, 107).
78. Barashenkov, V. S., Ilinov, A. S., Sobolevskii, N. M. & Toneev, V. D. Interaction of particles and nuclei of high and ultrahigh energy with nuclei. *Soviet Physics Uspekhi* **16**, 31–52 (Jan. 1973) (cit. on p. 95).

Vita

EDUCATION

Indiana University, *Bloomington, IN*

PhD Physics July 2022

MS Physics November 2016

International Neutrino Summer School (INSS), *Fermilab* August 2019

Excellence in Detector and Instrumentation Technologies (EDIT), *Fermilab* March 2018

United States Particle Accelerator School (USPAS), *Northern Illinois University*

Accelerator Physics course June 2017

The University of Iowa, *Iowa City, IA*

BS Physics May 2014

RESEARCH EXPERIENCE

NuMI Off-axis ν_e Appearance experiment (NOvA) June 2015 - May 2022

Advisor: Mark Messier, PhD Indiana University

- Created infrastructure to track shutoffs of detector components within selected events in NOvA Test Beam.
- Developed keepup analysis to track particle yield in the NOvA Test Beam detector on a week-to-week basis.
- Served as a deputy run coordinator to assist with NOvA Test Beam operations.
- Assembled data acquisition (DAQ) and monitoring systems for NOvA Test Beam based on pre-existing DAQ for NOvA Near and Far Detectors.
- Developed and maintained detector monitoring systems to maximize detector uptime and quality data.
- Analyzed data from pedestal scans of the NOvA Far Detector to determine more accurate parameters for our simulated pulse shaping of physics hits in the detector.
- Helping to maintain documentation including instructions for shifters and descriptions of plots used for monitoring NOvA detectors.

- Improved software for setting hardware thresholds on channels in the NOvA detectors.
- Investigated excess vertex energy by reconstructing the Δ mass from $\Delta \rightarrow N\pi^0$ decays.

Theoretical neutrino research

August 2013 - May 2014

Advisor: Mary Hall Reno, PhD University of Iowa

- Independent study on neutrino oscillations in vacuum and matter.
- Studied basics of neutrino Monte Carlo simulations.

Main Injector Experiment for ν -A (MINERvA) - REU student

May 2013 - August 2013

Advisor: Kevin McFarland, PhD University of Rochester

- Analyzed charged-current quasielastic events in the MINERvA detector to discover a way to discriminate multi-nucleon from single nucleon final states.

uMI Off-axis ν_e Appearance experiment (NOvA) - REU student

May 2012 - August 2012

Advisor: Mark Messier, PhD Indiana University

- Applied pre-selection cuts to NOvA prototype data to eliminate cosmic ray events.
- Hand-scanned the selected sample to identify electron neutrino events for testing reconstruction software.

PUBLICATIONS

Acero, M. A. *et al.* Search for Active-Sterile Antineutrino Mixing Using Neutral-Current Interactions with the NOvA Experiment. *Phys. Rev. Lett.* **127**, 201801. <https://link.aps.org/doi/10.1103/PhysRevLett.127.201801> (20 Nov. 2021)

Acero, M. A. *et al.* Extended search for supernovalike neutrinos in NOvA coincident with LIGO/Virgo detections. *Phys. Rev. D* **104**, 063024. <https://link.aps.org/doi/10.1103/PhysRevD.104.063024> (6 Sept. 2021)

Acero, M. A. *et al.* Seasonal variation of multiple-muon cosmic ray air showers observed in the NOvA detector on the surface. *Phys. Rev. D* **104**, 012014. <https://link.aps.org/doi/10.1103/PhysRevD.104.012014> (1 July 2021)

Acero, M. A. *et al.* Search for slow magnetic monopoles with the NOvA detector on the surface. *Phys. Rev. D* **103**, 012007. <https://link.aps.org/doi/10.1103/PhysRevD.103.012007> (1 Jan. 2021)

Acero, M. A. *et al.* Supernova neutrino detection in NOvA. *Journal of Cosmology and Astroparticle Physics* **2020**, 014–014. <https://doi.org/10.1088/1475-7516/2020/10/014> (Oct. 2020)

Acero, M. A. *et al.* Measurement of neutrino-induced neutral-current coherent π^0 production in the NOvA near detector. *Phys. Rev. D* **102**, 012004. <https://link.aps.org/doi/10.1103/PhysRevD.102.012004> (1 July 2020)

Acero, M. A. *et al.* Search for multimessenger signals in NOvA coincident with LIGO/Virgo detections. *Phys. Rev. D* **101**, 112006. <https://link.aps.org/doi/10.1103/PhysRevD.101.112006> (11 June 2020)

Acero, M. A. *et al.* First measurement of neutrino oscillation parameters using neutrinos and antineutrinos by NOvA. *Phys. Rev. Lett.* **123**, 151803. <https://link.aps.org/doi/10.1103/PhysRevLett.123.151803> (15 Oct. 2019)

Acero, M. A. *et al.* Observation of seasonal variation of atmospheric multiple-muon events in the NOvA Near Detector. *Phys. Rev. D* **99**, 122004. <https://link.aps.org/doi/10.1103/PhysRevD.99.122004> (12 June 2019)

Acero, M. A. *et al.* New constraints on oscillation parameters from ν_e appearance and ν_μ disappearance in the NOvA experiment. *Phys. Rev. D* **98**, 032012. <https://link.aps.org/doi/10.1103/PhysRevD.98.032012> (3 Aug. 2018)

Adamson, P. *et al.* Search for active-sterile neutrino mixing using neutral-current interactions in NOvA. *Phys. Rev. D* **96**, 072006. <https://link.aps.org/doi/10.1103/PhysRevD.96.072006> (7 Oct. 2017)

TALKS AND POSTERS

The NOvA Test Beam Program *Poster*

APS Division of Particles & Fields, *Boston, MA*

August 2019

The NOvA Test Beam Program

New Perspectives, *Fermilab - Batavia, IL*

June 2019

Data Monitoring and Performance of the NOvA Detectors

New Perspectives, *Fermilab - Batavia, IL*

June 2017

Hand Scan Results for NuMI Events Recorded in the NOvA Near Detector *Poster*

APS Conference for Undergraduate Women in Physics, *Urbana-Champaign, IL* January 2013

APS Division of Nuclear Physics - CEU Program, *Newport Beach, CA* October 2012

ACTIVITIES

Young NOvA

- Institutional Board representative June 2020 - June 2021
- Member August 2015 - present

Society of Physics Students - Iowa Chapter

- Vice President June 2012 - May 2014
- Secretary August 2011 - May 2012
- Member August 2010 - May 2014

SCHOLARSHIPS AND AWARDS

Fermilab Neutrino Physics Center (NPC) Fellowship Award Fall 2019

Recognizes the exemplary service of an individual who has made significant contributions to the experiment in the way of service to the community.

Van Allen Award Fall 2013

To a senior for outstanding work in physics or astronomy.

Departmental Distinguished Service Award May 2012

For volunteer efforts as Secretary of local chapter of Society of Physics Students.

Myrtle K. Maier Scholarship May 2012, renewed May 2013

Physics department award based primarily on scholastic ability.